

AD-A066 095

PROTOTYPE DEVELOPMENT ASSOCIATES INC SANTA ANA CALIF

F/G 20/4

HARDENED RV DEVELOPMENT PROGRAM. PHASE IV. VEHICLE RECOVERY TEC--ETC(U)

AUG 78 D H SMITH, L S GROENER

DNA001-76-C-0310

UNCLASSIFIED

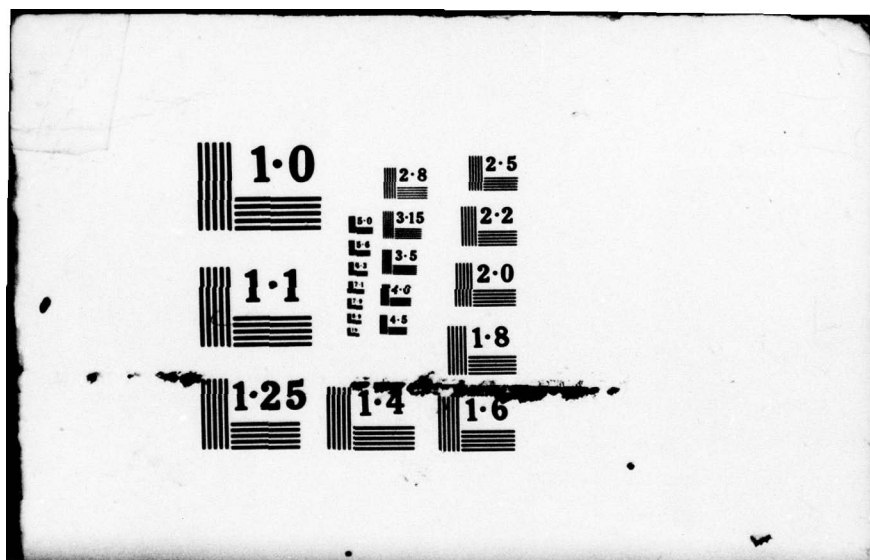
PDA-TR-1065-00-19

DNA-4656F

NL

1 OF 1
ADA
066095





AD A0 66095

DDC FILE COPY

(12) ^{NW} LEVEL III

AD-E 300 470

DNA 4656F

HARDENED RV DEVELOPMENT PROGRAM—PHASE IV

Vehicle Recovery Technology Wind Tunnel Tests

Prototype Development Associates, Inc.
1740 Garry Avenue
Santa Ana, California 92705

August 1978

Final Report for Period 11 May 1976—31 March 1977

CONTRACT No. DNA 001-76-C-0310

APPROVED FOR PUBLIC RELEASE;
DISTRIBUTION UNLIMITED.

THIS WORK SPONSORED BY THE DEFENSE NUCLEAR AGENCY
UNDER RDT&E RMSS CODE X337076469 Q93QAXAD41035 H2590D.

Prepared for
Director
DEFENSE NUCLEAR AGENCY
Washington, D. C. 20305

DDC
RECEIVED
MAR 21 1979
B

79 02 26 086

Destroy this report when it is no longer
needed. Do not return to sender.

PLEASE NOTIFY THE DEFENSE NUCLEAR AGENCY,
ATTN: TISI, WASHINGTON, D.C. 20305, IF
YOUR ADDRESS IS INCORRECT, IF YOU WISH TO
BE DELETED FROM THE DISTRIBUTION LIST, OR
IF THE ADDRESSEE IS NO LONGER EMPLOYED BY
YOUR ORGANIZATION.



UNCLASSIFIED

SECURITY CLASSIFICATION OF THIS PAGE (When Data Entered)

REPORT DOCUMENTATION PAGE		READ INSTRUCTIONS BEFORE COMPLETING FORM
1. REPORT NUMBER DNA 4656F	2. GOVT ACCESSION NO.	3. RECIPIENT'S CATALOG NUMBER
4. TITLE (and Subtitle) HARDENED RV DEVELOPMENT PROGRAM, PHASE IV. Vehicle Recovery Technology Wind Tunnel Tests.	5. TYPE OF REPORT & PERIOD COVERED Final Report, Interim 11 May 1976—31 Mar 1977	6. PERFORMING ORG. REPORT NUMBER PDA-TR-1065-00-19
7. AUTHOR(s) D. H. Smith L. S. Groener	8. CONTRACT OR GRANT NUMBER(s) DNA 001-76-C-0310	9. PERFORMING ORGANIZATION NAME AND ADDRESS Prototype Development Associates, Inc. 1740 Garry Avenue Santa Ana, California 92705
10. CONTROLLING OFFICE NAME AND ADDRESS Director Defense Nuclear Agency Washington, D.C. 20305	11. REPORT DATE Aug 1978	12. PROGRAM ELEMENT, PROJECT, TASK AREA & WORK UNIT NUMBERS NWED Subtask Q93QAXAD410-35
13. MONITORING AGENCY NAME & ADDRESS (if different from Controlling Office) DNA, SBIE	14. SECURITY CLASS (of this report) UNCLASSIFIED	15. DECLASSIFICATION/DOWNGRADING SCHEDULE
16. DISTRIBUTION STATEMENT (of this Report) Approved for public release; distribution unlimited. 6270VH		
17. DISTRIBUTION STATEMENT (of the abstract entered in Block 20, if different from Report)		
18. SUPPLEMENTARY NOTES This work sponsored by the Defense Nuclear Agency under RDT&E RMSS Code X337076469 Q93QAXAD41035 H2590D.		
19. KEY WORDS (Continue on reverse side if necessary and identify by block number) Wake-Drogue Mass-Jettison-Drogue Reentry Nosetip Nosetip Recovery Wind Tunnel Testing 2,000,000/ft to 4,000,000/ft.		
20. ABSTRACT (Continue on reverse side if necessary and identify by block number) A study of mass-jettison-drogue ICBM nosetip recovery vehicles was conducted, followed by wind tunnel tests of the configurations that appeared most attractive. Various combinations of vehicle and nosetip geometry were tested in AEDC tunnel A at Mach numbers from 3 to 5 and Reynolds numbers $2 \times 10^6/\text{ft}$ to $4 \times 10^6/\text{ft}$. Heat transfer data was taken to assure that turbulent flow over the entire model was achieved; however, the primary goal of the tests was force data.		

DD FORM 1 JAN 73 1473 EDITION OF 1 NOV 65 IS OBSOLETE

UNCLASSIFIED

SECURITY CLASSIFICATION OF THIS PAGE (When Data Entered)

390 71 4

79 02 26 086

JUB

PREFACE

This report summarizes the results of an analytical and experimental study which objectives were to evaluate alternate configurations for mass-jettison-drogue ICBM nosetip recovery vehicles, and to perform wind tunnel tests on those configurations found most attractive. This work was performed by Prototype Development Associates, Inc., 1740 Garry Avenue, Santa Ana, California under the management of Major W. E. Mercer of the Defense Nuclear Agency, with technical assistance provided by Captain J. Pellegrini of the Air Force Space and Missile Systems Organization.

ACCESSION for	
NTIS	White Section <input checked="" type="checkbox"/>
DDC	Bufi Section <input type="checkbox"/>
UNANNOUNCED	<input type="checkbox"/>
JUSTIFICATION _____	
BY _____	
DISTRIBUTION/AVAILABILITY CODES	
Dist.	AVAIL. and/or SPECIAL
A	

Conversion factors for U. S. customary to metric (SI) units of measurement.

To Convert From	To	Multiply By
angstrom	meters (m)	1.000 000 X E -10
atmosphere (normal)	kilo pascal (kPa)	1.013 25 X E +2
bar	kilo pascal (kPa)	1.000 000 X E +2
barn	meter ² (m ²)	1.000 000 X E -28
British thermal unit (thermochemical)	joule (J)	1.054 350 X E +3
calorie (thermochemical)	joule (J)	4.184 000
cal (thermochemical)/cm ²	mega joule/m ² (MJ/m ²)	4.184 000 X E -2
curie	giga becquerel (GBq)*	3.700 000 X E +1
degree (angle)	radian (rad)	1.745 329 X E -2
degree Fahrenheit	degree kelvin (K)	$T_K = (t^{\circ}F + 459.67)/1.8$
electron volt	joule (J)	1.602 19 X E -19
erg	joule (J)	1.000 000 X E -7
erg/second	watt (W)	1.000 000 X E -7
foot	meter (m)	3.048 000 X E -1
foot-pound-force	joule (J)	1.355 818
gallon (U. S. liquid)	meter ³ (m ³)	3.785 412 X E -3
inch	meter (m)	2.540 000 X E -2
jerk	joule (J)	1.000 000 X E +9
joule/kilogram (J/kg) (radiation dose absorbed)	Gray (Gy)**	1.000 000
kilotons	terajoules	4.183
kip (1000 lbf)	newton (N)	4.448 222 X E +3
kip/inch ² (ksi)	kilo pascal (kPa)	6.894 757 X E +3
ktap	newton-second/m ² (N-s/m ²)	1.000 000 X E +2
micron	meter (m)	1.000 000 X E -6
mil	meter (m)	2.540 000 X E -5
mile (international)	meter (m)	1.609 344 X E +3
ounce	kilogram (kg)	2.834 952 X E -2
pound-force (lbf avoirdupois)	newton (N)	4.448 222
pound-force inch	newton-meter (N·m)	1.129 848 X E -1
pound-force/inch	newton/meter (N/m)	1.751 268 X E +2
pound-force/foot ²	kilo pascal (kPa)	4.788 026 X E -2
pound-force/inch ² (psi)	kilo pascal (kPa)	6.894 757
pound-mass (lbm avoirdupois)	kilogram (kg)	4.535 924 X E -1
pound-mass-foot ² (moment of inertia)	kilogram-meter ² (kg·m ²)	4.214 011 X E -2
pound-mass/foot ³	kilogram/meter ³ (kg/m ³)	1.601 846 X E +1
rad (radiation dose absorbed)	Gray (Gy)**	1.000 000 X E -2
roentgen	coulomb/kilogram (C/kg)	2.579 760 X E -4
shake	second (s)	1.000 000 X E -8
slug	kilogram (kg)	1.459 390 X E +1
torr (mm Hg, 0° C)	kilo pascal (kPa)	1.333 22 X E -1

*The becquerel (Bq) is the SI unit of radioactivity; 1 Bq = 1 event/s.

**The Gray (Gy) is the SI unit of absorbed radiation.

A more complete listing of conversions may be found in "Metric Practice Guide E 380-74," American Society for Testing and Materials.

TABLE OF CONTENTS

<u>Section</u>		<u>Page</u>
1.0	INTRODUCTION AND SUMMARY	7
2.0	SIZING STUDY	15
2.1	Performance Requirements	15
2.2	Vehicle Design	15
2.3	Conclusions	27
3.0	WIND TUNNEL TESTS	35
3.1	Facility Selection	35
3.2	Apparatus	35
3.2.1	Wind Tunnel	35
3.2.2	Model	37
3.2.3	Instrumentation	37
3.3	Procedure	48
3.3.1	Test Conditions	48
3.3.2	Test Procedure	48
3.3.2.1	General	48
3.3.2.2	Data Acquisition	53
3.3.3	Data Reduction	53
3.3.4	Data Uncertainty	54
3.3.4.1	Test Conditions	54
3.3.4.2	Aerodynamic Coefficients	54
3.4	Results	55
3.4.1	Wind Tunnel Data	55
3.4.2	Comparison to Theory	66
4.0	CONCLUSIONS	78
5.0	REFERENCES	80

LIST OF FIGURES

<u>Figure</u>		<u>Page</u>
1-1	Mass-jettison-drogue (MJD) recovery concept.	8
1-2	FLAME drag data comparison.	9
1-3	FLAME flow fields.	11
1-4	Recovery vehicle configurations.	12
1-5	Model nosetips.	14
2-1	Stagnation point recession history comparison.	16
2-2	Effect of recovery ballistic coefficient charge on parachute requirements.	17
2-3	9.25-inch base wake-drogue.	20
2-4	9.25-inch base flared body.	21
2-5	10.0-inch base wake-drogue (sharp and blunt).	22
2-6	11.0-inch base flared body (sharp and blunt).	23
2-7	17.0-inch base wake-drogue.	24
2-8	17.0-inch base flared body.	25
2-9	Typical deceleration profile.	29
2-10	Typical velocity profile.	30
2-11	Drag area and volume comparison.	32
3-1	Wind tunnel and model injection system.	36
3-2	Model details.	38
3-3	Nosetips.	42
3-4	Boundary layer trips.	43
3-5	Gardon gage location.	46
3-6	FLAME flow fields.	57
3-7	FLAME configuration shadowgraphs.	58
3-8	FLAME drogue angle sensitivity.	59
3-9	FLAME nose shape sensitivity (Mach 5).	60
3-10	FLAME nose shape sensitivity (Mach 4).	61
3-11	FLAME nose shape sensitivity (Mach 3).	62
3-12	Pre-recovery nose shape sensitivity.	63
3-13	FLAME bluntness sensitivity (25° drogue).	64
3-14	Flared body drogue angle sensitivity.	65
3-15	Flared body nose shape sensitivity (30° flare, Mach 5, 0.135 bluntness).	67
3-16	Flared body nose shape sensitivity (25° flare, Mach 5, 0.135 bluntness).	68
3-17	Flared body nose shape sensitivity (25° flare, Mach 3, 0.135 bluntness).	69
3-18	Flared body nose shape sensitivity (25° flare, Mach 5, 0.190 bluntness).	70
3-19	Flared body nose shape sensitivity (25° flare, Mach 5, 0.250 bluntness).	71
3-20	Boom size sensitivity.	72
3-21	Flare position sensitivity.	73
3-22	Influence of bluntness on drag.	74
3-23	Influence of bluntness on center-of-pressure position.	75
3-24	Influence of drogue/flare angle on drag.	76
3-25	Influence of drogue/flare angle on center-of-pressure position.	77

LIST OF TABLES

<u>Table</u>		<u>Page</u>
2-1	Flight configuration study matrix.	19
2-2	Recovery vehicle electronics packaging study.	26
2-3	Typical weight and balance calculation summary.	28
2-4	Recovery performance predictions.	31
3-1	Hemispheric, biconic, flat, and asymmetric nosetip dimensions.	44
3-2	Pedorical nosetip dimensions.	45
3-3	Test summary data group numbers.	49
3-4	Model component designation.	52

1.0 INTRODUCTION AND SUMMARY

Reentry vehicle nosetip design is an area of continued interest in ballistic missile research and development. Many unresolved questions would be answered if the nosetips of high performance vehicles could be recovered economically. The initial steps in the development of such a capability were funded under two previous DNA contracts to Prototype Development Associates, Inc. (PDA): the HEART Recovery Vehicle (HRV) Program (Reference 1), and the Fighter Launched Advanced Materials Experiment (FLAME) Program (Reference 2). The first of these was a concept demonstration program with a sounding rocket launch vehicle. The second program used a fighter launched booster to simulate the terminal portion of reentry; however, even in this case, the environment was less severe than for a modern ICBM.

In both programs, a special purpose reentry vehicle based on the "mass-jettison-drogue" (MJD) concept was utilized. This concept is illustrated schematically in Figure 1-1. The vehicle includes a nosetip section, a drogue section, a connecting structural boom, and high density side panels. At the recovery initiation altitude (typically 10 to 15 Kft), pyrotechnic devices part the external heatshield and deploy the side panels. The resulting abrupt decrease in mass and increase in drag causes a large decrease in the vehicle ballistic coefficient. Thus, the vehicle decelerates rapidly to subsonic velocities permitting deployment of a parachute stowed in the drogue section. Typically, the drogue section also will contain various devices to aid the search team in locating the vehicle after touch-down, as well as a telemetry system to transmit in-flight data.

An underlying philosophy of the HRV and FLAME programs was to obtain an early flight evaluation of the MJD concept with a minimum of design studies and ground tests. This approach was reasonably successful with an actual recovery achieved under each program. Most of the problems encountered were of a routine nature to be expected with new hardware development.

Figure 1-2, however, illustrates a potential problem with the specific geometry selected for the recovery vehicles. Shown are drag coefficient data for two FLAME flights derived from radar trajectory data for the period after side panel deployment. Also presented are theoretical drag curves for 1) the drogue alone, and 2) the complete reentry vehicle before side panel deployment. The measured data for Flight F-002 roughly parallel the theoretical drogue curve and are free of abrupt discontinuities. These F-002 data suggest a stable flow pattern with a relatively small separated region at the drogue root (where it joins with the boom). The drag level is entirely satisfactory for the recovery system.

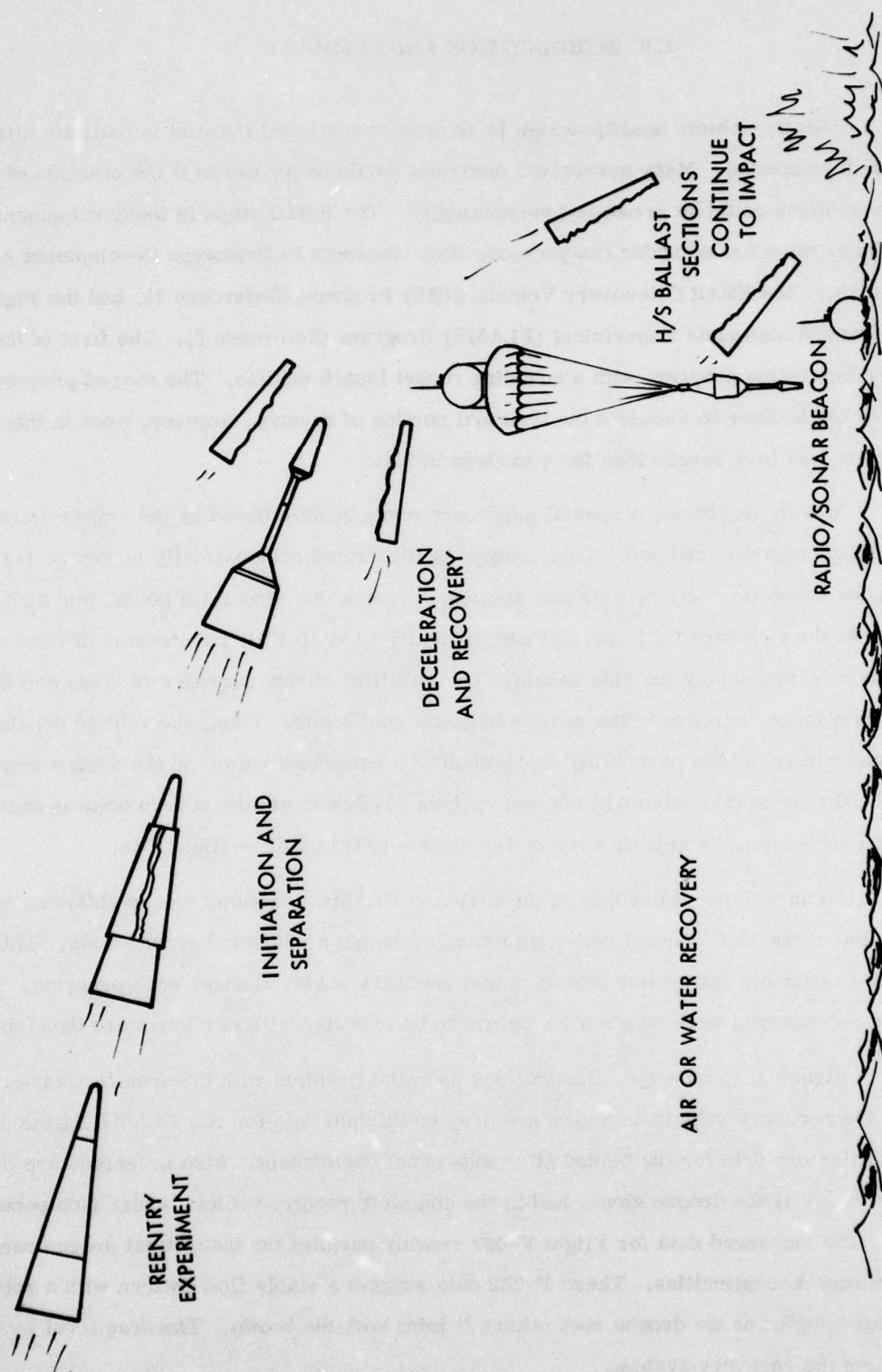


Figure 1-1. Mass-jettison-drogue (MJD) recovery concept.

FLIGHT DATA

○ F-007

□ F-002

BOUNDING ANALYSES

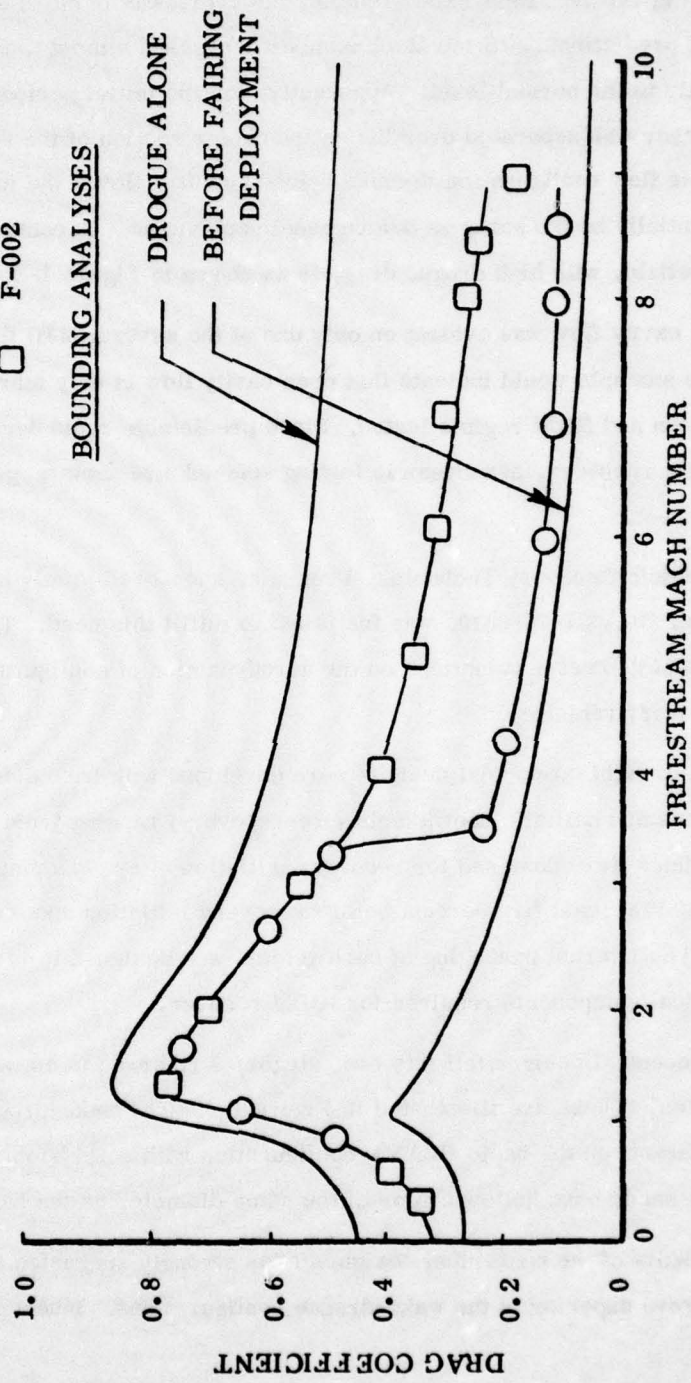


Figure 1-2. FLAME drag data comparison.

The drag for the Flight F-007 vehicle, however, was in close agreement with the pre-panel deployment predictions until the Mach number decreased almost to three. The drag then increased abruptly to the normal level. Apparently, for the initial period after panel deployment, the boundary layer was separated over the entire center section of the vehicle as shown in Figure 1-3a. With this flow configuration (termed "closed cavity" flow), the inviscid flowfield and pressures would essentially be the same as before panel deployment. In contrast, the "normal" (or "open cavity") flowfield, with high drogue drag, is as shown in Figure 1-3b.

Closed cavity flow was evident on only one of the several MJD flights to date. However, even this single example would indicate that open cavity flow is only marginally stable for the vehicle configuration and flight regime tested. Since predictable rapid deceleration is essential for reliable low altitude recovery, aerodynamic testing seemed a necessary prelude to further flight vehicle development.

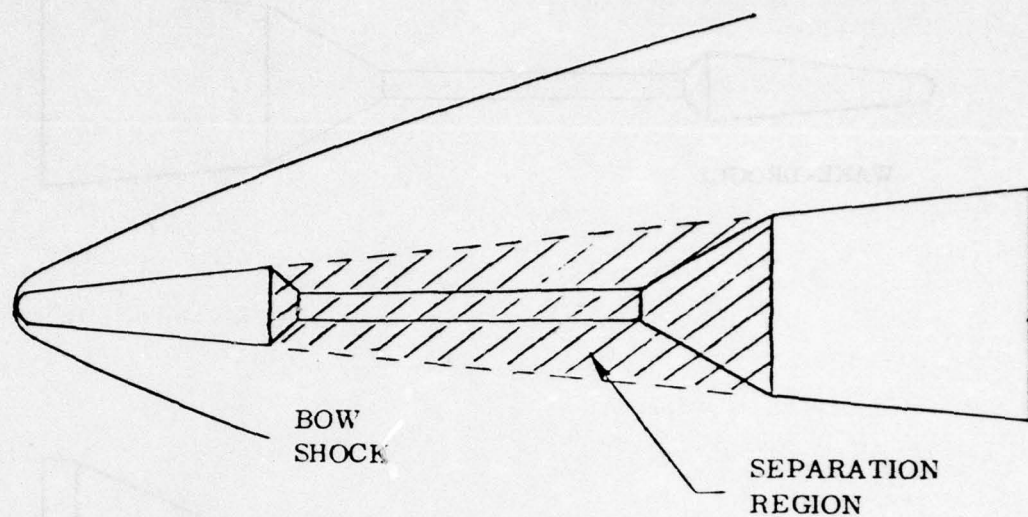
The Vehicle Recovery Technology Program, sponsored jointly by SAMSO and DNA under Contract Number DNA001-76-0310, was instituted to fulfill this need. The objective was to investigate the effects of geometry variations on the aerodynamics of configurations suitable for ICBM range MJD recovery vehicles.

A total of eight conceptual designs were developed with base diameters ranging from 9.25 inches to 17 inches and ballistic coefficients (pre-recovery) ranging from 1990 lb/ft^2 to 3600 lb/ft^2 . The vehicles were designed for recovery initiation after peak stagnation pressure, and to have static margins of at least five percent before recovery initiation and ten percent after recovery initiation. The internal packaging of each vehicle was designed to include a parachute system and all electrical components required for ICBM recovery.

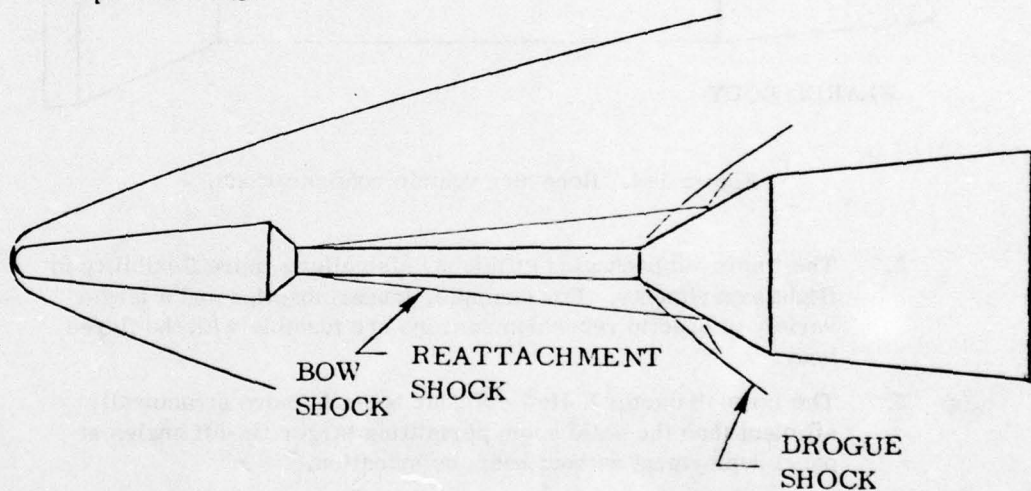
The conceptual designs fell into two categories referred to as wake-drogue vehicles and flared body vehicles. These are illustrated in Figure 1-4. The wake-drogue vehicles are simple geometry variations on the basic FLAME configuration with solid booms. The flared body vehicles, on the other hand, have hollow booms of the same diameter as the base of the nose section.

The results of the conceptual design studies strongly suggested that the flared body configuration would prove superior to the wake-drogue configurations. Inherent advantages of the flared body are:

1. The hollow boom allows more efficient vehicle packaging. The improved packaging permits a lower flare angle (with reduced vulnerability to separated flow) for a fixed static margin and a fixed ballistic coefficient ratio (ratio of ballistic coefficient before and after panel deployment).



a. Separated Flow



b. Attached Flow

Figure 1-3. FLAME flow fields.

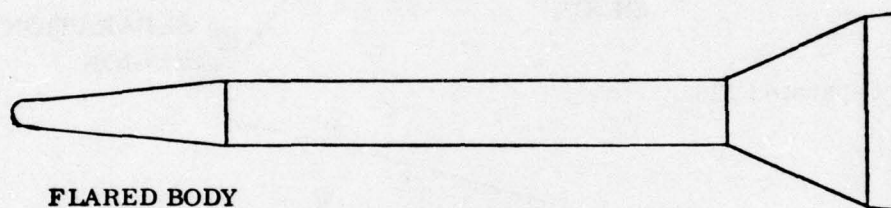
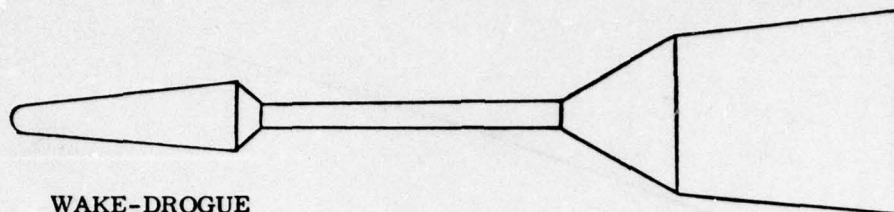


Figure 1-4. Recovery vehicle configurations.

2. The improved packaging efficiency also allows more flexibility in flight experiments. For example, longer nosetips and a larger variety of nosetip recession sensors are feasible with the flared body.
3. The large diameter hollow cylinder boom is more structurally efficient than the solid boom permitting larger tip-off angles at panel deployment without boom deformation.

Other important conclusions of the analytical studies were that, to meet the goal of recovering nose-tips with a final shape representative of a normal (no recovery attempt) flight, a recovery initiation altitude of about 15 Kft is adequate and the ratio of ballistic coefficients before and after recovery initiation should be at least ten.

The aerodynamic tests were conducted in the AEDC Tunnel A at Mach numbers of 3, 4, and 5, and at unit Reynolds numbers up to 4×10^6 /ft. Some initial heat transfer measurements were made early in the program to ensure a turbulent boundary layer in the regions of potential separation. The basic source of data, however, was force measurements from which drag coefficients could be derived.

The wind tunnel models were composed of modular sections that could be assembled in a variety of ways to obtain a large number of geometries. Included were three different boom diameters corresponding to a FLAME type wake-drogue, a flared body, and an intermediate diameter. Flare (drogue) angles were varied from 20° to 35° . Fifteen different nose sections were available (Figure 1-5) to evaluate the effect of possible ablated shapes on flow stability. Also tested were configurations corresponding to the basic vehicle (pre-panel deployment) with various bluntness ratios.

The force measurements were taken while the model angle-of-attack was varied continuously between -5 degrees to $+22$ degrees at a pitch rate of 0.5 deg/sec. In this way, it was possible to obtain a large amount of data in a minimum number of runs.

Tests with the original FLAME configuration confirmed the hypothesized explanation of the Flight F-007 anomaly. When the model was injected at zero angle-of-attack, a closed cavity flow field would result. However, when the model was pitched to one degree or more angle-of-attack, the flow field changed to the open cavity type with a corresponding large increase in drag. In some cases, the open cavity flow field would persist when the model was returned to zero angle-of-attack. Thus, the flow could be termed bi-stable at angles-of-attack or less than one degree.

The overall test results confirmed the conclusion of the analytical studies; i.e., the flared body geometry is superior to the wake-drogue configuration. The flow field patterns for the two geometries were similar, though separation was never bi-stable for the flared body. When the flare angle was reduced to 25 degrees, the desirable open cavity pattern was stable for all angles-of-attack and all forebodies. The configuration studies showed that a 25 degree flare provided adequate drag for the flared body (because of its packaging advantages), but inadequate drag for the wake-drogue. An additional advantage of the flared body demonstrated by wind tunnel data is that the drag is less sensitive to nosetip shape than the wake-drogue.

It was concluded that a recovery vehicle meeting all of the goals of the VRT Program is feasible. Designs are presented for vehicles with ballistic coefficients up to 3500 lb/ft^2 and peak dynamic pressures up to 160 atm . These vehicles should have stable aerodynamics both before and after low altitude recovery initiation.

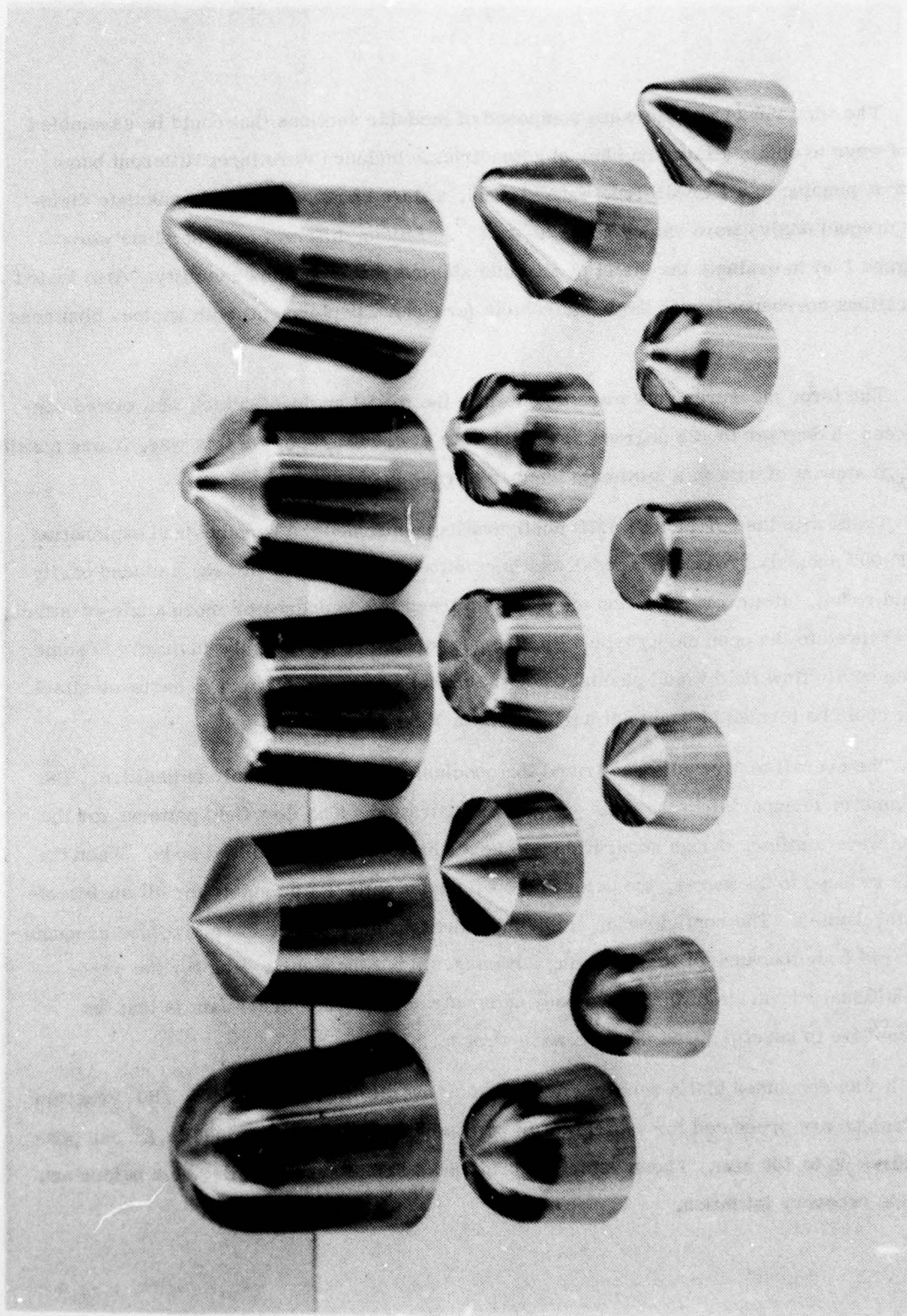


Figure 1-5. Model nosetips.

2.0 SIZING STUDY

Eight recovery vehicles (R/V's) were designed to satisfy four different nosetip recovery missions, to provide guidance in selecting wind tunnel model configurations. It was found that recovery vehicles should be designed for initiation altitudes below 20,000 feet, requiring that the ballistic coefficient drop by a factor of at least ten at recovery deployment. Both flared body and wake-drogue vehicles were designed for each mission and the flared body vehicles were found to be superior in every respect.

2.1 PERFORMANCE REQUIREMENTS

The basic requirement for a nosetip recovery vehicle is that recovery should not be initiated until nosetip recession is nearly complete. Figure 2-1 shows the recession history for a typical ICBM, and superimposed on the curve are recession histories for R/V's recovered at 15,000 feet for three ballistic coefficient ratios (ratio of ballistic coefficient before and after recovery initiation). It can be seen that nosetip recession is nearly complete at 15,000 feet, and that the magnitude of the recovery ballistic coefficient change has little effect on total recession. If recovery is initiated at very low altitude, the ballistic coefficient decrease after initiation must be very large to decelerate the R/V down to parachute deployment speed before impact. Figure 2-2 shows impact velocity as a function of recovery initiation altitude for the three ballistic coefficient ratios shown above and for the FLAME vehicle. This map illustrates the capability of the hypersonic decelerator concept to obtain the low subsonic terminal velocities necessary to avoid terminal decelerator design problems. Standard parachute designs and practices can be used for the terminal recovery system. It is seen that for the ballistic coefficient ratios of 12 and 18, deceleration is extremely rapid and the impact velocity is independent of initiation altitude over the range in initiation altitudes shown. In contrast, the R/V's with lower ballistic coefficient ratios have impact velocities that are strong functions of initiation altitude. This is an undesirable characteristic because the terminal recovery system would have to be overdesigned to be able to survive a reasonable range of off-nominal trajectories. The above considerations suggest that a recovery vehicle should be designed for initiation around 15,000 feet altitude to accomplish the nosetip recession test objective, and that the ballistic coefficient should decrease by a factor of ten or more at initiation to minimize terminal decelerator design problems.

2.2 VEHICLE DESIGN

Eight vehicles were designed to achieve specified nosetip recovery goals. Both wake-drogue and flared body vehicles were designed for four pre-recovery geometries. Each vehicle was

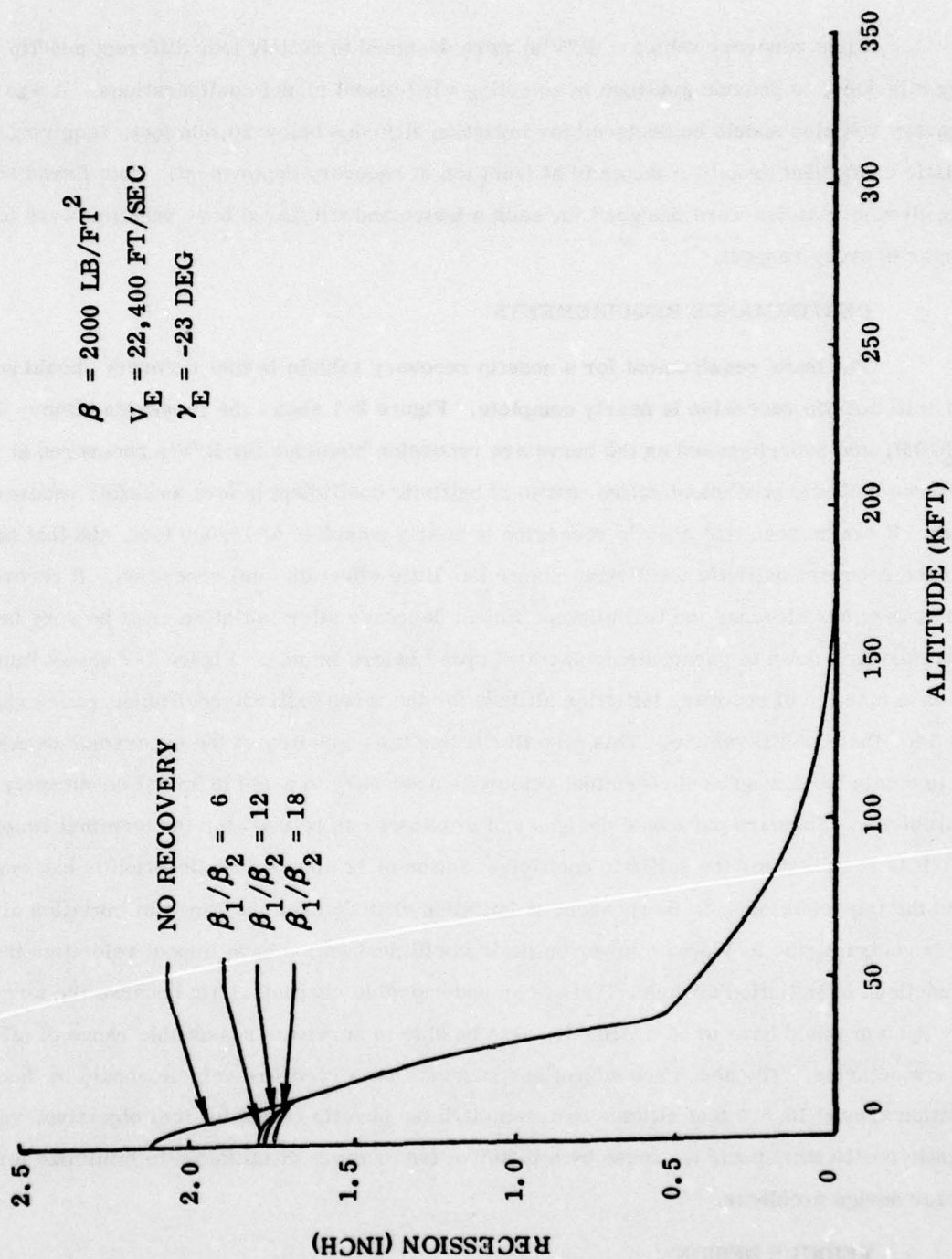


Figure 2-1. Stagnation point recession history comparison.

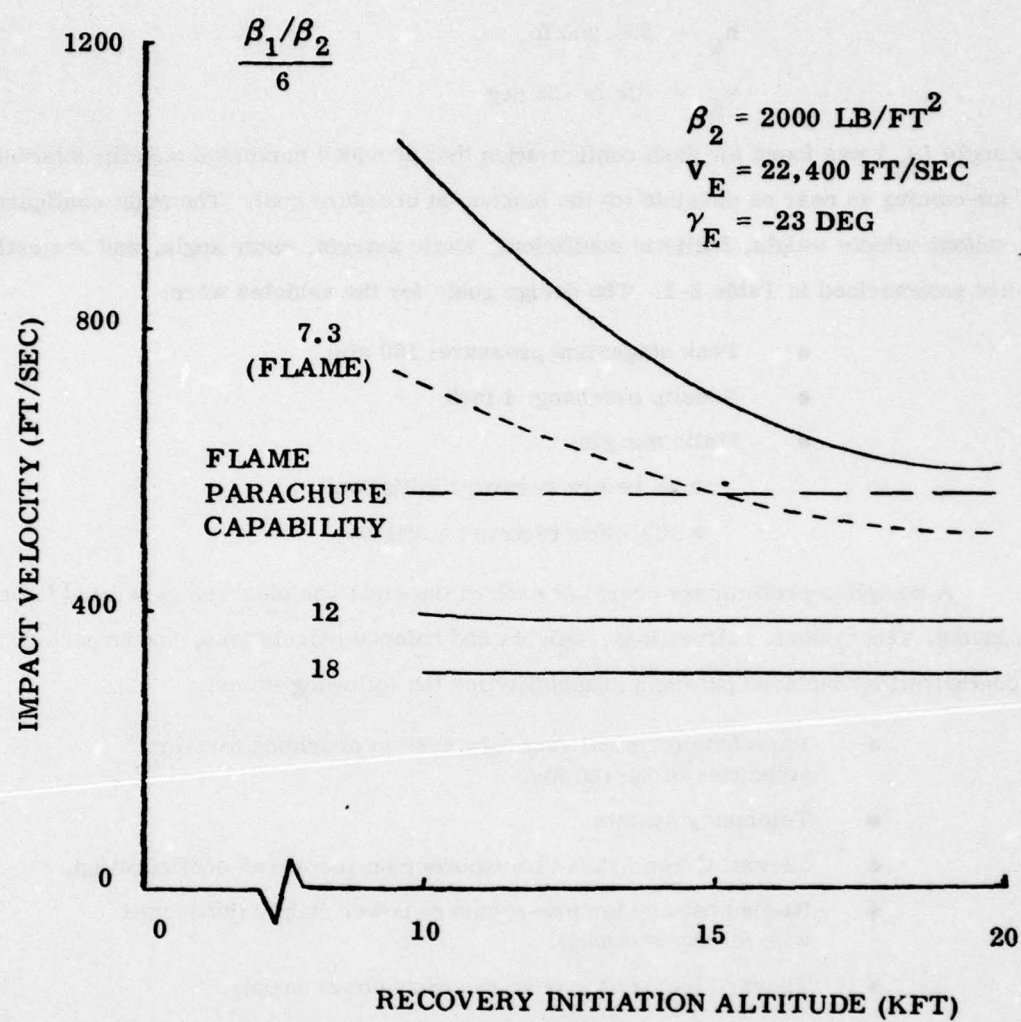


Figure 2-2. Effect of recovery ballistic coefficient charge on parachute requirements.

designed for ICBM trajectories having entry conditions:

$$V_E = 22,500 \text{ ft/sec}$$

$$h_E = 300,000 \text{ ft}$$

$$\gamma_E = -25 \text{ to } -35 \text{ deg}$$

The entry angle (γ_E) was found for each configuration that provided maximum nosetip ablation while achieving (or coming as near as possible to) the stagnation pressure goal. The eight configurations, and the resultant vehicle weight, ballistic coefficient, static margin, entry angle, and stagnation pressure are summarized in Table 2-1. The design goals for the vehicles were:

- Peak stagnation pressure: 160 atm
- Nosetip overhang: 4 inch
- Static margin:
 - > 5% before recovery initiation
 - > 10% after recovery initiation

A complete preliminary design of each of the eight vehicles was generated including packaging layout, aerodynamic calculations, weights and balance calculations, and trajectory analysis. All configurations included packaging capability for the following items:

- Parachute terminal recovery system providing terminal velocities of 80-180 fps.
- Telemetry system.
- 50-watt C-band radar transponder on recovered configuration.
- Ni-Cad battery for pre-recovery power supply (jettisoned with fairing sections).
- Thermal battery for post-recovery power supply.
- Nosetip recession instrumentation.
- 3-Axis rate gyros and accelerometers.
- Inertial fuze for recovery initiation.

Figures 2-3 through 2-8 show the packaging layouts developed for each of the eight vehicles. Table 2-2 summarizes the telemetry and electronics packaged.

Both 9.25-inch base diameter vehicles (1 and 2) and the 11-inch base diameter wake-drogue configurations (3 and 5) were somewhat space limited requiring a PAM FM/FM telemetry system. The remaining configurations allow incorporation of a PCM encoder.

Table 2-1. Flight configuration study matrix.

No.	Configuration Type	Base Dia. (in)	Cone Angle (deg)	Nosetip		Vehicle Length (in)	Vehicle Weight (lb)	Beta (PSF)	Static Margin (%)	γ_E (Deg)	P_{Omax} (ATM)
				Radius (in)	Overhang (in)						
1	Wake Drogue	9.25	6	.750	2.750	37.585	103	3600	19	25	160
2	Flare Body	9.25	6	.750	4.50	37.585	100	3600	11	25	160
3	Wake Drogue	11.0	6	.750	4.50	45.904	117	3290	16	27.5	160
4	Flare Body	11.0	6	.750	4.50	45.904	116	3270	11	27.5	160
5	Wake Drogue	11.0	6	1.375	4.50	40.594	150	2400	14	35	150
6	Flare Body	11.0	6	1.375	4.50	40.594	148	2370	8	35	150
7	Wake Drogue	17.0	6	2.25	4.50	61.597	321	1990	15	35	130
8	Flare Body	17.0	6	2.25	4.50	61.97	320	1990	6	35	130

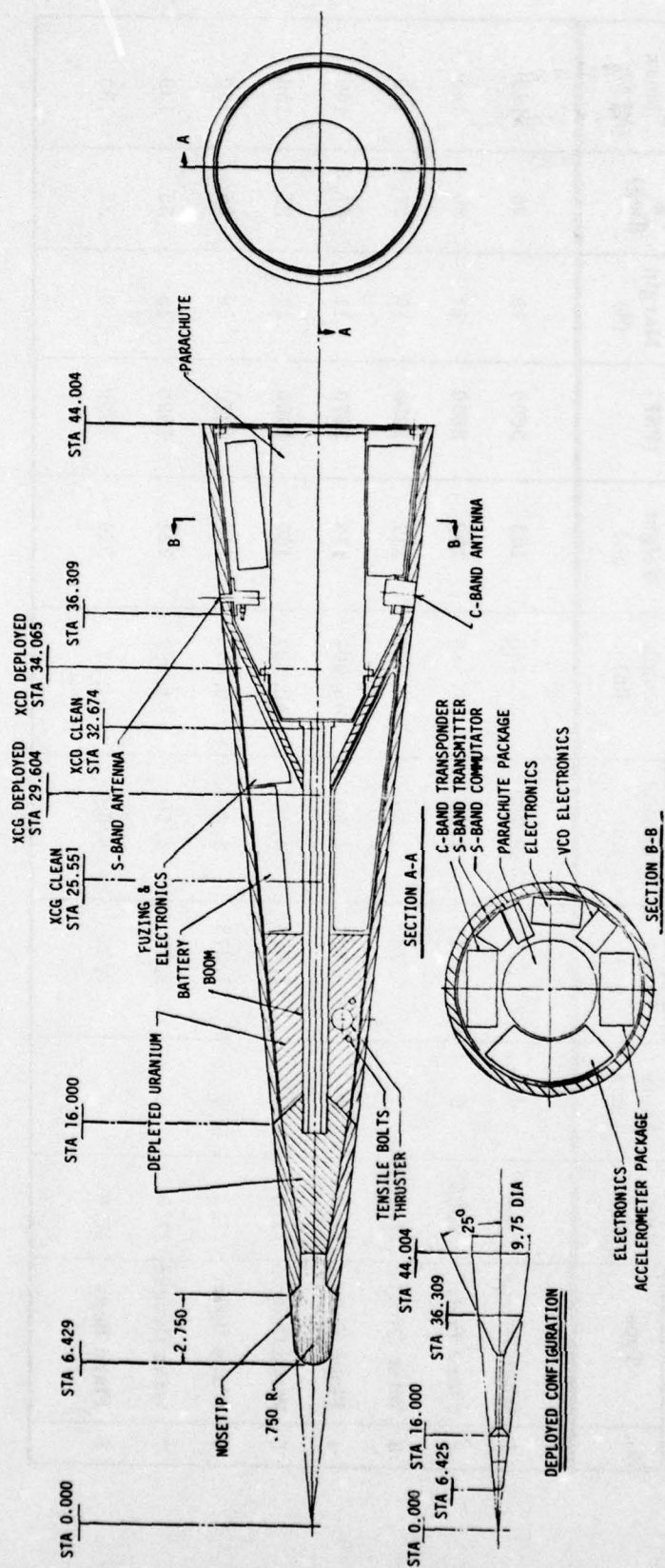


Figure 2-3. 9.25-inch base wake-droge.

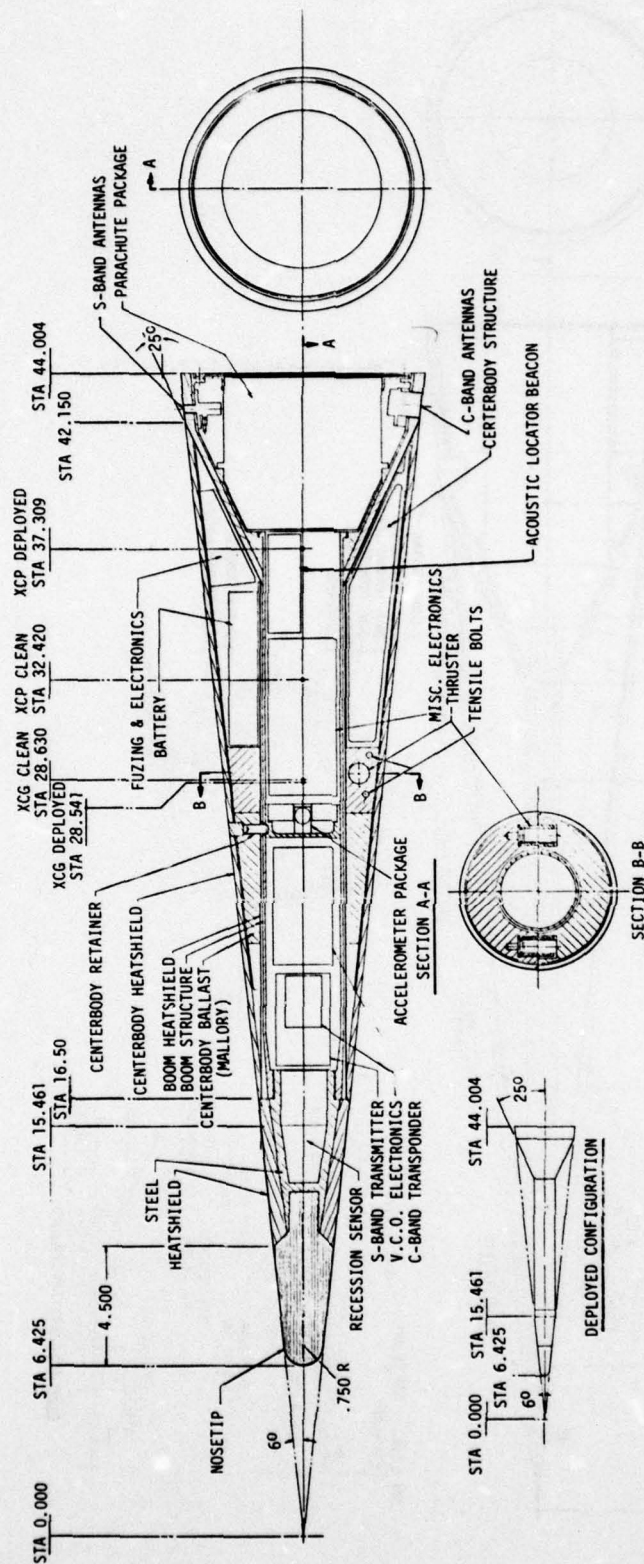


Figure 2-4. 9.25-inch base flared body.

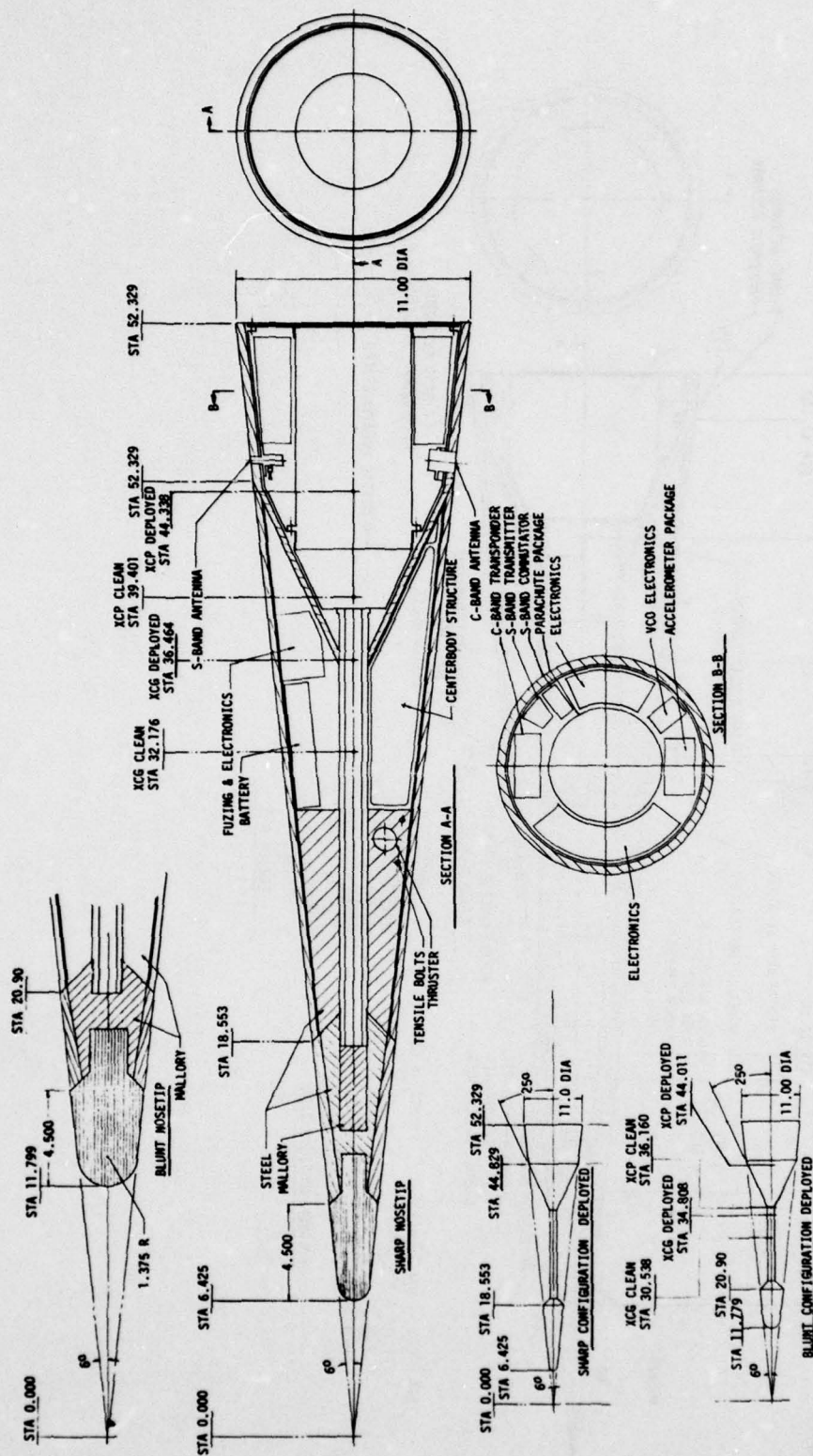


Figure 2-5. 10.0-inch base wake-drogue (sharp and blunt).

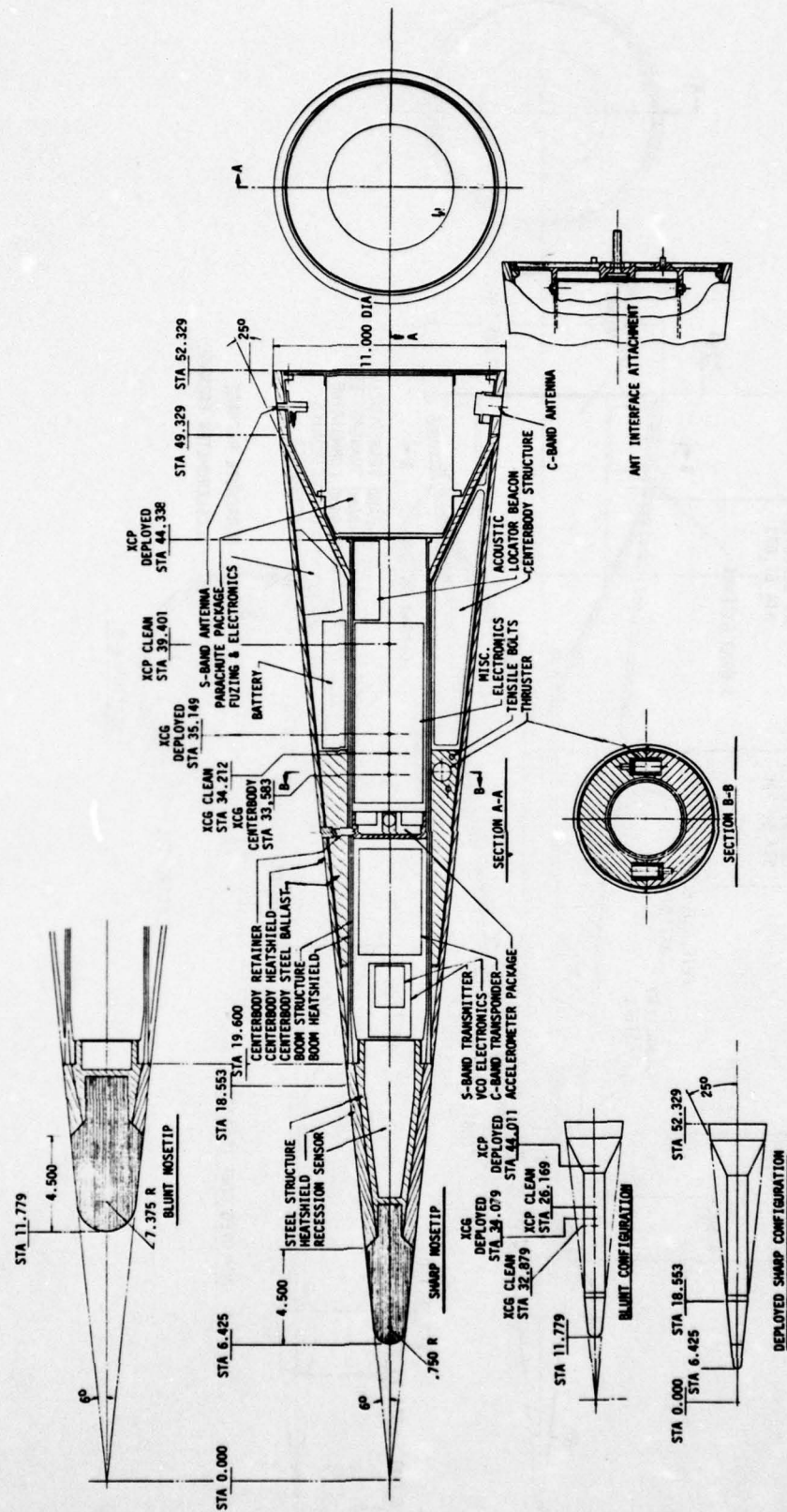


Figure 2-6. 11.0-inch base flared body (sharp and blunt).

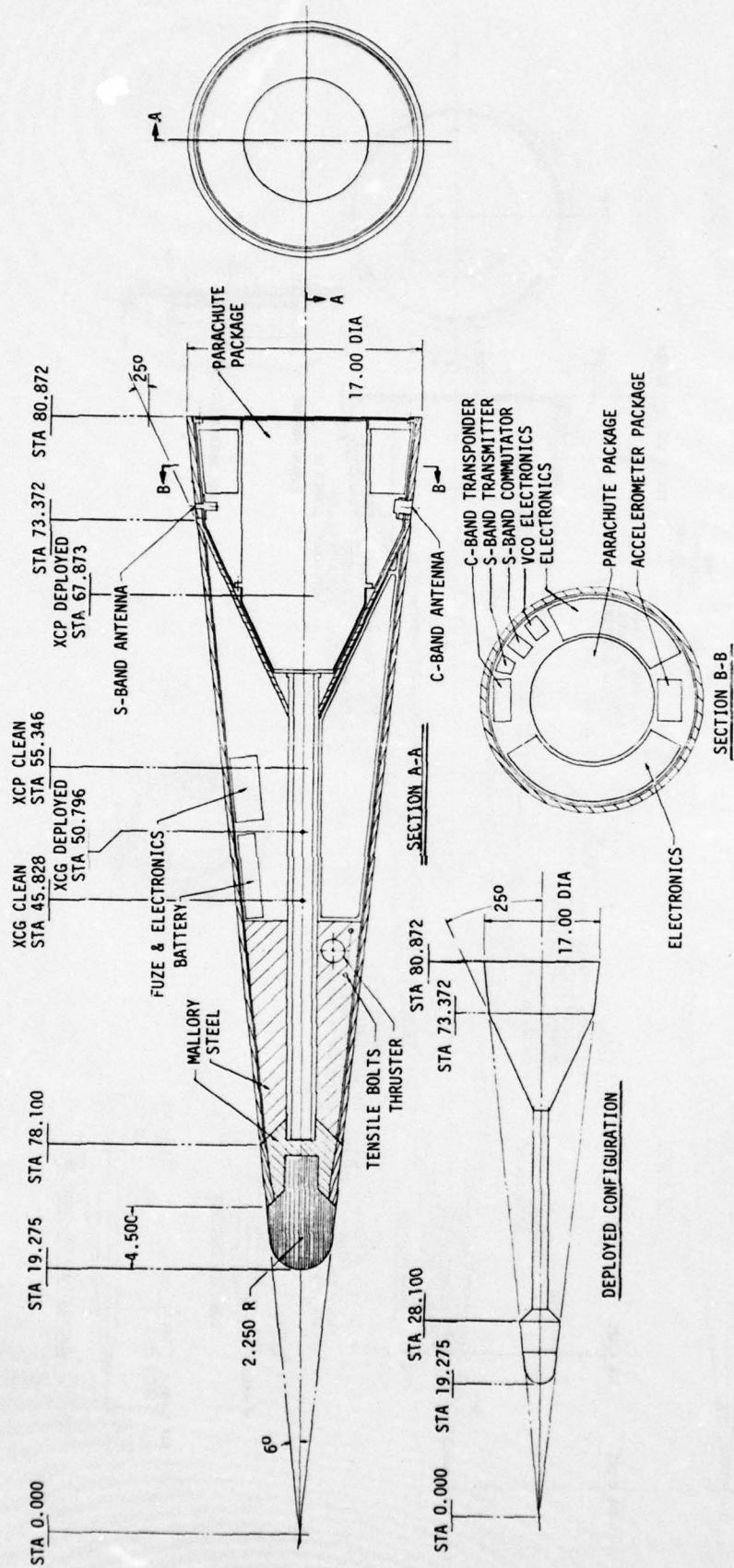


Figure 2-7. 17.0-inch base wake-drogue.

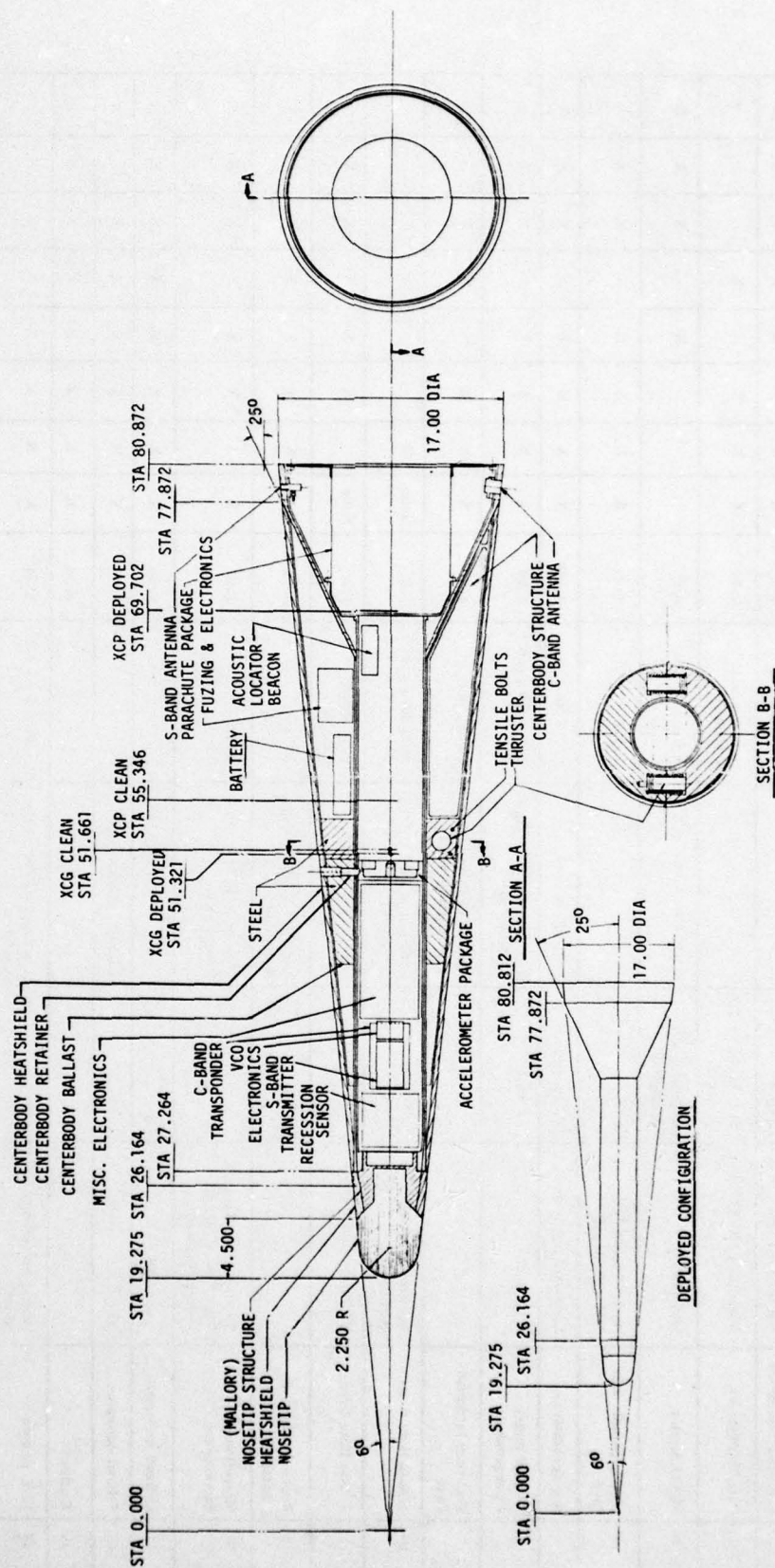


Figure 2-8. 17.0-inch base flared body.

Table 2-2. Recovery vehicle electronics packaging study.

No.	Components	Model and Manufacturer	Description	Comments	Size (in)	Weight (lbs)	Usage Configuration No.									
							1	2	3	4	5	6	7	8	9	10
1	Hi-Cad Battery Potting	GE GCT 1.5 Cells	26 Cells 1.5 Ah		1.004 dia x 1.13	3.73 0.75	X	X	X	X	X	X	X	X	X	X
2	Thermal Battery	Catalyst Research 4057-80			1.65 dia x 2.400	0.50	X	X	X	X	X	X	X	X	X	X
3	S-Band Transmitter	Microcom T-905	5 Watt		1 x 2 x 3.25	0.875	X	X	X	X	X	X	X	X	X	X
4	Pam Multiplexer	Microcom MC-27-34	Low Level 34 CH		1.51 x 2.95 x 1.26	0.38	X	X	X		X					
5	PCM Encoder	IED 410	62 Analog CH 32 Digital	MMP-600 1.75 x 1.5	1.5 x 3.25 x 4.25	0.75				X				X	X	X
6	VCDs, Mount, Min Amp	Aydin Vector MM-652 Mount			2.055 x 1.02 x 1.42	0.15	X	X	X	X	X	X	X	X	X	X
7	Accelerometers	Endevco 2262 Series	Piezoresistive	Min. of six used	0.610 dia	0.375	X	X	X	X	X	X	X	X	X	X
8	C-Band Radar Transponder	Vega 349C-4	50 Watt	Repackaged for Configuration 2 only	1.2 x 3.0 x 5.0	1.25	X	X	X	X	X	X	X	X	X	X
9	Recovery Initiation Fuse			Min. of 25 in ³ allowed for Configuration 2	25 in ³ min.	4.0	X	X	X	X	X	X	X	X	X	X
10	3-Axis Rate Gyro	Northrup Mod of P/N 79157		Proposal to PDA 28 July 75	2.77 dia x 4.0	1.3	None	X								
11	3-Axis Rate Gyro	US Time 402104-0			2.11 x 2.5 x 2.375	1.3	None		X	X	X	X	X	X	X	X
12	Recession Instrumentation	-----		Min. of 30 in ³ for Configuration 2	30 in ³	2.75	None	X	X	X	X	X	X	X	X	X
13	Miscellaneous Electronics	Transducers, Timers, Reg. Power Supply Power Dividers		Min. of 30 in ³ for Configuration 2	30 in ³	2.0	X	X	X	X	X	X	X	X	X	X
14	C-Band Antennas	Vega 820C-1				0.38	X	X	X	X	X	X	X	X	X	X
15	S-Band Antennas	GE		FLAME Antennas		0.38	X	X	X	X	X	X	X	X	X	X
16	Cables					0.50	X	X	X	X	X	X	X	X	X	X
17	UHF Beacon	Micro Electronics Model 151		Packaged in Parachute Canister	1.06 x 1 x 2 1/2	0.21 ⁽¹⁾	X	X	X	X	X	X	X	X	X	X
18	UHF Beacon Power Supply	PDA Part		Packaged in Parachute Canister	6 x 2 x 2 1/2	0.313 ⁽¹⁾	X	X	X	X	X	X	X	X	X	X
TOTAL WEIGHTS							15.3	19.3	19.3	19.7	19.3	19.7	19.7	19.7	19.7	19.7

(1) Included in parachute assembly weight

Configuration 1 lacks available packaging volume for either nosetip recession instrumentation or a 3-axis rate gyro assembly. However, configurations 4, 6, 7, and 8 have weight and volume capability for expanding the electronics well beyond the 20 pound system described. For example, they will accept the PDA multiray recession instrumentation which weighs approximately 5.5 pounds and requires approximately 60 cubic inches of packaging volume.

The components described are all catalogue items with the exception of the 3-axis rate gyro package, and the radar transponder in configuration 2. Data on the gyro package and transponder were obtained by direct communication with the component vendors.

Aerodynamic coefficients for the pre-recovery geometries were obtained using tabulated results of the computer code described in Reference 3. Aerodynamic coefficients for the recovery geometries were calculated using the approximate technique of superposition of sections to obtain total body coefficients. Coefficients for each section were obtained from the tabulation described above. Note that this technique implicitly assumes that the flow is attached over the entire body.

Table 2-3 and Figures 2-9 and 2-10 show samples of the final weight and balance code and trajectory code analyses for one of the eight vehicles.

Table 2-4 summarizes the recovery performance predicted for the eight designs. Comparing each pair of vehicles, it can be seen that in every case the flared body is more stable than the wake-drogue and allows recovery at the same or lower altitude. The reasons for this are shown in Figure 2-11. Due to its shape, the boom of the flared body provides efficient packaging for the electronic components minimizing the volume required in the flare. This allows the forward conical surface of the flare to be moved much farther aft than is possible on the wake-drogue. This repositioning results in a substantial increase in both drag area and stability.

2.3 CONCLUSIONS

The following conclusions were reached by comparing the wake-drogue and flared body designs for each of the four pre-recovery configurations:

- The flared body should have higher drag and a farther aft center-of-pressure than the wake drogue (assuming all attached flow).
- The flared body required less ballast than the wake-drogue. Consequently, the 9.25-inch base diameter flared body can achieve the 4-inch nosetip overhang goal, while the wake-drogue vehicle of the same size cannot.

Table 2-3. Typical weight and balance calculation summary.

Description	Weight	X-CG	Y-CG	Z-CG	RHO-X	RHO-Y	RHO-Z
Nosetip	0.906	9.647	0.000	0.000	0.654	3.754	3.754
Nosetip Structure	5.707	16.929	0.000	0.000	1.156	6.274	6.274
Nosetip Heatshield	2.070	15.581	0.000	0.000	1.437	5.487	5.487
Nosetip Assembly	8.683	15.848	0.000	0.000	12.29	341.40	341.40
Boom Heatshield	1.733	30.253	0.000	0.000	1.895	11.807	11.807
Boom	8.647	31.079	0.000	0.000	1.780	14.933	14.933
Structure Drogue	4.214	47.559	0.000	0.000	3.862	6.488	6.488
Drogue Heatshield	4.739	48.599	0.000	0.000	4.522	7.892	7.892
Drogue and Boom Assy	19.332	38.892	0.000	0.000	193.32	4062.61	4062.61
Parachute Assembly	8.000	48.300	0.000	0.000	.000	.000	.000
Telemetry & Electronics	10.000	33.000	0.000	0.000	.000	.000	.000
Antennas	0.750	50.500	0.000	0.000	.000	.000	.000
Deployed Configuration	46.766	35.149	0.000	0.000	205.61	9516.16	9516.16
Heatshield Centerbody	12.651	34.502	0.000	0.000	3.557	16.582	16.582
Structure Centerbody	6.095	36.348	0.000	0.000	3.682	17.567	17.567
Centerbody Mass	37.786	30.528	0.000	0.000	2.500	7.229	7.229
Shelf Structure	4.500	40.000	0.000	0.000	.000	.000	.000
Fuse and Electronics	4.000	42.000	0.000	0.000	.000	.000	.000
Ni-Cad Battery	4.500	39.000	0.000	0.000	.000	.000	.000
Centerbody Structure	69.532	33.583	0.000	0.000	478.84	8344.87	8344.87
Total Vehicle	116.298	34.212	0.000	0.000	684.45	17929.62	17929.62

AXIAL DECELERATION VS ALTITUDE
RN = .75 RB = 5.5

VE = 22500 FPS GAMMA = 35 DEG
110 LB VEHICLE 51 LB RECOVERED

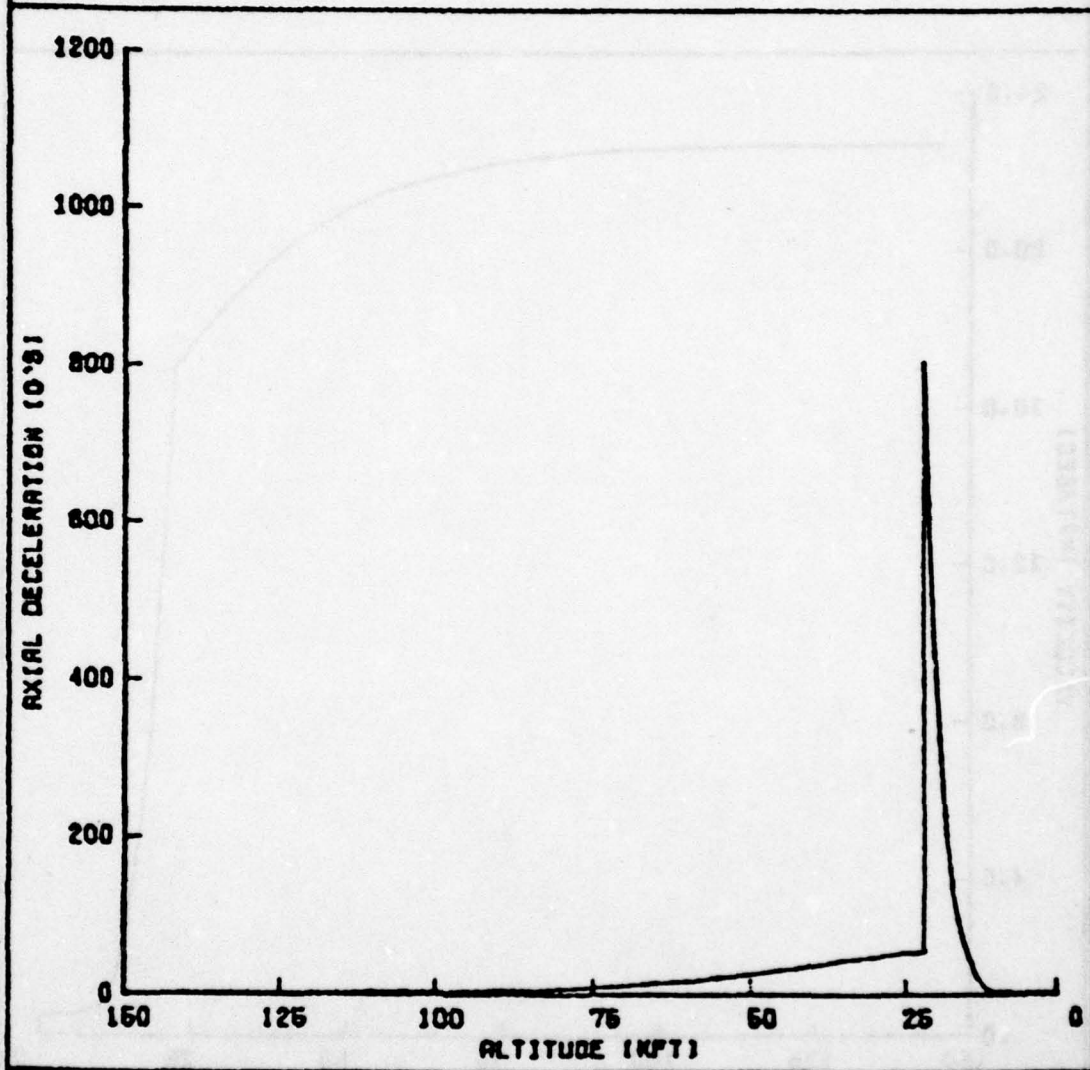


Figure 2-9. Typical deceleration profile.

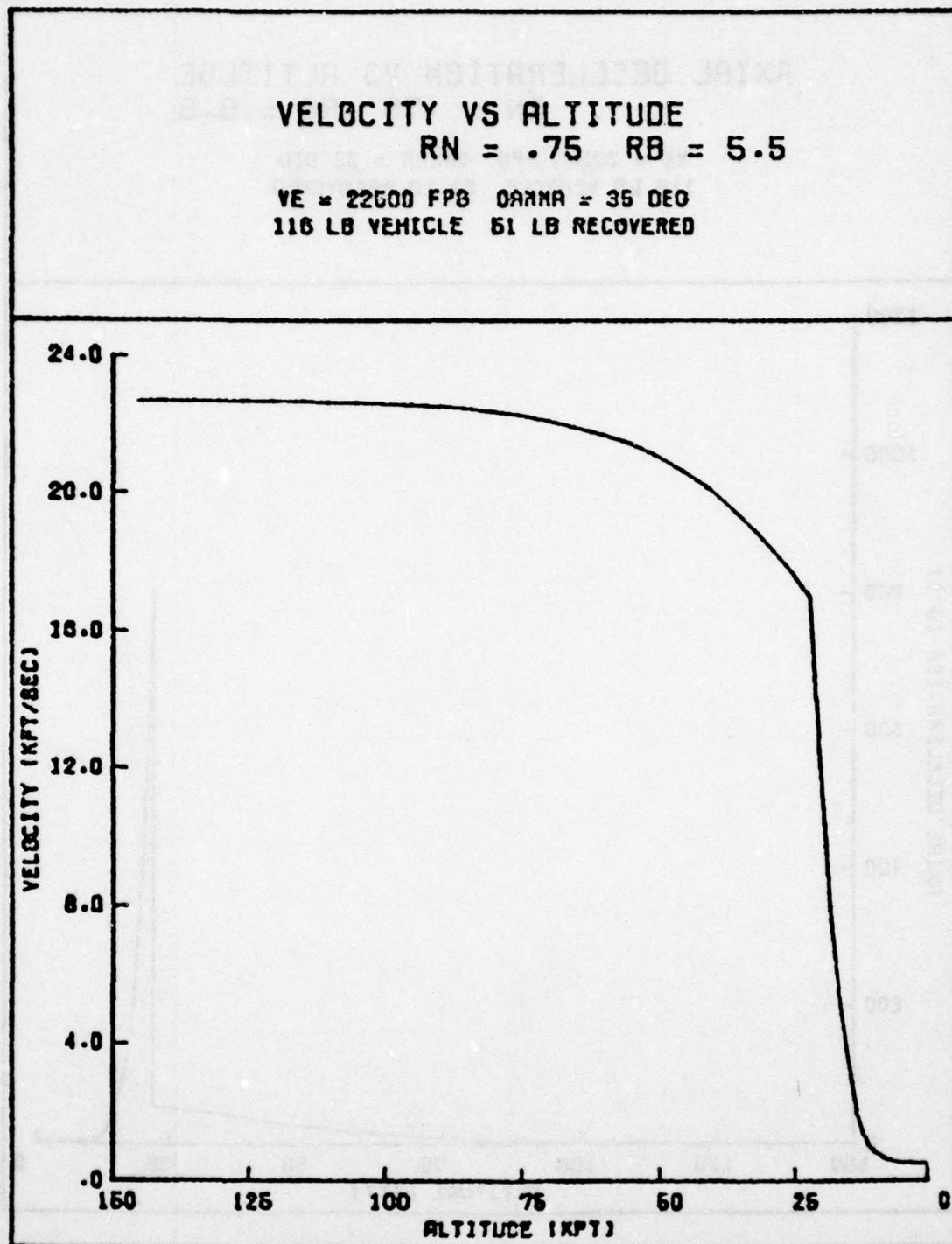


Figure 2-10. Typical velocity profile.

Table 2-4. Recovery performance predictions.

Configuration		Base Dia (in)	Nosetip Radius (in)	Recovered Weight (lb)	Altitude at ρ_{omax} (ft)	Static Margin (%)	Beta Change		Parachute Deployment Altitude (1) (ft)	Minimum Recovery Altitude (2) (ft)
No.	Type						$\beta_{\text{Clean}}/\beta_{\text{Deployed}}$	Weight Drag Total		
1	Wake Drogue	9.25	.750	42.0	21300	12	2.4	3.25	7.8	15300
2	Flare Body	9.25	.750	38.0	21300	24	2.6	5.6	15.	13800
3	Wake Drogue	11.0	.750	51.0	21700	10	2.3	5.0	11.5	15700
4	Flare Body	11.0	.750	47.0	21700	20	2.5	6.0	15.	13700
5	Wake Drogue	11.0	1.375	60.0	18900	14	2.5	3.2	8.0	18900
6	Flare Body	11.0	1.375	51.0	19000	24	2.9	3.9	11.3	15000
7	Wake Drogue	17.0	2.250	118.0	19900	28	2.7	3.8	10.4	13900
8	Flare Body	17.0	2.250	118.0	19900	30	2.7	3.9	10.5	13900

(1) Dynamic Pressure < 500 PSF after recovery initiated at ρ_{omax}

(2) Parachute Deployment at 1000 ft altitude

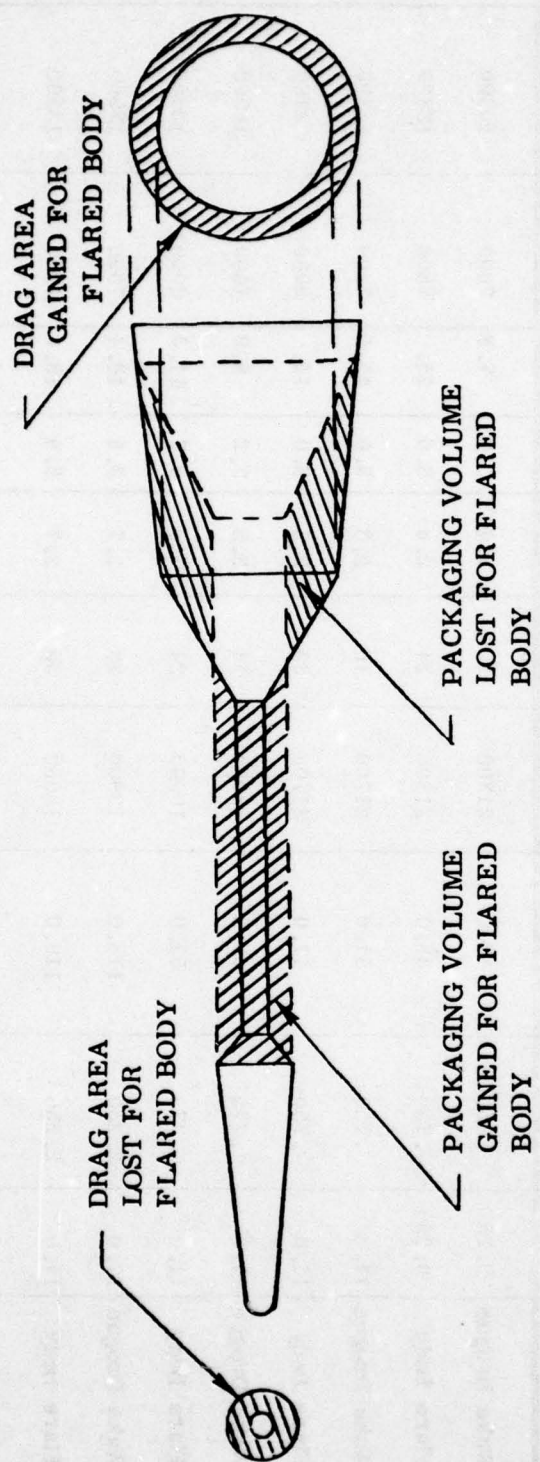


Figure 2-11. Drag area and volume comparison.

- Pre-recovery static margin of the flared body vehicle can be varied to suit the nosetip experiment objectives; however, a wake-drogue vehicle that meets the 10 percent recovery configuration static margin goal will necessarily have a pre-recovery static margin exceeding 14 percent.
- Due to the difference in volume available along the vehicle centerline, the flared body is better suited to nosetip recession sensor experiments than the wake-drogue.
- The larger diameter boom of the flared body has over triple the angle-of-attack capability of the wake-drogue.

goals:

The following conclusions were reached relative to the recovery vehicle performance

- The 0.75 inch nose radius vehicles evaluated could all achieve the 160 atm goal, while the blunter vehicles could not. Note: the blunter vehicles could also achieve that goal if their weight were increased with additional ballast. For example, vehicles 7 and 8 would reach 160 atm if their weights were increased approximately 70 pounds.
- Peak stagnation pressures occur around 20,000 feet altitude. All the vehicles designed can be safely recovered at or below that altitude using a single stage subsonic parachute.

3.0 WIND TUNNEL TESTS

Static stability and axial-force data were obtained on 101 configurations at Mach numbers 3.01, 4.02, and 5.05 and free-stream unit Reynolds numbers of 2, 4, and 4 million per foot, respectively. Effects of configuration nose shape, nose bluntness ratio, boom size, drogue angle, and drogue location on vehicle performance were investigated. Qualitative heat-transfer rate data were obtained simultaneously with the force data at Mach number 5 on 32 configurations to determine the effectiveness of the trip devices in producing turbulent flow forward of the drogue surfaces. The angle-of-attack range was from -5 to 12 degrees at zero sideslip. A complete listing of the test data is contained in Reference 4.

3.1 FACILITY SELECTION

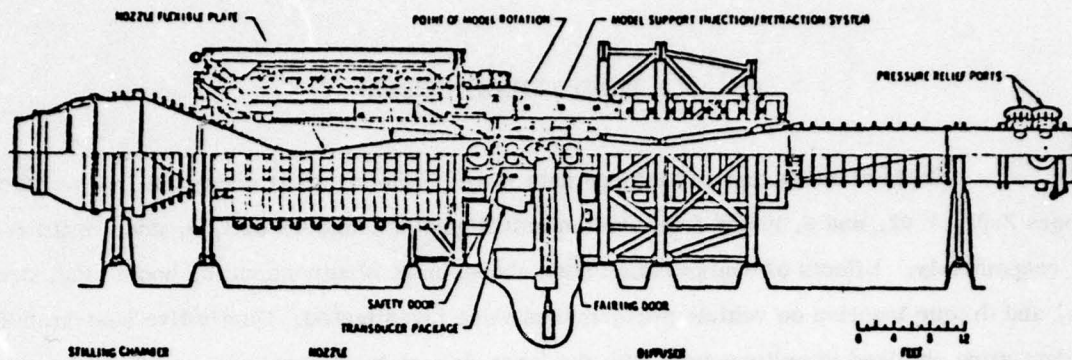
An evaluation of wind tunnels for this test series was conducted, and Supersonic Wind Tunnel A of the von Karman Gas Dynamics Facility at Arnold Engineering Development Center (AEDC), Air Force Systems Command (AFSC), located at Arnold Air Force Station, Tennessee was selected. This facility was chosen for the following reasons:

- Reynolds number: Turbulent flow over essentially the entire model was required.
- Mach number: The Mach number range of tunnel A brackets the Mach number at which the FLAME drag anomaly was observed.
- Economy: Tunnel A allows more runs per 8-hour shift than any other tunnel considered. Due to the very large number of runs planned, this was an important consideration.
- Visual observation: Direct observation and shadowgraph photography of the critical vehicle center section is possible. This is not true in tunnel B.
- Model interchangeability: If higher Mach number data should be desired at a later time, a model designed for Tunnel A can also be used in Tunnel B.

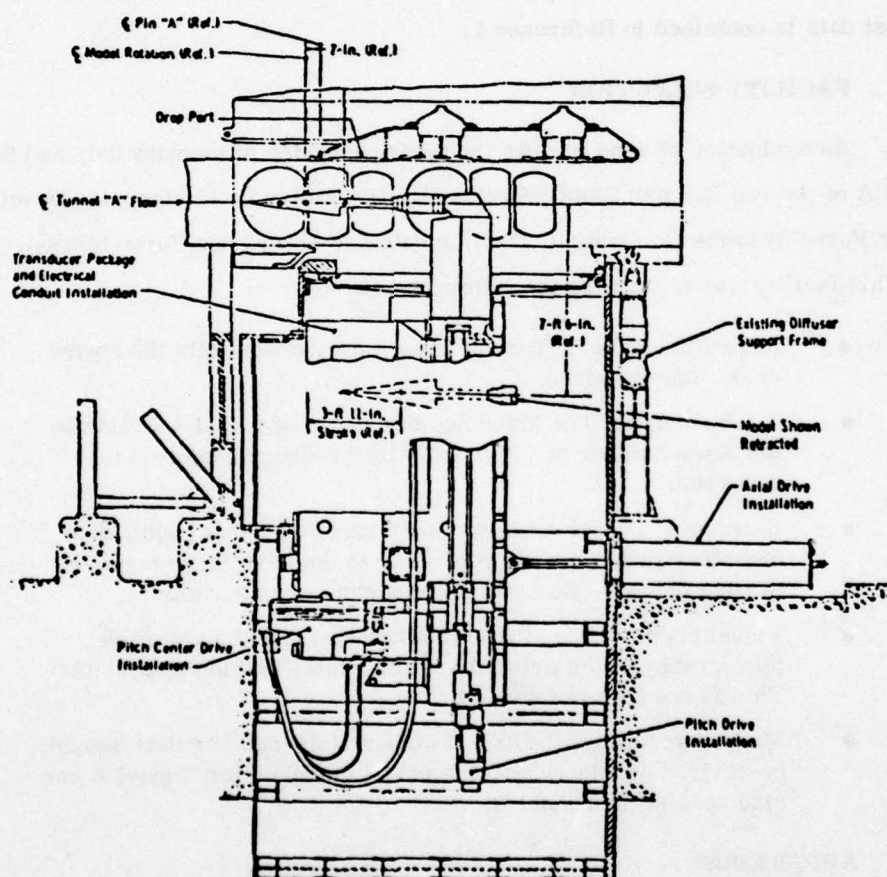
3.2 APPARATUS

3.2.1 Wind Tunnel

Tunnel A (Figure 3-1) is a continuous, closed-circuit, variable density wind tunnel with an automatically driven flexible-plate-type nozzle and a 40- by 40-inch test section. The tunnel can be operated at Mach numbers from 1.5 to 6 at maximum stagnation pressures from 29 to 200 psia, respectively, and stagnation temperatures up to 750°R ($M = 6$). Minimum operating pressures range



a. VKF Tunnel A



b. Model injection system.

Figure 3-1. Wind tunnel and model injection system.

from about one-tenth to one-twentieth of the maximum at each Mach number. The tunnel is equipped with a model injection system which allows removal of the model from the test section while the tunnel remains in operation. A description of the tunnel and airflow calibration information may be found in Reference 5.

3.2.2 Model

The basic geometry of the recovery and pre-recovery configurations nose components, and trip devices is shown in Figures 3-2 through 3-4. The model was designed as a flexible static force model which incorporated features to facilitate configuration changes. The pre-recovery model (Figure 3-2a) was a six degree half-angle cone with a 15-inch base diameter. The recovery configurations are shown in Figures 3-2b, c and d. The nose components (Figure 3-3) and trip devices (Figure 3-4) were interchangeable among all configurations. Tables 3-1 and 3-2 list the actual dimensions of each model nosetip. Most runs employed 0.040 trips, although the heat transfer data indicated that turbulent flow was achieved over essentially the entire model even when no trips were used.

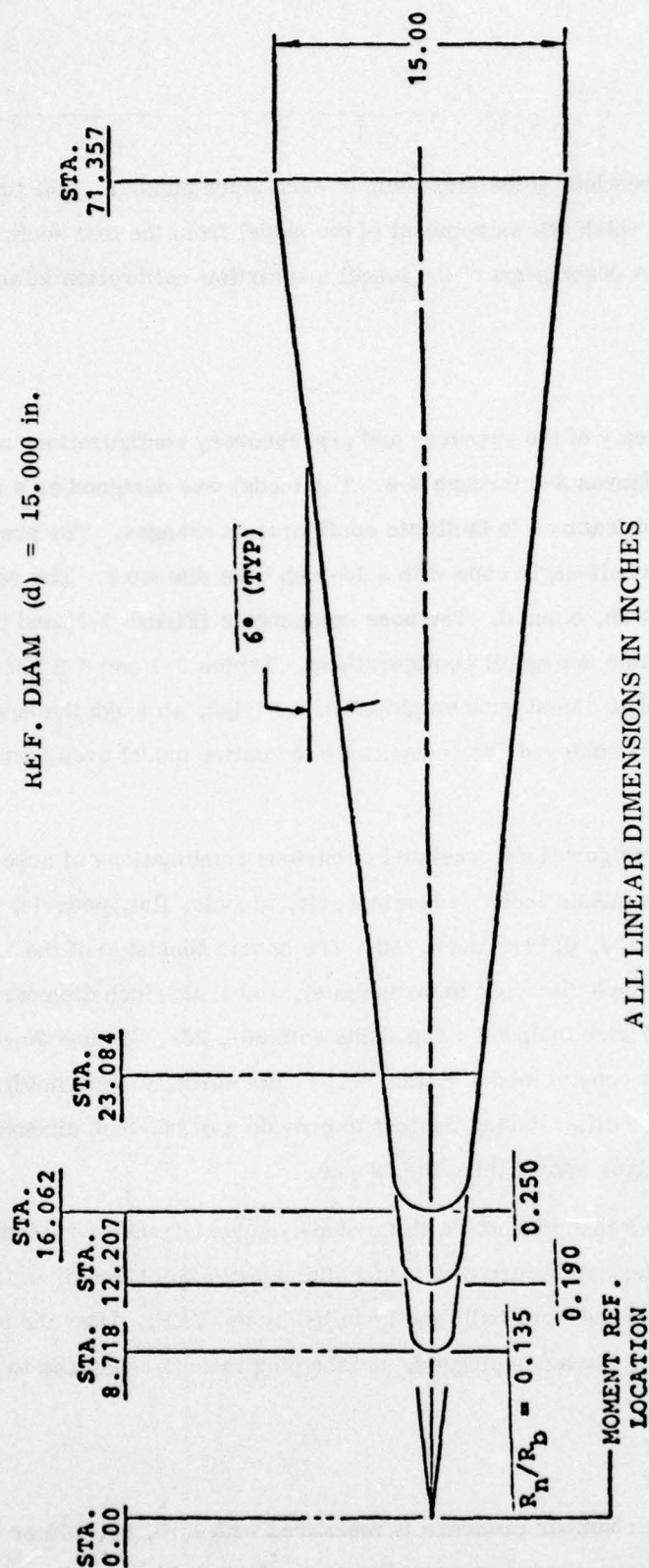
The recovery configurations consisted of various combinations of nose, boom, and drogue components. Nose components included hemispheric, biconic, flat, pedoric, and asymmetric shapes of bluntness ratios of 0.135, 0.190, and 0.250. The booms consisted of the 1.864-inch diameter FLAME flight test, 3.464-inch diameter (intermediate), and 4.852-inch diameter (large) cylindrical sections. Drogue geometries included components with 20-, 25-, 30- and 35-degree forward angle which joined the 6-degree cone at model station 55.541 (forward), 61.600 (mid), or 68.200 (aft). The 30-degree aft drogue was modified during the test to provide a 0.125-inch circumferential gap to bleed off part of the boundary layer approaching the drogue.

Model components instrumented with Gardon-type heat-transfer rate gages (Reference 6) are shown in Figure 3-5. The gages were 0.250-inch diameter, except for six 0.125-inch diameter gages on the FLAME boom, and were built and installed by the VKF. After the test was completed, the gages were removed, the holes plugged, and the plug inserts contoured to the model surfaces.

3.2.3 Instrumentation

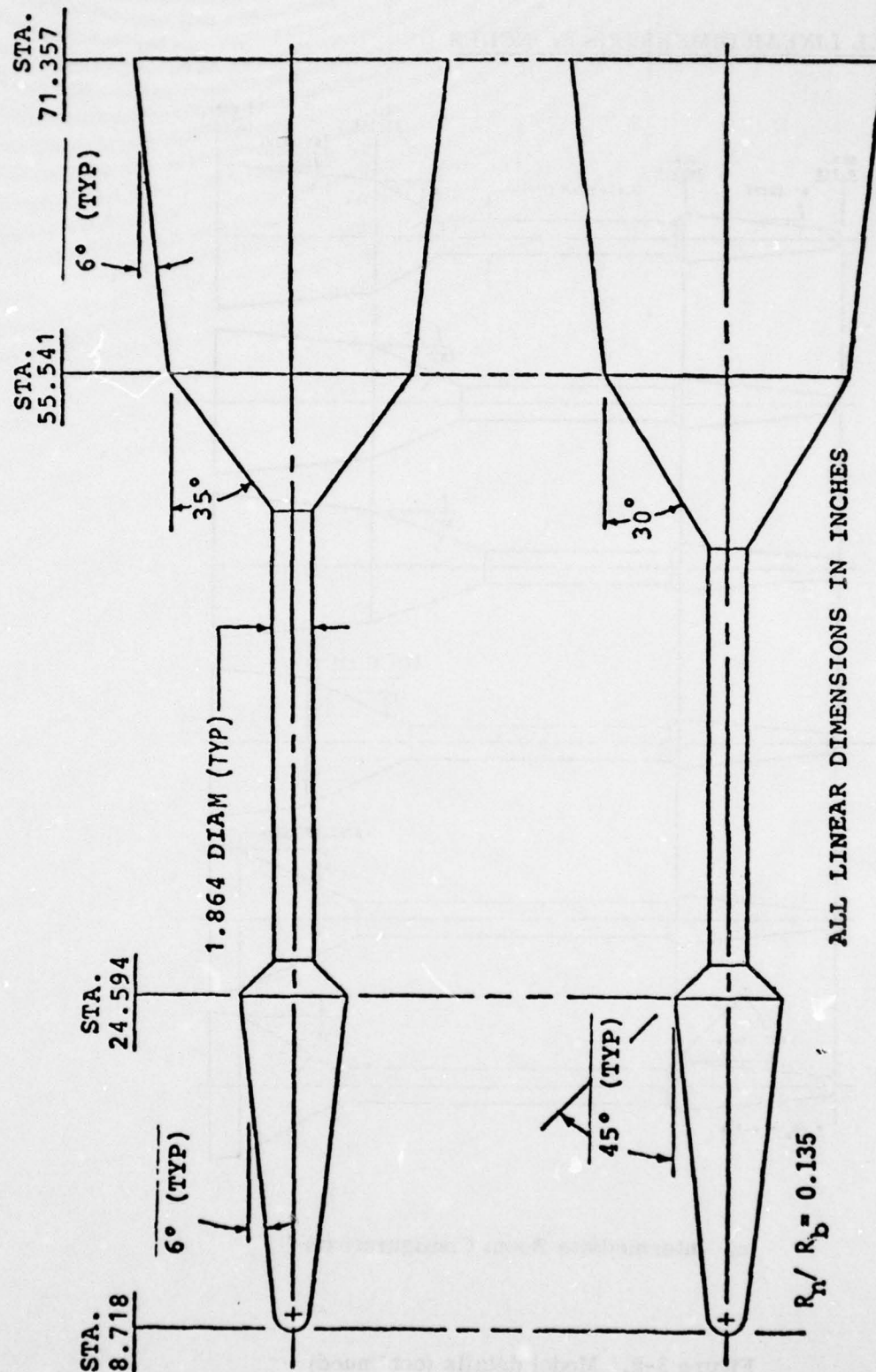
Tunnel A stilling chamber pressure is measured with a 15, 60, 150 or 300 psid transducer referenced to a near vacuum. Based on periodic comparisons with secondary standards, the uncertainty (a bandwidth which includes 95 percent of the residuals) of these transducers is estimated to be within ± 0.2 percent of reading or ± 0.015 psia, whichever is greater. Stilling chamber

REF. AREA (S) = 176.715 in.^2
 REF. DIAM (d) = 15.000 in.



a. Basic Cone Configuration

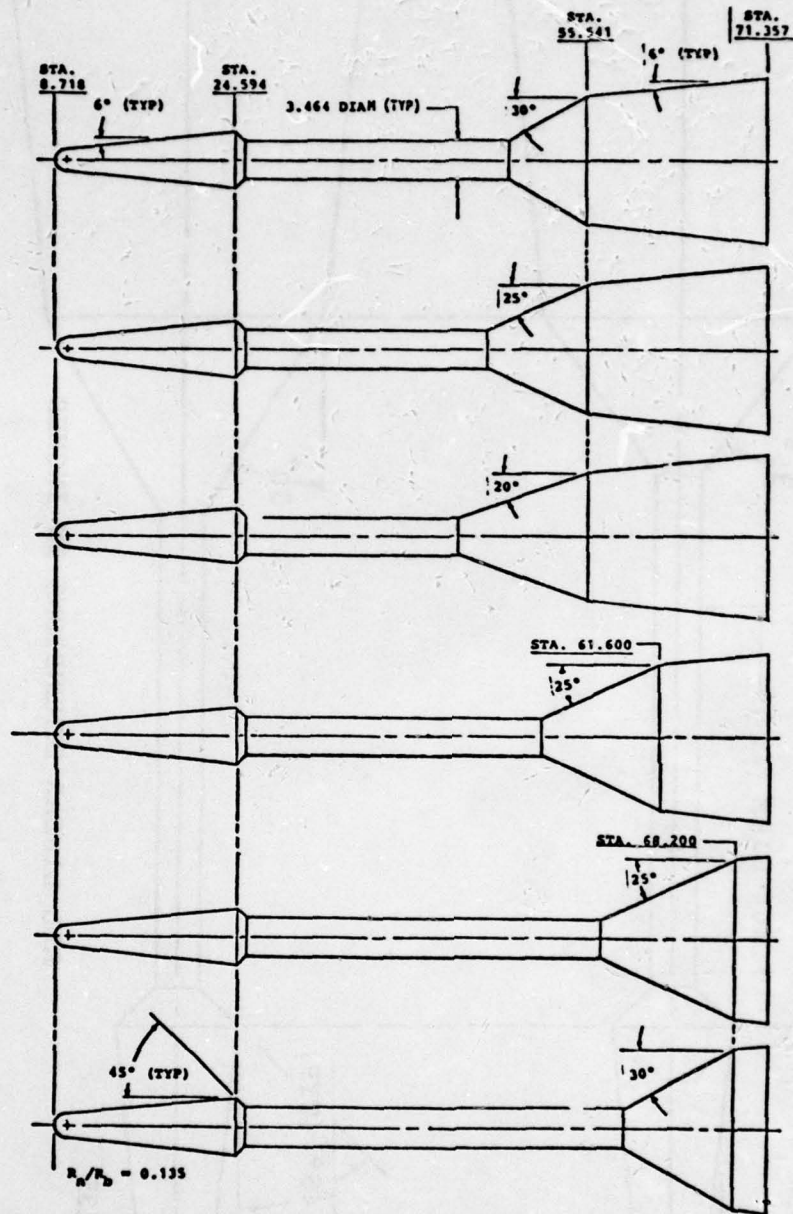
Figure 3-2. Model details.



b. FLAME Boom Configuration

Figure 3-2. Model details (continued).

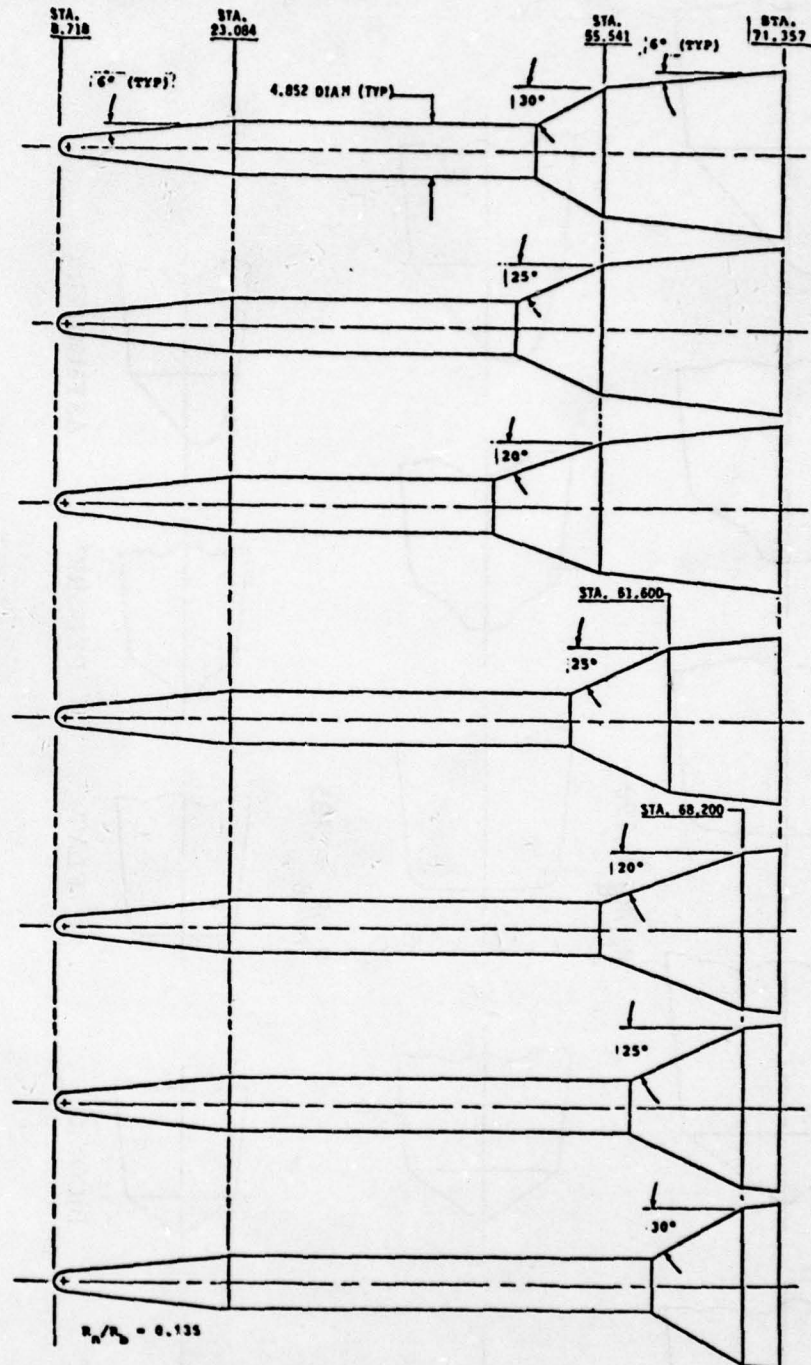
ALL LINEAR DIMENSIONS IN INCHES



c. Intermediate Boom Configurations

Figure 3-2. Model details (continued)

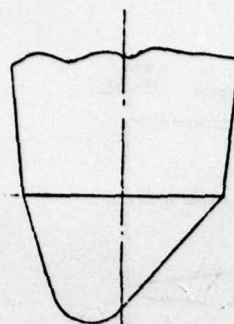
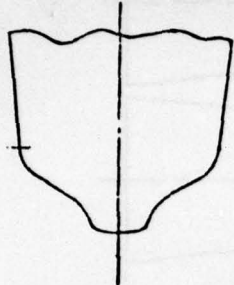
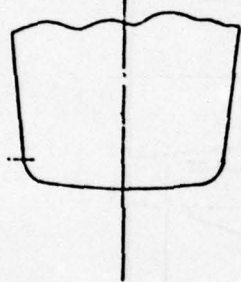
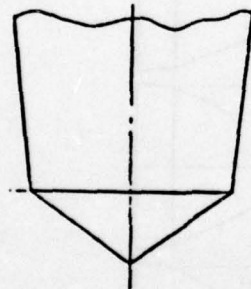
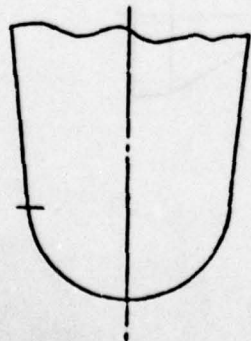
ALL LINEAR DIMENSIONS IN INCHES



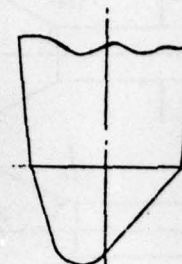
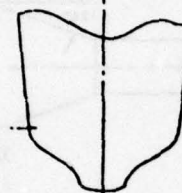
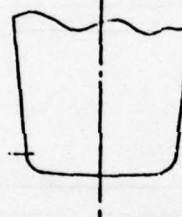
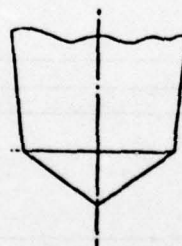
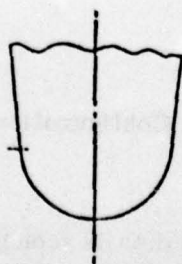
d. Large Boom Configurations

Figure 3-2. Model details (concluded).

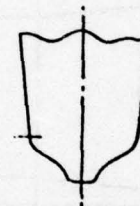
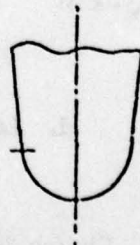
$$R_N/R_B = .25$$



$$R_N/R_B = .190$$



$$R_N/R_B = .135$$



HEMISPHERIC

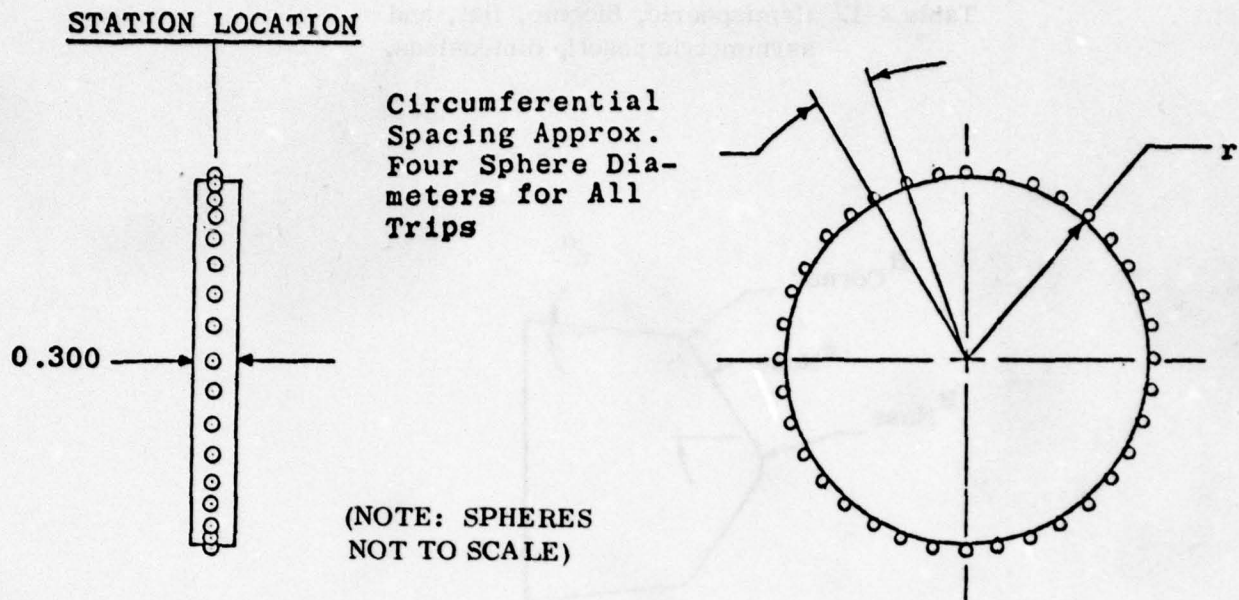
BICONIC

FLAT

PEDORIC

ASYMMETRIC

Figure 3-3. Nosetips.

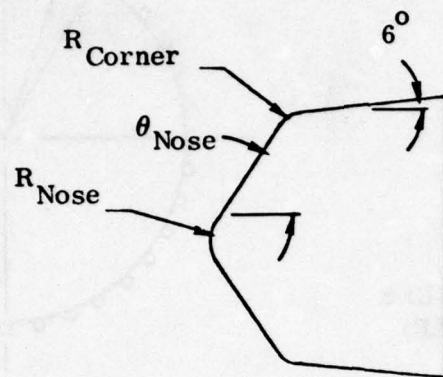


R_n/R_b	Station	r	Trip Diam	No.
0.250	21.634	2.275	0.025	143
			0.040	89
0.190	15.958	1.700	0.025	107
			0.040	63
0.135	11.368	1,200	0.025	75
			0.040	47

ALL DIMENSIONS IN INCHES

Figure 3-4. Boundary layer trips.

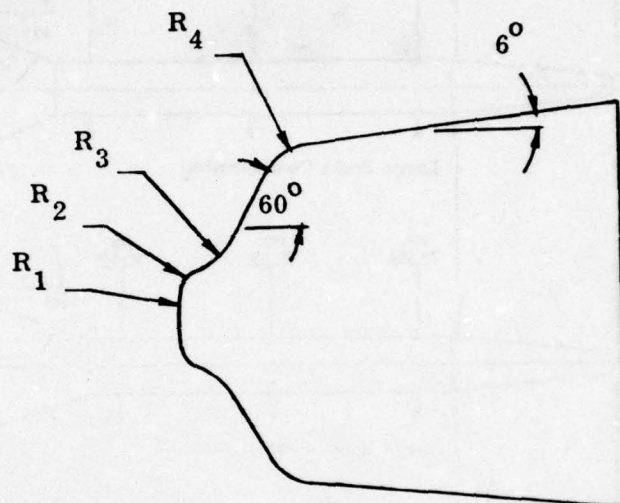
Table 3-1. Hemispheric, biconic, flat, and asymmetric nosetip dimensions.



All Radii Tangent

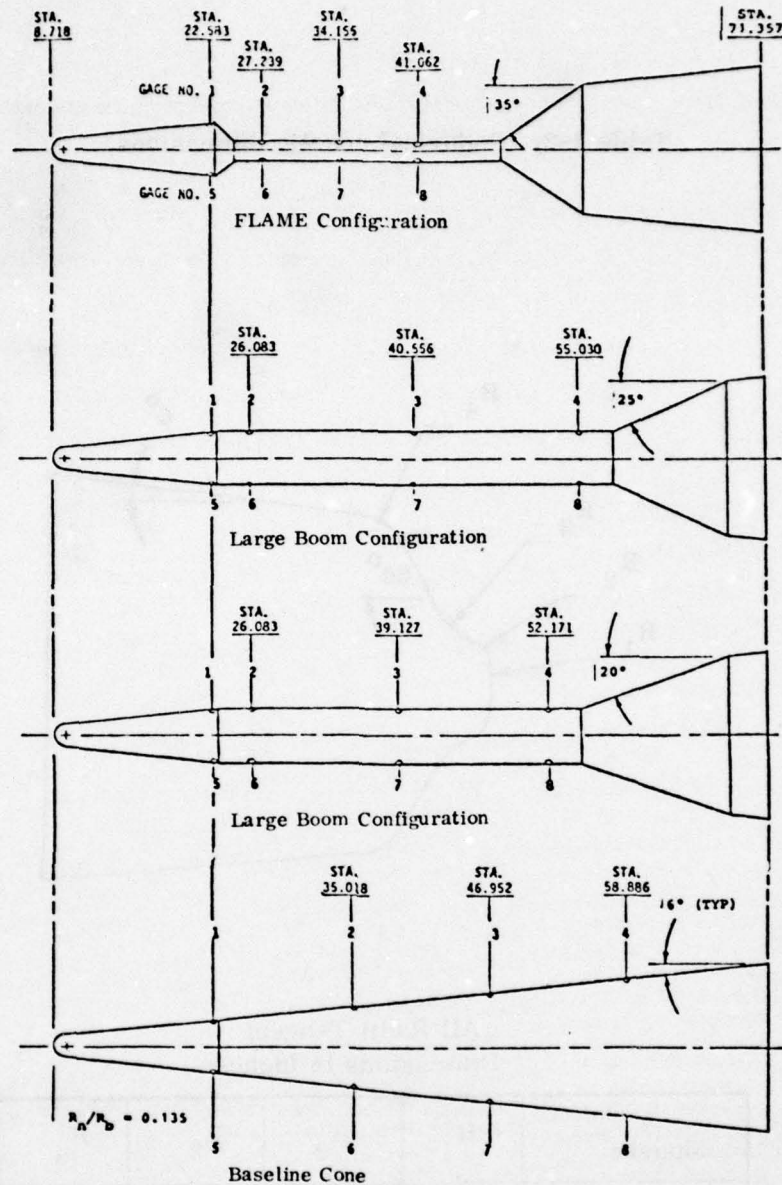
Model	Bluntness	R_{Nose} (inch)	θ_{Nose} (deg)	R_{Corner} (inch)
Hemisphere	0.135	1.018	—	—
	0.190	1.425	—	—
	0.250	1.875	—	—
Biconic	0.135	0.125	55	0.015
	0.190	0.125	55	0.015
	0.250	0.125	55	0.015
Flat	0.135	12.000	—	0.250
	0.190	12.000	—	0.375
	0.250	12.000	—	0.500
Aysmmetric	0.135	0.407	42/18	0.015
	0.190	0.507	42/18	0.015
	0.250	0.750	42/18	0.015

Table 3-2. Pedorical nosetip dimensions.



All Radii Tangent
Dimensions in Inches

Model	R ₁	R ₂	R ₃	R ₄
Small	1.000	0.125	0.500	0.375
Intermediate	1.400	0.175	0.700	0.525
Large	1.842	0.230	0.921	0.691



Note: All gages 0.250-in. diam except gages 2-4 and 6-8 on FLAME configuration. Gages top and bottom dead center.

Figure 3-5. Gardon gage location.

temperature is measured with a copper-constantan thermocouple with an uncertainty of $\pm 3^{\circ}\text{F}$ based on repeat calibrations.

Model forces and moments were measured with a six-component, moment type, strain-gage balance supplied and calibrated by VKF. Prior to the test, static loads in each plane and combined static loads were applied to the balance to simulate the range of loads and center-of-pressure locations anticipated during the test. The following uncertainties represent the bands of 95 percent of the measured residuals, based on differences between the applied loads and the corresponding values calculated from the balance calibration equations included in the final data reduction. The range of check loads applied and the measurement uncertainties follow.

Component	Balance Design Load	Calibration Load Range	Range of Check Load	Measurement Uncertainty
Normal force, lb	± 1000	± 500	50-200	± 5.0
Pitching moment, *in lb	± 4750	± 4750	300-1200	± 16.0
Side force, lb	± 500	± 250	---	± 4.0
Yawing moment, *in lb	± 2375	± 2375	---	± 6.0
Rolling moment, in lb	± 750	± 165	---	± 2.1
Axial force, lb	± 300	± 300	---	± 1.6

*About balance forward moment bridge.

The transfer distance from the balance forward moment bridge to the model moment reference location was 57.159-inch along the longitudinal axis and was measured with an estimated precision of ± 0.005 inch.

Two model base pressures were measured with 15-psid transducers reference to a near vacuum and having full-scale calibrated ranges of 1, 5, and 15 psia. Based on periodic comparisons with secondary standards, the precision is estimated to be ± 0.2 percent of full scale of the range being used. An additional model base pressure was measured with a fast-response 1-psid transducer referenced to a near vacuum and mounted on the sting just downstream of the base such that the transducer sensing tube was within 0.3 inches of the model base. The precision of this transducer is estimated by the manufacturer to be ± 0.08 percent.

The model surface heat-transfer rates were measured with a high sensitivity gage that operates on the Gardon gage principle (Ref. 7), but has an order of magnitude higher sensitivity.

This gage was developed at AEDC/VKF for use in continuous wind tunnels. The gages were calibrated using a radiant heat source and exposing one or more test gages and heat-transfer standards to the same incident heat flux and measuring the output from each simultaneously. The heat-transfer standards have been checked by two independent organizations and found to agree within ± 4 percent. Accuracy of the test calibrations is estimated to be within ± 5 percent and gage repeatability and linearity are estimated to have been within ± 3 percent. Internal to each heat gage, a copper-constantan thermocouple was installed to monitor the gage edge temperature.

Model flow-field photographs were obtained with a double-pass optical flow visualization system with a 35-inch diameter field of view.

3.3 PROCEDURE

3.3.1 Test Conditions

The test was conducted at Mach numbers of 3.01, 4.02, and 5.05 and a free-stream unit Reynolds of 2, 4, and 4 million per foot, respectively. A summary of the nominal test conditions at each Mach number is given below.

M_∞	P_o , psia	T_o , $^{\circ}\text{R}$	q_w , psia	p_w , psia	$Re_\infty \times 10^{-6}$
3.01	15.0	590	2.55	0.40	2.0
4.02	50.0	590	3.64	0.32	4.0
5.05	93.0	640	2.96	0.17	4.0

A test summary showing all configurations tested and the variables for each is presented in Table 3-3. The designation of the model components of each specific configuration is shown in Table 3-4.

3.3.2 Test Procedure

3.3.2.1 General

During tests in Tunnel A, the model is mounted on a sting support mechanism located in an installation tank directly underneath the tunnel test area. The tank is separated from the tunnel by a pair of fairing doors and a safety door. When closed, the fairing doors, except for a slot for the pitch sector, cover the opening to the tank and the safety door seals the tunnel from the tank. After the model is prepared for a test run, the personnel access door to the tank is closed, the tank is vented to the tunnel flow, the safety and fairing doors are opened, and the model is injected into the

Table 3-3. Test summary data group numbers.

CONFIG. NO.	NOSE SHAPE	BLUNT. RATIO	BOOM SIZE	DROGUE ANGLE, DEG.	DROGUE STATION	TRIP SIZE, IN.	MACH NUMBER		
							3.01	4.02	5.05
11111	HEMI	0.135	CLEAN	CLEAN	CLEAN	NONE			91*
11121	↓	0.190	↓	↓	↓	↓			90*
11131		0.250	↓	↓	↓	↓			89*
11123	FLAT	0.190	↓	↓	↓	↓			96*
11124	PEDOR	↓	↓	↓	↓	↓			95
11115	ASYM	0.135	↓	↓	↓	↓			92
11125	↓	0.190	↓	↓	↓	↓			93
11135	↓	0.250	↓	↓	↓	↓			94
22321	HEMIS	0.190	INTER	20	FWD	0.040			61
22312	BICON	0.135	↓	↓	↓	↓			58
22322	↓	0.190	↓	↓	↓	↓			59
22332	↓	0.250	↓	↓	↓	↓			60
22323	FLAT	0.190	↓	↓	↓	↓			62
22324	PEDOR	↓	↓	↓	↓	↓			63
22325	ASYM	↓	↓	↓	↓	↓			64
22412	BICON	0.135	LARGE	↓	↓	↓			65
22422	↓	0.190	↓	↓	↓	↓			66
22432	↓	0.250	↓	↓	↓	↓			67
23321	HEMIS	0.190	INTER	25	↓	↓			71
23312	BICON	0.135	↓	↓	↓	↓			68
23322	↓	0.190	↓	↓	↓	↓			69
23332	↓	0.250	↓	↓	↓	↓			70
23323	FLAT	0.190	↓	↓	↓	↓			72
23324	PEDOR	↓	↓	↓	↓	↓			73
23325	ASYM	↓	↓	↓	↓	↓			74
23421	HEMIS	0.190	LARGE	↓	↓	↓			78
23412	BICON	0.135	↓	↓	↓	↓			75
23422	↓	0.190	↓	↓	↓	↓			76
23432	↓	0.250	↓	↓	↓	↓			77
23423	FLAT	0.190	↓	↓	↓	↓			79
23424	PEDOR	↓	↓	↓	↓	↓			80
23425	ASYM	↓	↓	↓	↓	↓			81

- NOTES:
1. Static force data obtained on all configurations.
 2. Asterisk (*) indicates group numbers where garden gage data obtained.
 3. Test Reynolds numbers were 2, 4, and 4×10^6 /ft for Mach numbers 3.01, 4.02, and 5.05, respectively, except for group 1 at Mach 5.05 which was 6.5×10^6 /ft.
 4. Angle-of-attack range was from -5 to 12 deg at 0 sideslip.

Table 3-3. Test summary data group numbers (continued).

CONFIG. NO.	NOSE SHAPE	BLUNT. RATIO	BOOM SIZE	DROGUE ANGLE, DEG.	DROGUE STATION	TRIP SIZE, IN.	MACH NUMBER		
							3.01	4.02	5.05
24211	HEMIS	0.135	FLAME	30	FWD	NONE		124	
24311	↓	↓	INTER	↓	↓	↓		126	
24312	BICON	↓	↓	↓	↓	0.040			82
24322	↓	0.190	↓	↓	↓	↓			83
24332	↓	0.250	↓	↓	↓	↓			84
24314	PEDOR	0.135	↓	↓	↓	↓			85
24411	HEMIS	↓	LARGE	↓	↓	NONE		125	
25211	HEMIS	↓	FLAME	35	↓	0.040	107,	120	36*
	↓	↓	↓	↓	↓	↓	108	121	106
25212	BICON	↓	↓	↓	↓	NONE		123	
25212	↓	↓	↓	↓	↓	0.040	109	122	37,
	↓	↓	↓	↓	↓	↓			38,42
25213	FLAT	↓	↓	↓	↓	↓	110		39,40
25214	PEDOR	↓	↓	↓	MID	↓			41
33311	HEMIS	0.135	INTER	25	↓	↓	116		46
33321	↓	0.190	↓	↓	↓	↓			43
33312	BICON	0.135	↓	↓	↓	↓	115	119	44
33322	↓	0.190	↓	↓	↓	↓			45
33332	↓	0.250	↓	↓	↓	↓	117	118	47
33323	FLAT	0.190	↓	↓	↓	↓			48
33324	PEDOR	↓	↓	↓	↓	↓			49
33325	ASYM	↓	↓	↓	↓	↓			54
33421	HEMIS	↓	LARGE	↓	↓	↓			50,51
33412	BICON	0.135	↓	↓	↓	↓			52
33422	↓	0.190	↓	↓	↓	↓			53
33432	↓	0.250	↓	↓	↓	↓			55
33423	FLAT	0.190	↓	↓	↓	↓			56
33424	PEDOR	↓	↓	↓	↓	↓			57
33425	ASYM	↓	↓	↓	↓	↓			103
42421	HEMIS	0.190	↓	20	AFT	↓			1*,2*
42412	BICON	0.135	↓	↓	↓	0.025			3*
42422	↓	0.190	↓	↓	↓	↓			4*
42432	↓	0.250	↓	↓	↓	↓			5*
42413	FLAT	0.135	↓	↓	↓	↓			6*
42413	↓	↓	↓	↓	↓	0.040			7*
42423	↓	0.190	↓	↓	↓	↓			8*
42433	↓	0.250	↓	↓	↓	↓			104
42424	PEDOR	0.190	↓	↓	↓	↓			105
42425	ASYM	↓	↓	↓	↓	↓			

- NOTES:
1. Static force data obtained on all configurations.
 2. Asterisk (*) indicates group numbers where garden gage data obtained.
 3. Test Reynolds numbers were 2, 4, and $4 \times 10^6/\text{ft}$ for Mach numbers 3.01, 4.02, and 5.05, respectively, except for group 1 at Mach 5.05 which was $6.5 \times 10^6/\text{ft}$.
 4. Angle-of-attack range was from -5 to 12 deg at 0 sideslip.

Table 3-3. Test summary data group numbers (continued).

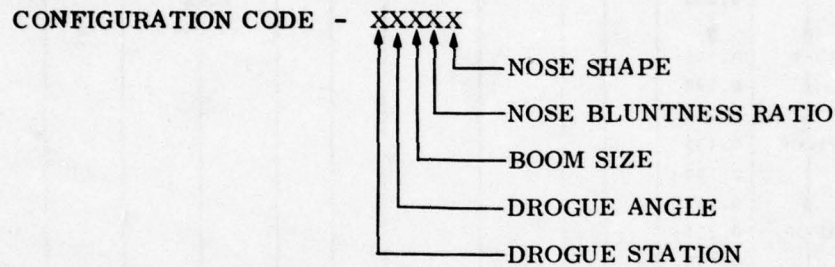
CONFIG. NO.	NOSE SHAPE	BLUNT. RATIO	BOOM SIZE	DROGUE ANGLE, DEG.	DROGUE STATION	TRIP SIZE, IN.	MACH NUMBER		
							3.01	4.02	5.05
43312	BICON	0.135	INTER	25	AFT	0.040			86
43322	↓	0.190	↓	↓	↓	↓			87
43332	↓	0.250	↓	↓	↓	↓			88
43411	HEMIS	0.135	LARGE	↓	↓	↓	114		9*, 10
43421	↓	0.190	↓	↓	↓	↓			11*
43431	↓	0.250	↓	↓	↓	↓			12*
43412	BICON	0.135	↓	↓	↓	↓	111		13*
43422	↓	0.190	↓	↓	↓	↓	112		14*
43432	↓	0.250	↓	↓	↓	NONE			16*
43432	↓	↓	↓	↓	↓	0.040	113		15*
43413	FLAT	0.135	↓	↓	↓	↓			17*
43423	↓	0.190	↓	↓	↓	↓			18*
43433	↓	0.250	↓	↓	↓	↓			19*
43414	PEDOR	0.135	↓	↓	↓	↓			20*
43424	↓	0.190	↓	↓	↓	↓			21*
43434	↓	0.250	↓	↓	↓	↓			22*
43415	ASYM	0.135	↓	↓	↓	↓			23*
43425	↓	0.190	↓	↓	↓	↓			24*
43435	↓	0.250	↓	↓	↓	↓			25*
43435	ASYM (90)	↓	↓	↓	↓	↓			26*
44411	HEMIS	0.135	↓	30	↓	↓			30*, 31
44412	BICON	↓	↓	↓	↓	↓			27*
44422	↓	0.190	↓	↓	↓	↓			28*, 29
44413	FLAT	0.135	↓	↓	↓	↓			32, 33
44414	PEDOR	↓	↓	↓	↓	↓			34, 35
46313	FLAT	0.135	INTER	30 BLB	↓	NONE	129		
46313	↓	↓	↓	↓	↓	0.040	128		101
46333	↓	0.250	↓	↓	↓	↓	127		102
46412	BICON	0.135	LARGE	↓	↓	↓			97
46422	↓	0.190	↓	↓	↓	↓			98
46432	↓	0.250	↓	↓	↓	↓			99
46433	FLAT	↓	↓	↓	↓	↓			100

NOTES:

1. Static force data obtained on all configurations.
2. Asterisk (*) indicates group numbers where garden gage data obtained.
3. Test Reynolds numbers were 2, 4, and $4 \times 10^6/\text{ft}$ for Mach numbers 3.01, 4.02, and 5.05, respectively, except for group 1 at Mach 5.05 which was $6.5 \times 10^6/\text{ft}$.
4. Angle-of-attack range was from -5 to 12 deg at 0 sideslip.

Table 3-4. Model component designation.

Each model configuration is identified by a 5-digit configuration numbers. Except for the baseline cone, the model configurations are comprised of nose, boom and drogue section components. The configuration number identifies the specific nose shape, nose bluntness ratio, boom size, drogue angle, and drogue location of each configuration. Model components are designated as follows:



Drogue Station

- 1 = Clean Body
- 2 = Forward (Sta. 55.541)
- 3 = Mid (Sta. 61.600)
- 4 = Aft (Sta. 68.200)

Boom Size

- 1 = Clean Body
- 2 = FLAME
- 3 = Intermediate
- 4 = Large

Drogue Angle

- 1 = Clean Body
- 2 = 20°
- 3 = 25°
- 4 = 30°
- 5 = 35°
- 6 = 30° BLB (with bleed overlay)

Nose Bluntness Ratio

- 1 = 0.135
- 2 = 0.190
- 3 = 0.250

Nose Shape

- 1 = Hemisphere
- 2 = Biconic
- 3 = Flat
- 4 = Pedoric
- 5 = Asymmetric

airstream. After the data acquisition sequence is completed, the model is returned into the tank and the fairing and safety doors are closed sealing the tank from the tunnel. The tank is vented to atmosphere with the tunnel running to allow access to the model in preparation for the next run. The sequence is repeated for each configuration and test condition.

3.3.2.2 Data Acquisition

To increase the data acquisition rate, the test was performed in a combined pitch-pause and continuous sweep mode and the force and heat-transfer rate data were recorded simultaneously during the data acquisition sequence. The first point of each data sequence was obtained in the pitch-pause mode to provide stabilized base pressure and Gardon gage measurements at zero angle-of-attack. Then the model was pitched to -5 degrees and the data sequence resumed as the model was pitched to 12 degrees in the continuous sweep mode at a sweep rate of approximately 0.45 deg/sec. Data were sampled at a rate of 2,400 channels/sec and 20 data loops were averaged for each data point. A differential base pressure measurement obtained during the sweep mode was combined with the initial base pressure measurement to provide base pressure variation with model angle-of-attack.

When Gardon gage data were desired, the model was cooled just prior to injection into the tunnel to a temperature near 45°F to provide as much temperature differential as possible between the model surface and the tunnel airstream. The cooling cycle required about five minutes to obtain the desired temperature level after the model had been in the tunnel. Table 3-1 shows the configurations on which Gardon gage measurements were obtained.

3.3.3 Data Reduction

Model force and moment measurements were reduced to coefficient form using the values calculated from the averaged data points and corrected for first and second order balance interaction effects. Model coefficients also were corrected for model tare weight and sting deflection. Model attitude, base pressure, and tunnel pressure and temperature also were calculated from averaged values.

The aerodynamic force and moment coefficients are presented in the standard body axis system. Pitching moments are referenced to a point on the model centerline at the virtual apex. Model base diameter and area were used as the reference length and area for the aerodynamic coefficients. Forebody axial-force coefficients (C_A) have been adjusted to zero base axial force using measured model pressures obtained and applied as described in Section 3.3.2. Lift (C_L) and drag (C_D) coefficients are based on normal-force coefficients (C_N) and forebody axial-force coefficients (C_A).

Heat-transfer rate data were reduced from the Gardon gage measurements using averaged data points obtained simultaneously with the force measurements. The thermopile-type Gardon gage is a direct reading heat-flux transducer whose output is converted to heating rate, \dot{q} , by means of an experimentally obtained scale factor, corrected for the gage edge temperature, T_e , and the gage output voltage. Gage surface temperature, T_w , is a function of T_e and the differential temperature, ΔT , between the center and edge of the gage sensing surface. Stanton number, St , calculations are related to tunnel free-stream conditions.

3.3.4 Data Uncertainty

An evaluation of the influence of random measurement errors is presented in this section to provide a partial measure of the uncertainty of the final test results presented in this report. Although evaluation of the systematic measurement error (bias) is not included, it should be noted that the instrumentation precision values (given in Section 3.2.3) used in this evaluation represent a total uncertainty combination of both systematic and 2-sigma random error contributions.

3.3.4.1 Test Conditions

Uncertainties in the basic tunnel parameters p_o and T_o (see Section 3.2.3) and the 2-sigma deviation in Mach number determined from test section flow calibrations were used to estimate uncertainties in the other free-stream properties, using the Taylor series method of error propagation.

M_∞	Uncertainty (\pm) Percent					
	M_∞	p_o	T_o	p_∞	q_∞	Re_∞
3.01	0.6	0.2	0.5	2.6	1.4	1.2
4.02	0.5	↓	↓	1.6	1.5	1.5
5.05	0.5	↓	↓	3.0	2.0	1.4

3.3.4.2 Aerodynamic Coefficients

The balance uncertainties listed in Section 3.2.3 were combined with uncertainties in the test conditions, using the Taylor series method of error propagation, to estimate the uncertainty of the aerodynamic coefficients for the primary test conditions.

M_∞	Uncertainty at Maximum Coefficient Value, ± Percent					
	C_N	C_m	C_Y	C_n	C_l	C_A
3.01	2.3	2.4	*	*	*	1.9
4.02	2.0	2.0	↓	↓	↓	1.8
5.05	2.6	2.6	↓	↓	↓	2.3

*Uncertainties for these coefficients were not evaluated as all configurations were run at zero beta and, except for one configuration, were symmetrical in the pitch plane.

The basic precision of the aerodynamic coefficients was also computed using only the balance uncertainties listed in Section 3.2.3 along with the nominal test conditions, using the assumption that the free-stream flow nonuniformity is a bias type of uncertainty which is constant for all runs. The following values, therefore, represent the data repeatability expected and are especially useful for detailed discrimination purposes in parametric model studies.

M_∞	Repeatability ±, Measured Coefficient Value					
	C_N	C_m	C_Y	C_n	C_l	C_A
3.01	0.0111	0.0024	0.0089	0.0009	0.0003	0.0036
4.02	0.0078	0.0017	0.0062	0.0006	0.0002	0.0025
5.05	0.0096	0.0020	0.0076	0.0008	0.0003	0.0031

The uncertainty in model attitude, α and β , as determined from tunnel sector calibrations and consideration of the possible errors in model deflection calculations, are estimated to be ± 0.1 degree.

Except for the basic gage calibration precision presented in Section 3.2.3, no evaluation was made of the uncertainties of the gage heat-rate and temperature measurements because of the quantitative purpose for which the measurements were made and the technique used to acquire the data. Gage data were obtained simultaneously with the force data to provide only general trends and levels and not for any quantitative evaluation.

3.4 RESULTS

3.4.1 Wind Tunnel Data

The anomaly in the FLAME vehicle drag was reproduced in the wind tunnel, and the cause was found to be flow separation in front of the drogue. When the model was injected into the

flow at zero angle-of-attack, the flow apparently separated, as shown in Figure 3-6a. However, when pitched to an angle-of-attack, the flow became attached as shown in Figure 3-6b. Shadowgraphs showing both types of flow are shown in Figure 3-7. Surprisingly, this phenomenon was found to be bi-stable in some instances. During some tests, the flow remained attached even after the model was pitched back to zero angle-of-attack. It was found that the difference in drag between separated and attached flow can exceed a factor of 2.0.

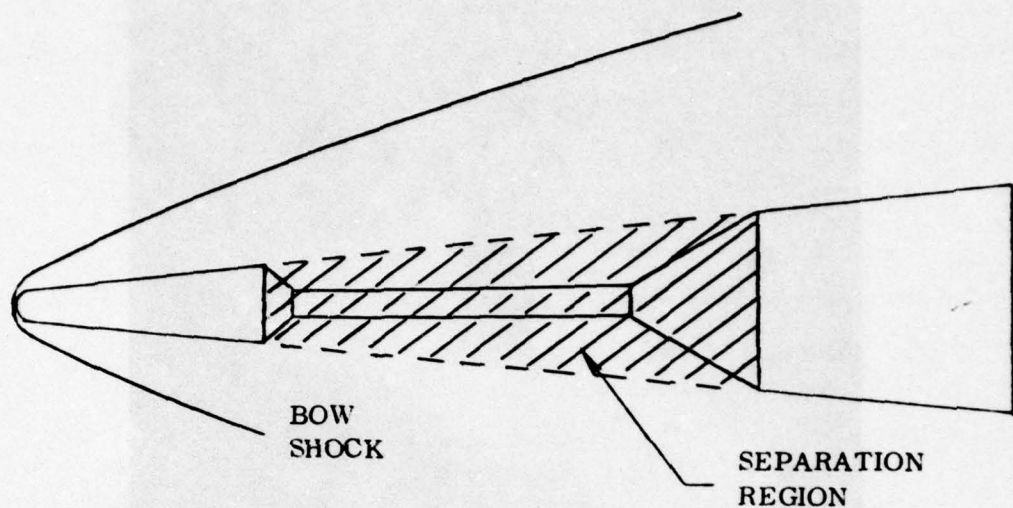
Heat transfer data showed that turbulent flow was achieved essentially over the whole body both with and without trips. The trips were found to have an insignificant effect on the aerodynamic data.

It had been hoped that the boundary layer bleed would suppress separation and allow higher drogue angles to be used. However, tests with boundary layer bleed on a 30 degree drogue indicated that the boundary layer bleed had essentially no effect.

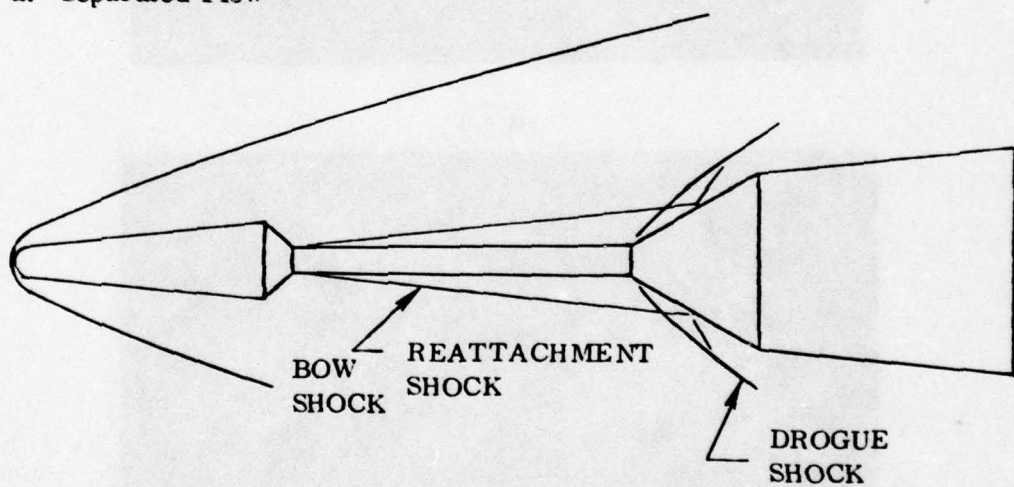
When separation in front of the drogue occurred, it was found to be a strong function of drogue angle as shown in Figure 3-8. Tests were conducted of wake-drogue configurations with different nose shapes for the 35 degree drogue angle, and with different bluntness ratios for the 25 degree drogue angle. As shown in Figures 3-9 through 3-11, the drag change caused by separation for the 35 degree drogue was significantly affected by the nosetip shape at Mach 5, and to a lesser extent at Mach 4 and 3. Note that since the drags of the different shape noses were not equal (see Figure 3-12), bluntness ratio might have caused a similar effect. Figure 3-13 shows that separation never occurred on the 25 degree drogue runs, regardless of the bluntness ratio. Unfortunately, the relatively low drag of the 25 degree drogue configuration makes it unattractive for the wake-drogue recovery vehicle design.

The flared body data was similar to the wake-drogue data: flow separation that was strongly affected by the nosetip occurred at high flare angles, but not at low flare angles. In this respect, the principal difference between a flared body and a wake-drogue is that due to the differences discussed in Section 2.0, practical flared body recovery vehicles can be designed using flare angles that do not induce separation.

Figure 3-14 shows the influence of flare angle on drag. The curves are very similar to those of the wake-drogue with two differences: 1) due to the difference in effective flare/drogue area, flared body drag is approximately 50 percent higher than the wake-drogue drag for the same drogue angle; and 2) separation on the flared body is never bi-stable.

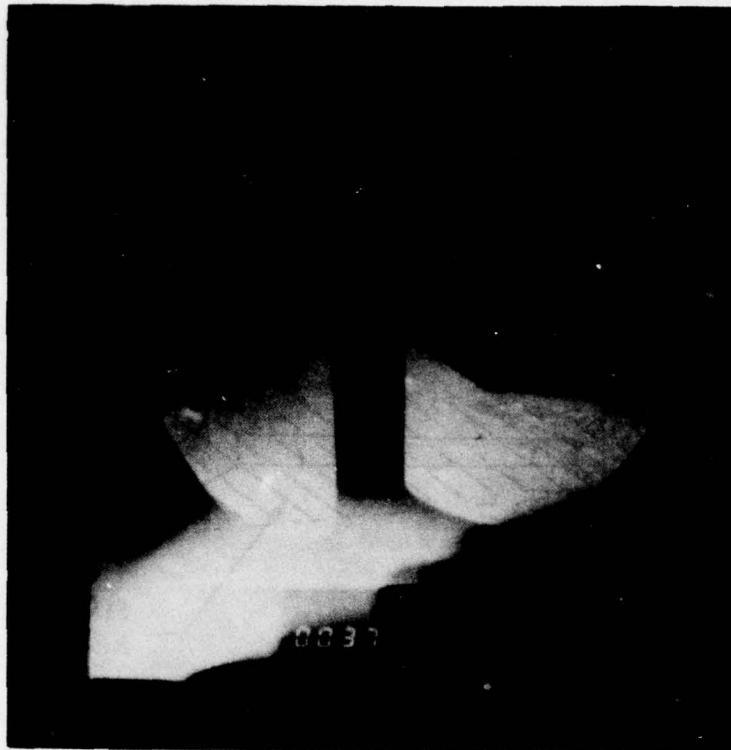


a. Separated Flow

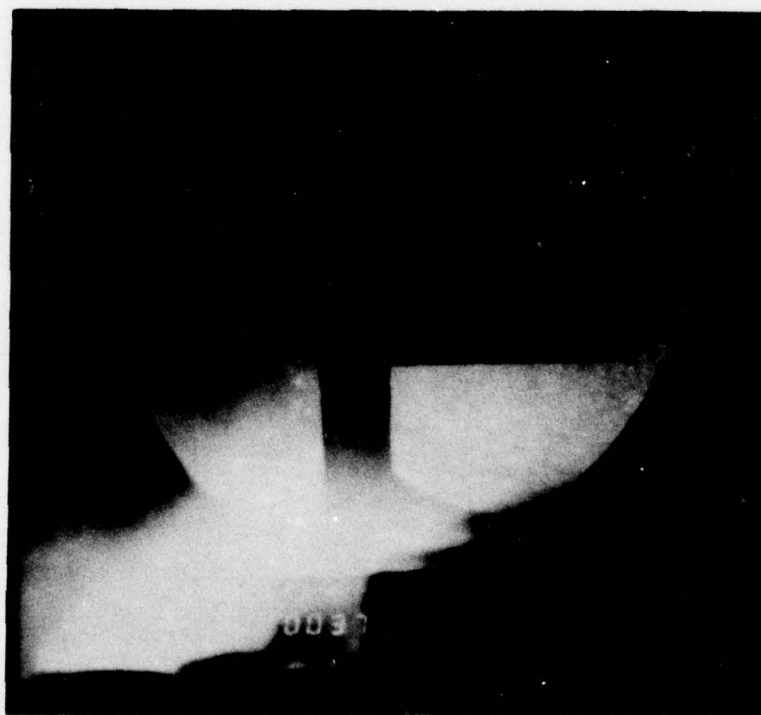


b. Attached Flow

Figure 3-6. FLAME flow fields.



$\alpha = 0^\circ$



$\alpha = 3^\circ$

Figure 3-7. FLAME configuration shadowgraphs.

MACH 5
 FLAME WITH INTERMEDIATE BOOM SIZE
 BICONIC NOSE
 0.135 BLUNTNESS

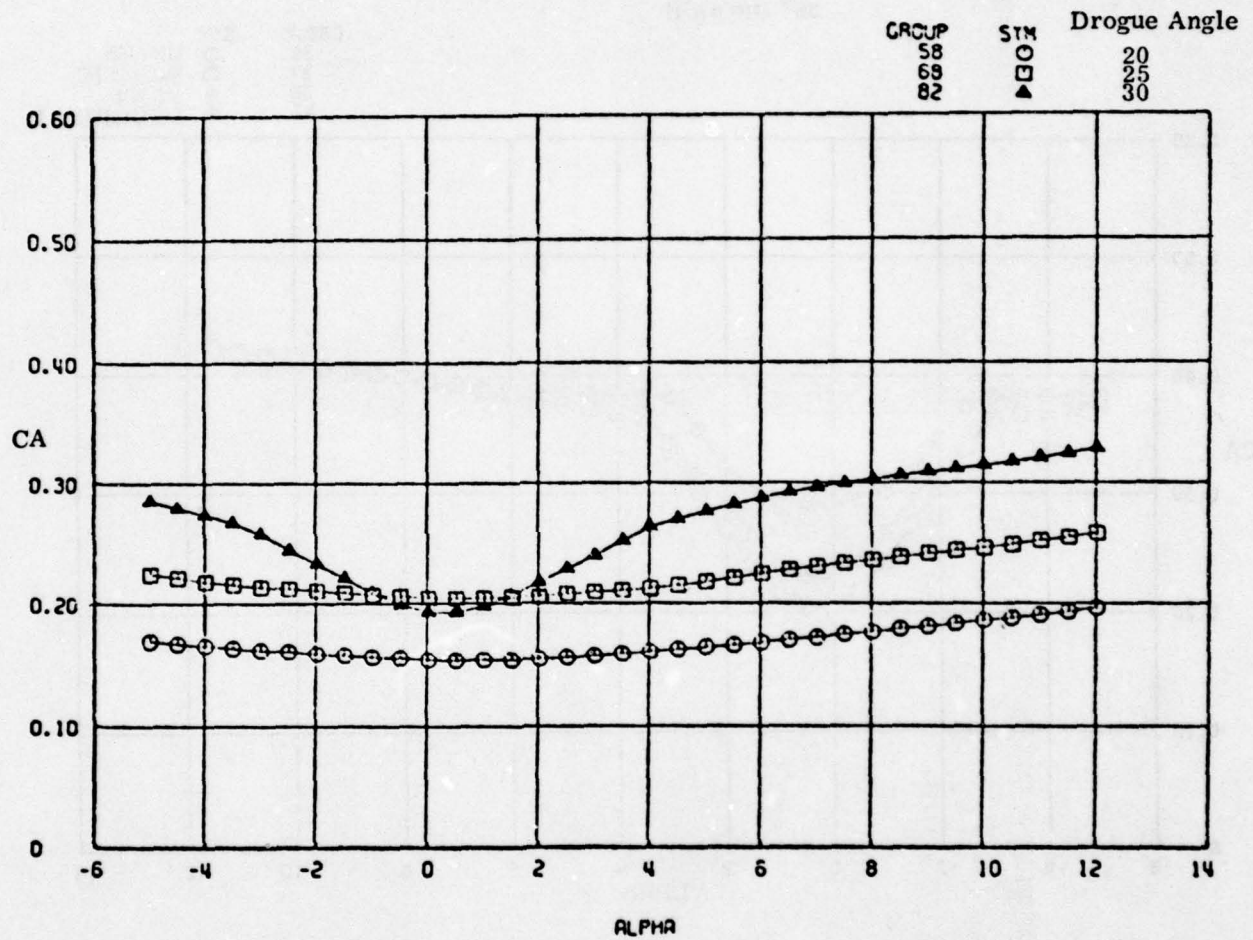


Figure 3-8. FLAME drogue angle sensitivity.

FLAME CONFIGURATION
0.135 BLUNTNESS
35° DROGUE

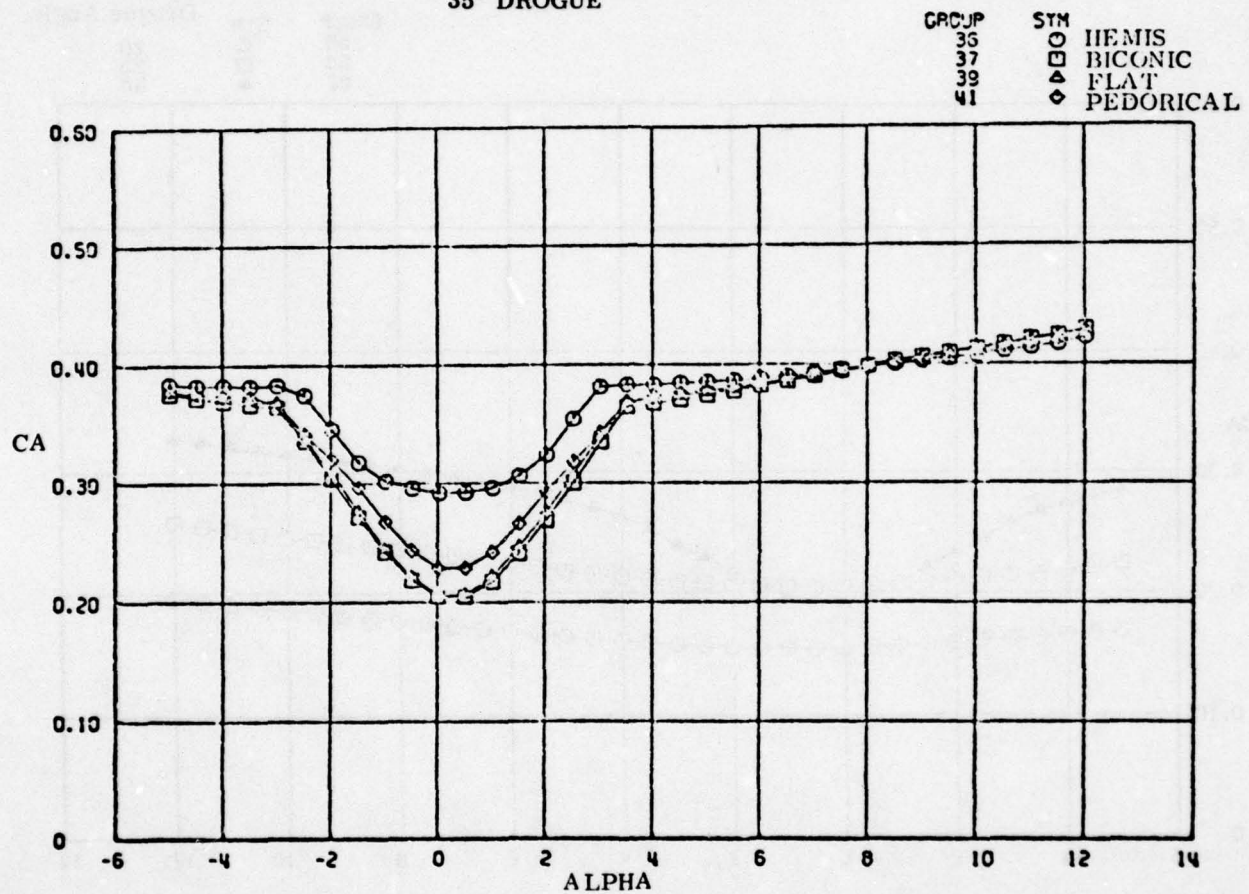


Figure 3-9. FLAME nose shape sensitivity (Mach 5).

FLAME CONFIGURATION
0.135 BLUNTNESS
35° DROGUE

GROUP SYM HEMIS
120 ○
122 □ BICONIC

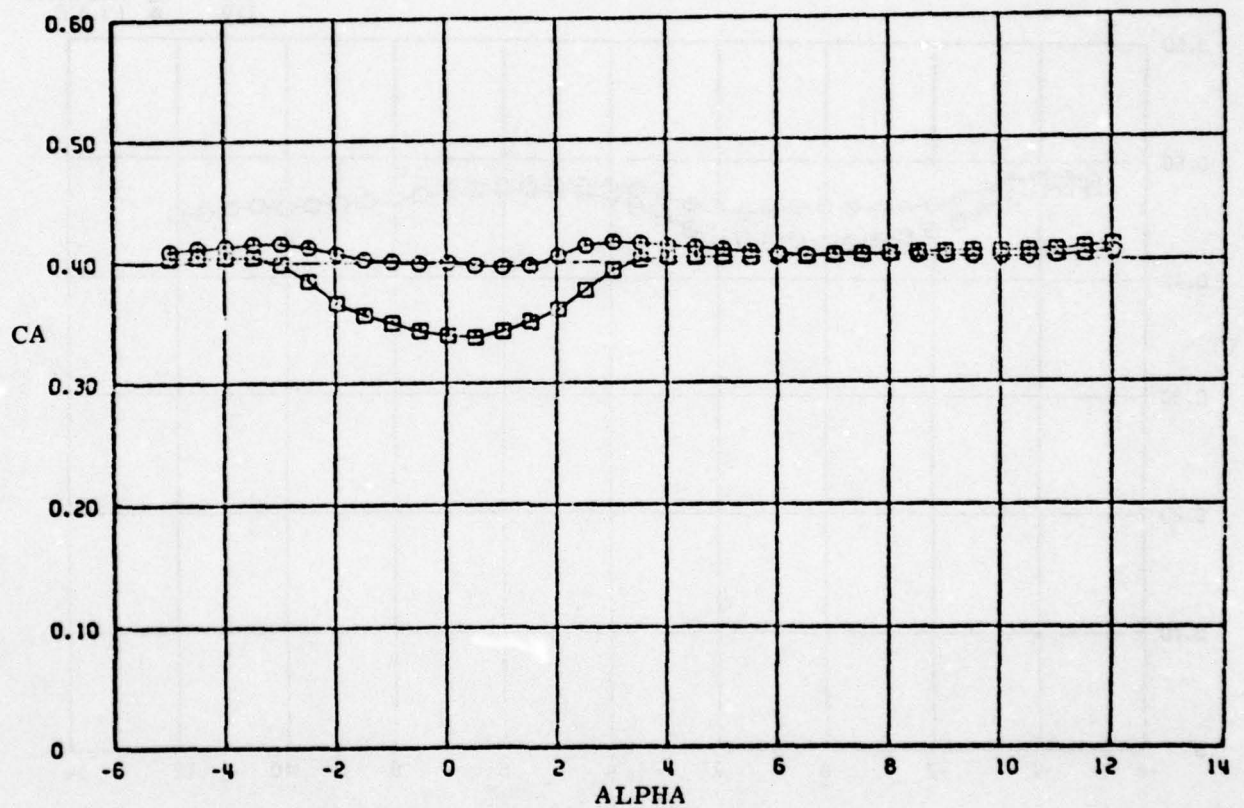


Figure 3-10. FLAME nose shape sensitivity (Mach 4).

FLAME CONFIGURATION
0.135 BLUNTNESS
35° DROGUE

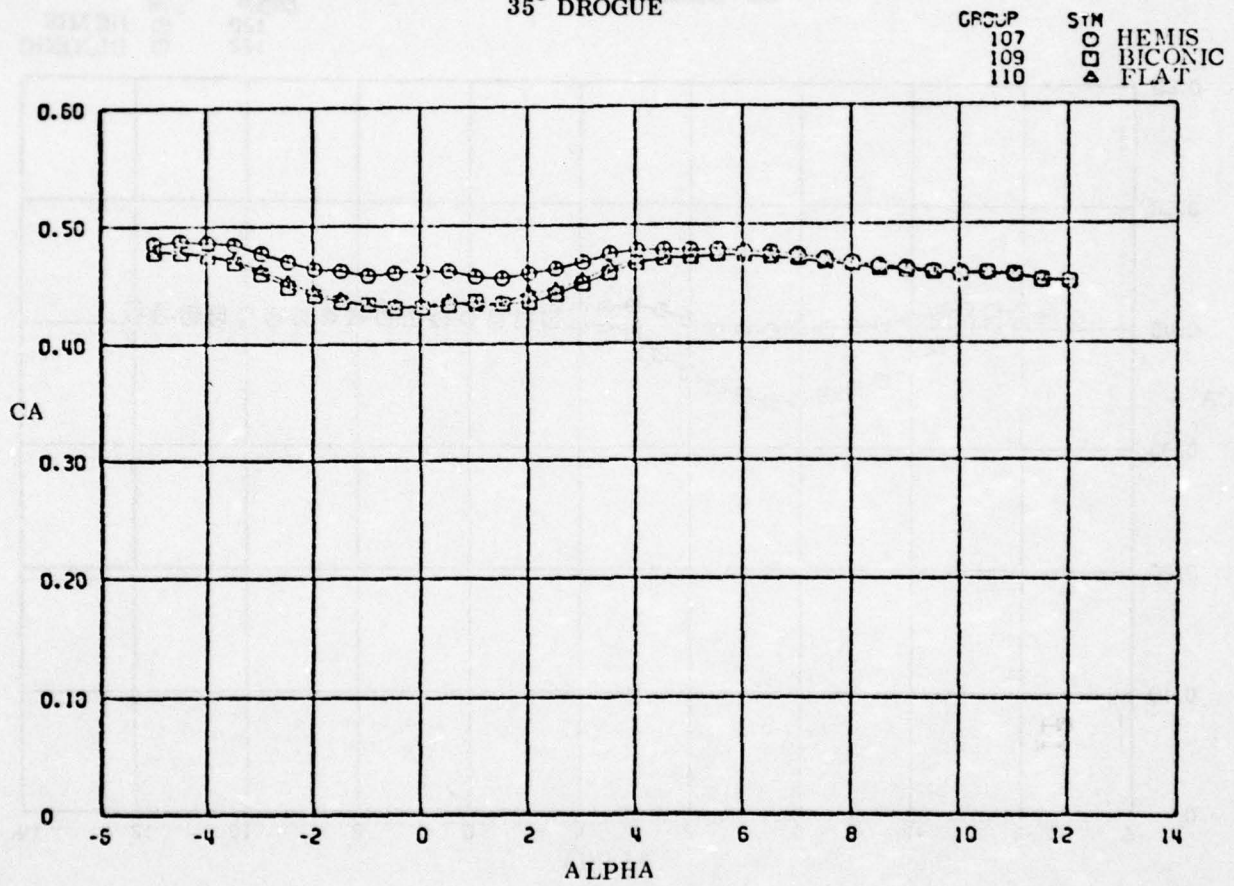


Figure 3-11. FLAME nose shape sensitivity (Mach 3).

$$R_N/R_B = 0.190$$

Mach 5

GROUP	SYM	
90	○	Hemis
96	□	Flat
95	△	Pedorical
93	◇	Asym.

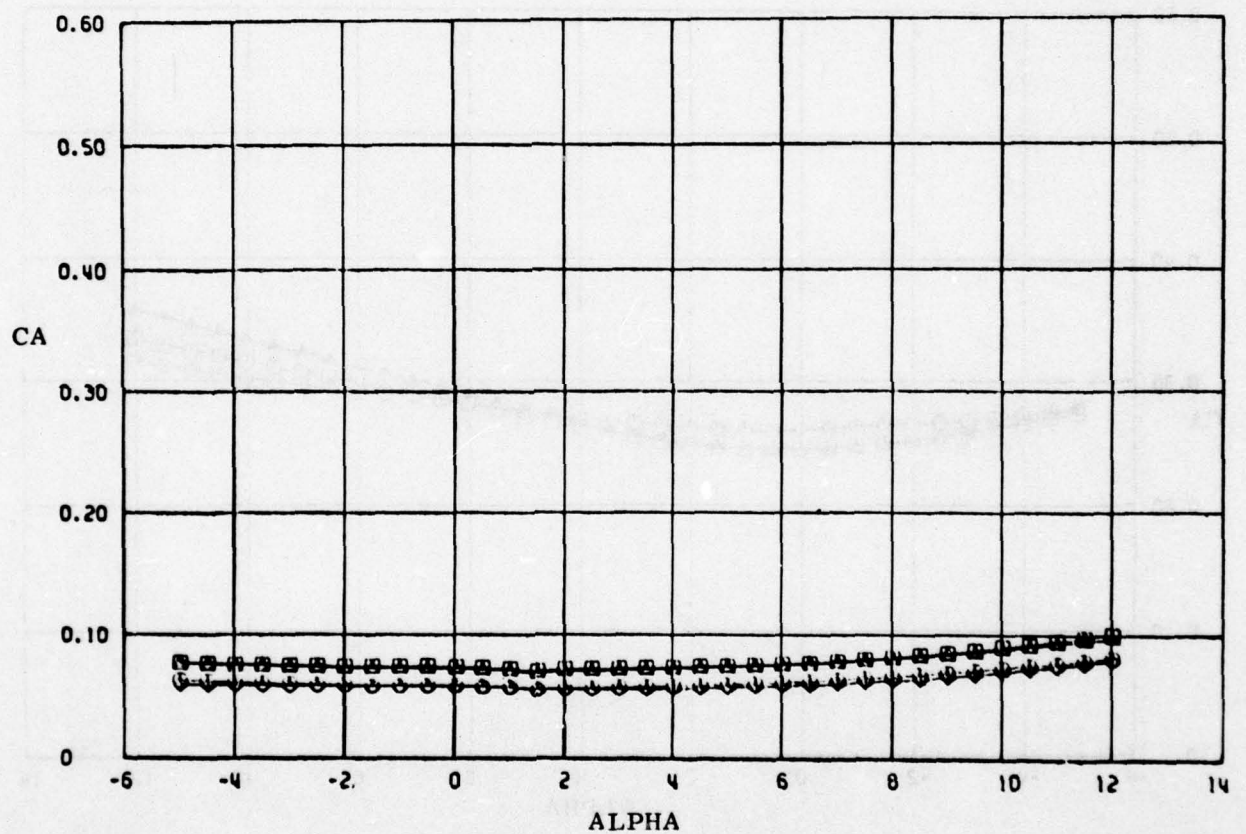


Figure 3-12. Pre-recovery nose shape sensitivity.

GROUP	SYM	R_N/R_B
43	○	0.135
44	□	0.190
45	△	0.250

MACH 5

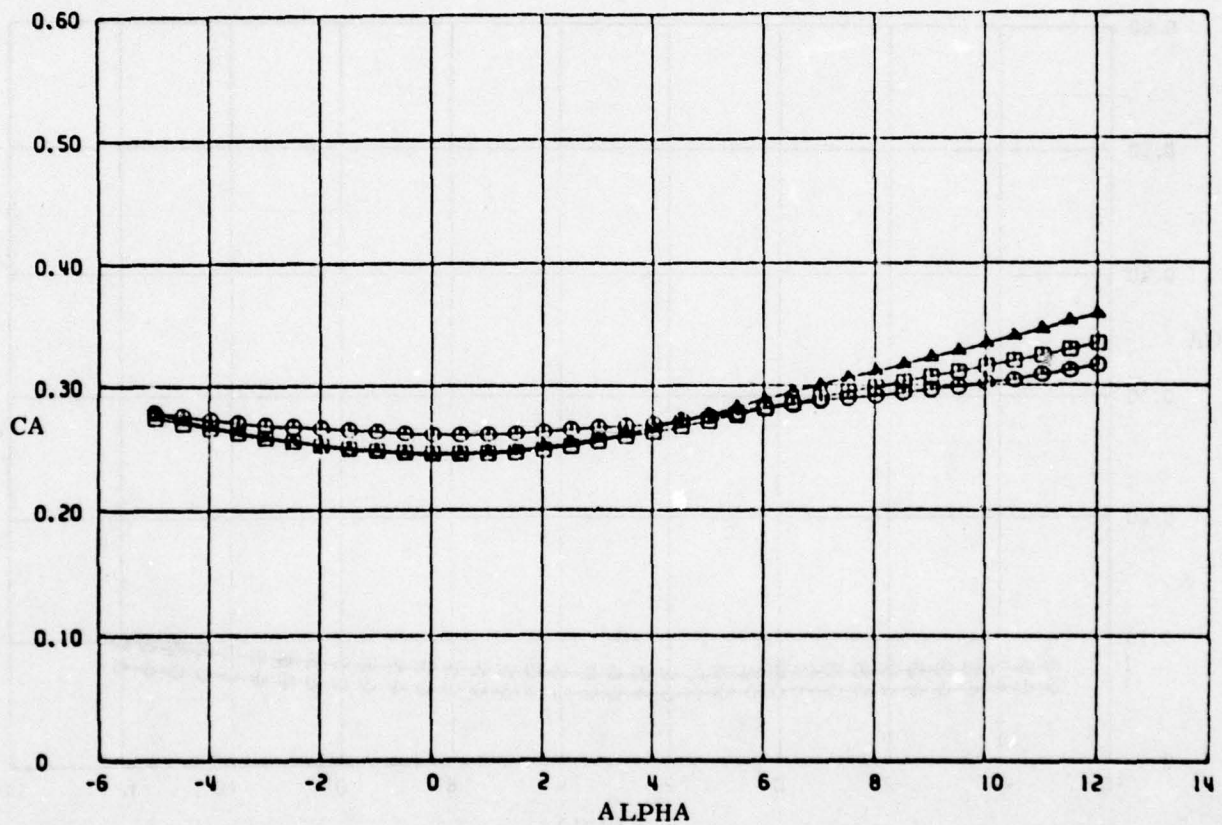


Figure 3-13. FLAME bluntness sensitivity (25° drogue).

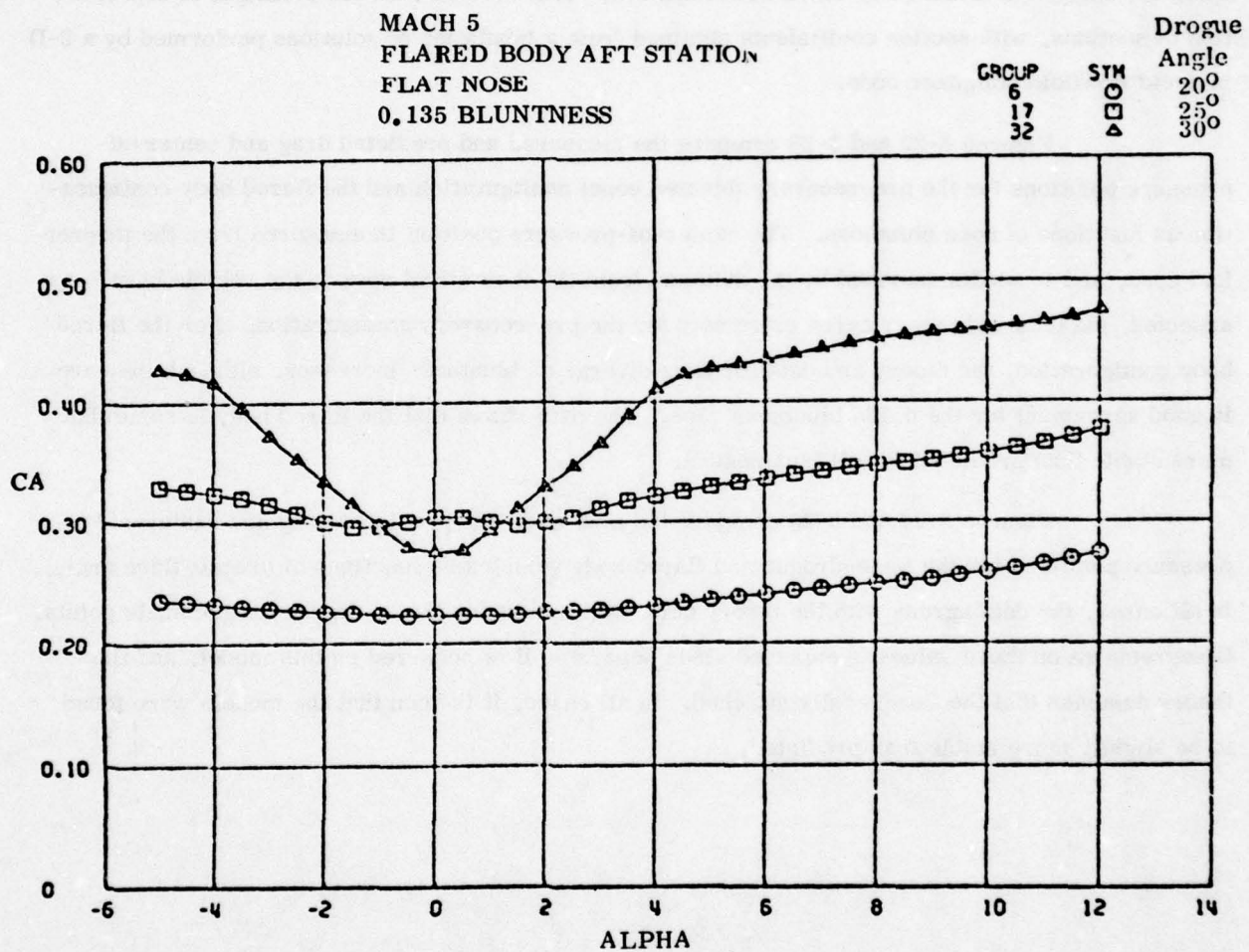


Figure 3-14. Flared body drogue angle sensitivity.

As with the wake-drogue, drag was strongly affected by nosetip shape if the flare angle was high enough to cause separation (Figure 3-15), and was essentially unaffected by both nosetip shape and bluntness ratio for lower flare angles (Figures 3-16 through 3-19).

3.4.2 Comparison to Theory

The data were generally found to agree well with the pretest predictions performed using the analytical method described in Section 2.2. This method uses the principal of superposition of sections, with section coefficients obtained from a tabulation of solutions performed by a 3-D inviscid flowfield computer code.

Figures 3-22 and 3-23 compare the measured and predicted drag and center-of-pressure positions for the pre-recovery (blunted cone) configuration and the flared body configuration as functions of nose bluntness. The center-of-pressure position is measured from the theoretical apex, and is nondimensioned by the distance from the theoretical apex to the vehicle base. As expected, the data and theory agree extremely for the pre-recovery configuration. For the flared body configuration, the theory and data for drag diverge as bluntness increases, although they are in good agreement for the 0.135 bluntness case. The data shows that the flared body is somewhat more stable than predicted for all bluntnesses.

Figures 3-24 and 3-25 compare the measured and predicted drag and center-of-pressure positions for the wake-drogue and flared body vehicles as functions of drogue/flare angle. In all cases, the data agrees with the theory quite well except for the 30 degree drogue angle points. Disagreement on these values is expected since separated flow occurred on this model, and the theory assumes that the flow is fully attached. In all cases, it is seen that the models were found to be slightly more stable than predicted.

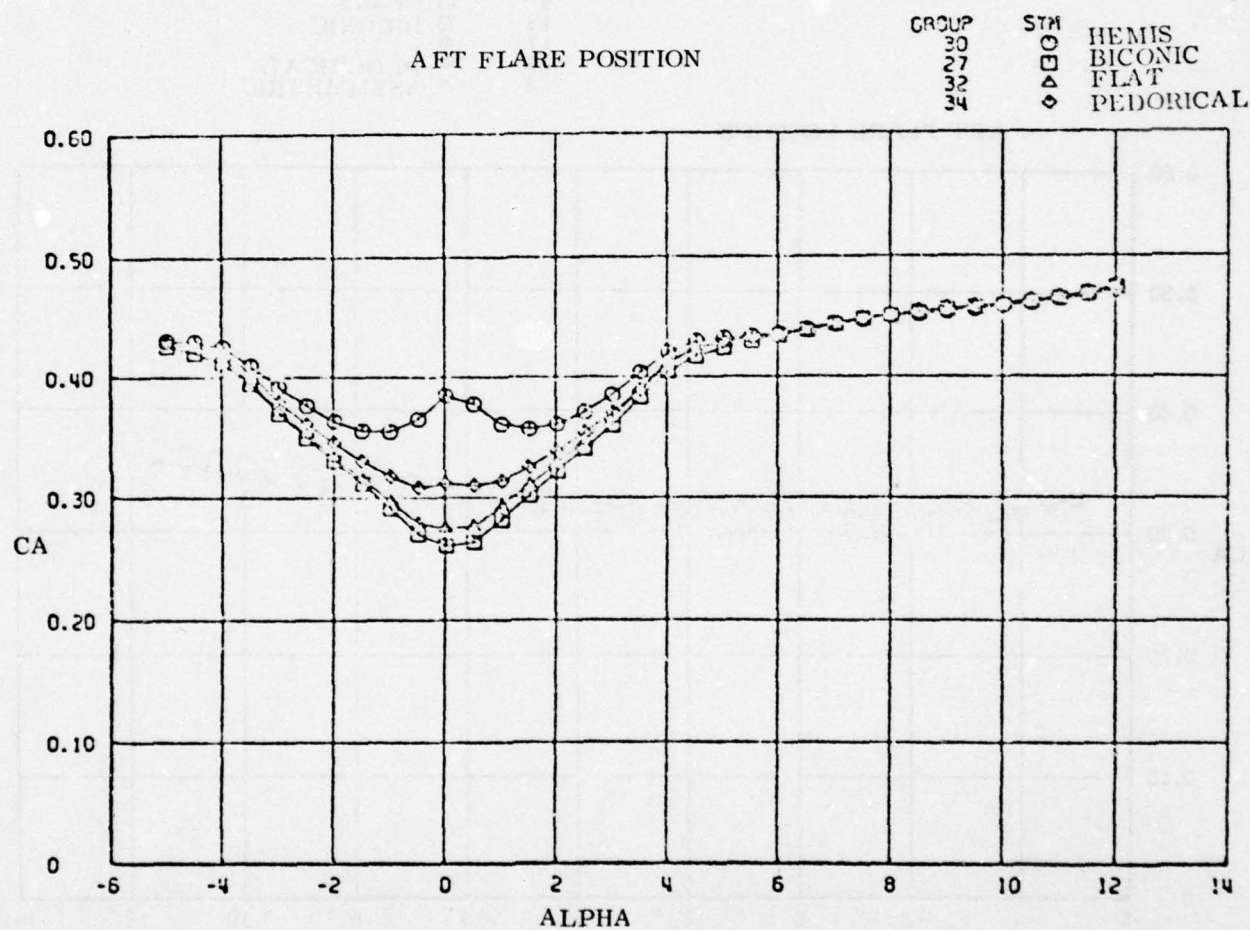


Figure 3-15. Flared body nose shape sensitivity
(30° flare, Mach 5, 0.135 Bluntness).

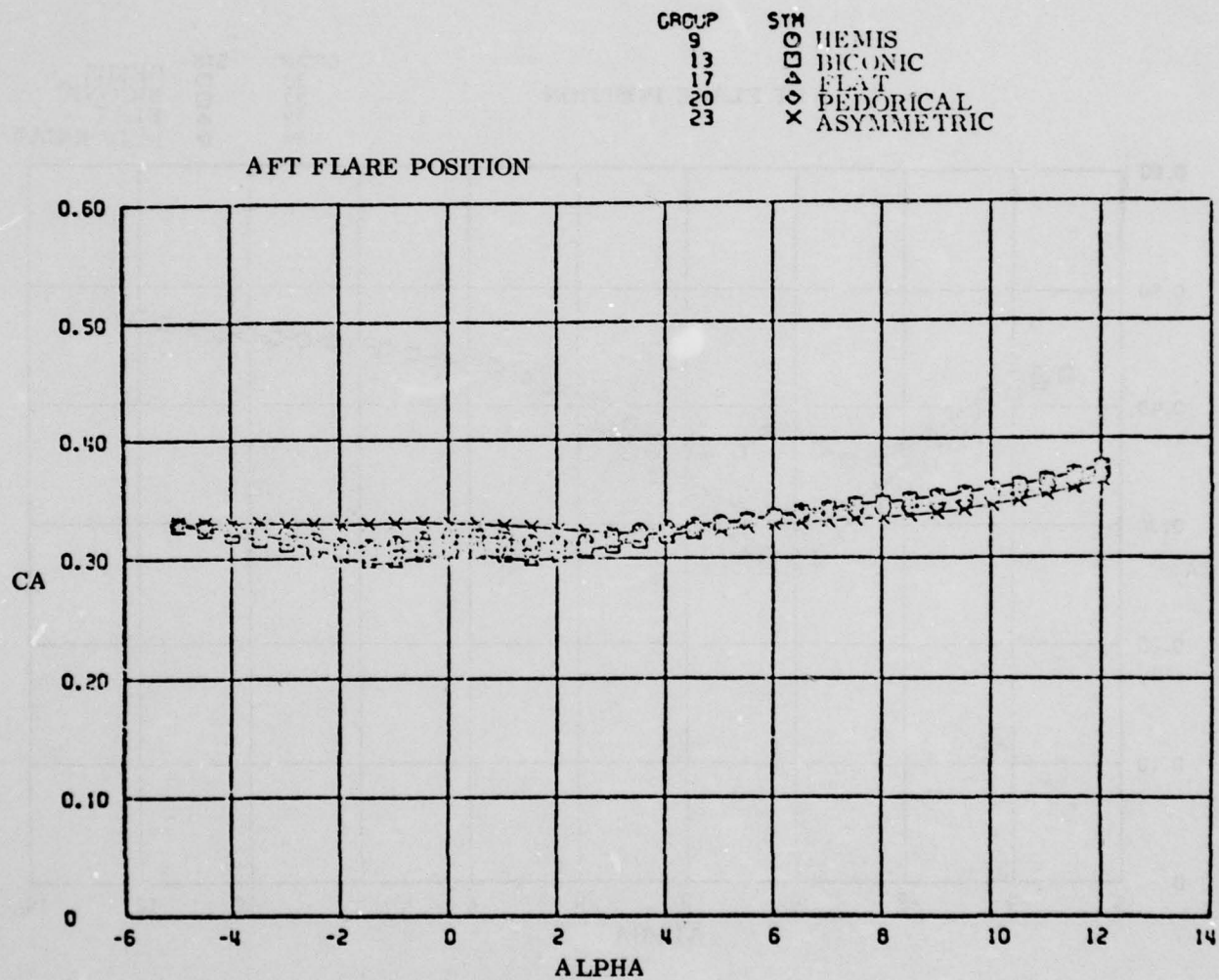


Figure 3-16. Flared body nose shape sensitivity
(25° flare, Mach 5, 0.135 bluntness).

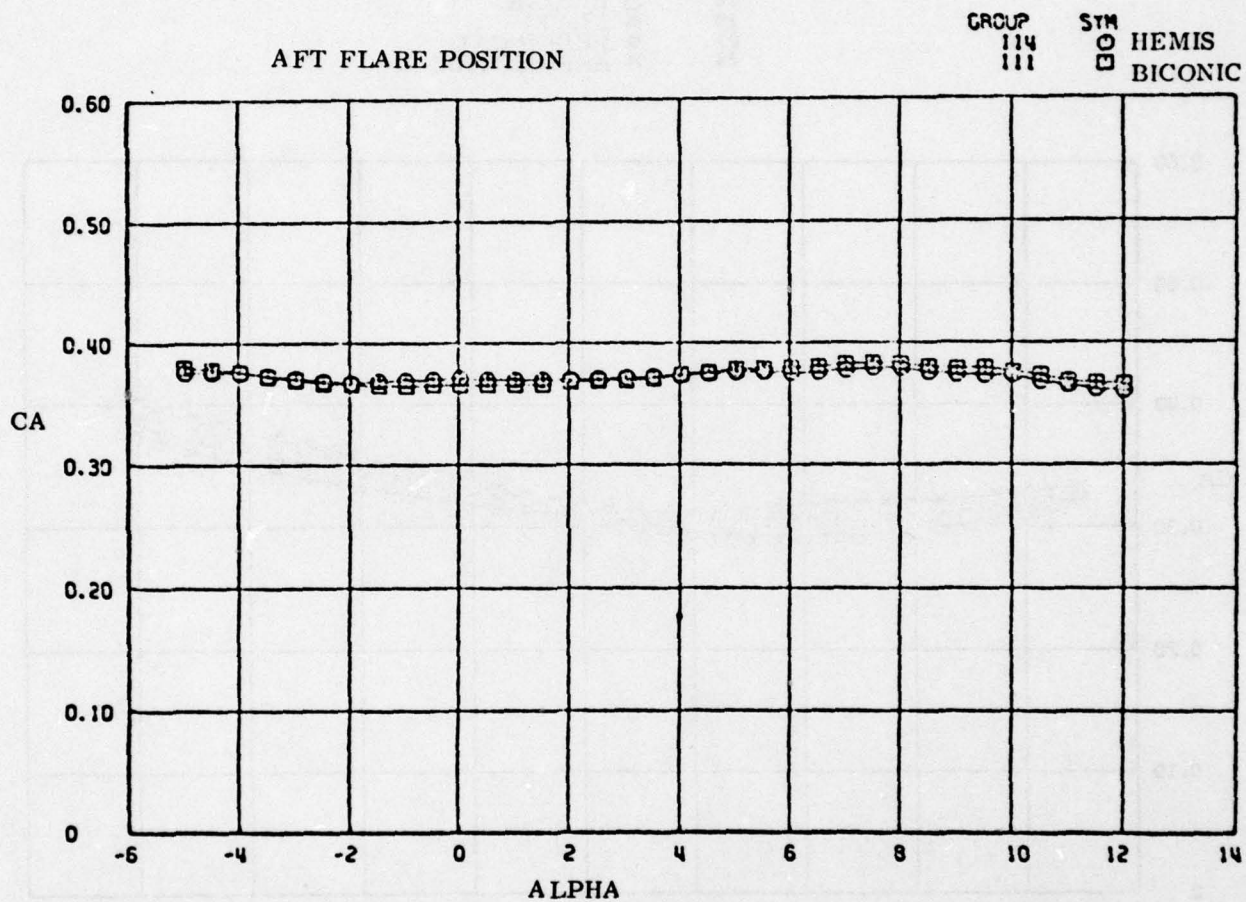


Figure 3-17. Flared body nose shape sensitivity
(25° flare, Mach 3, 0.135 bluntness).

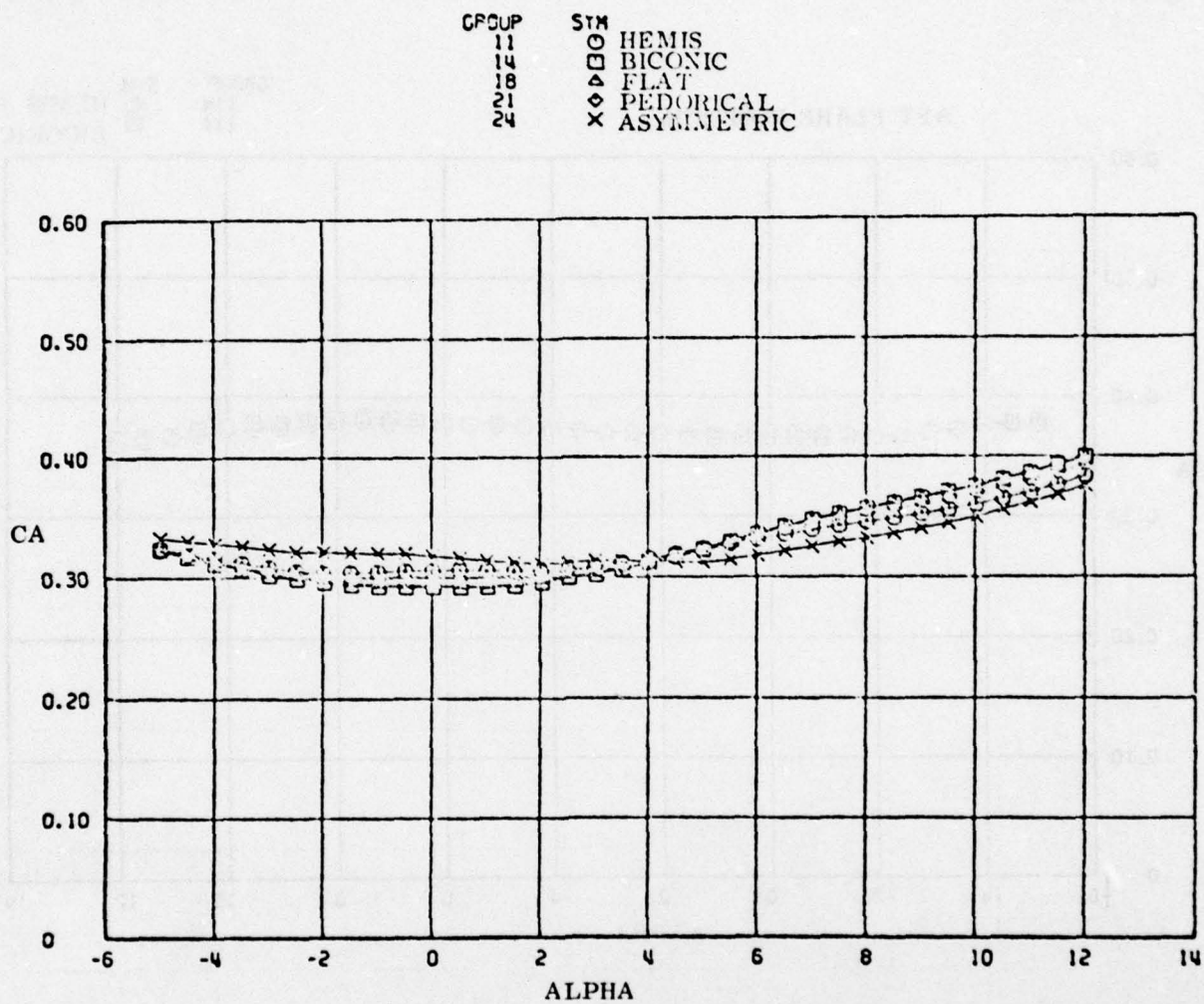


Figure 3-18. Flared body nose shape sensitivity
(25° flare, Mach 5, 0.190 bluntness).

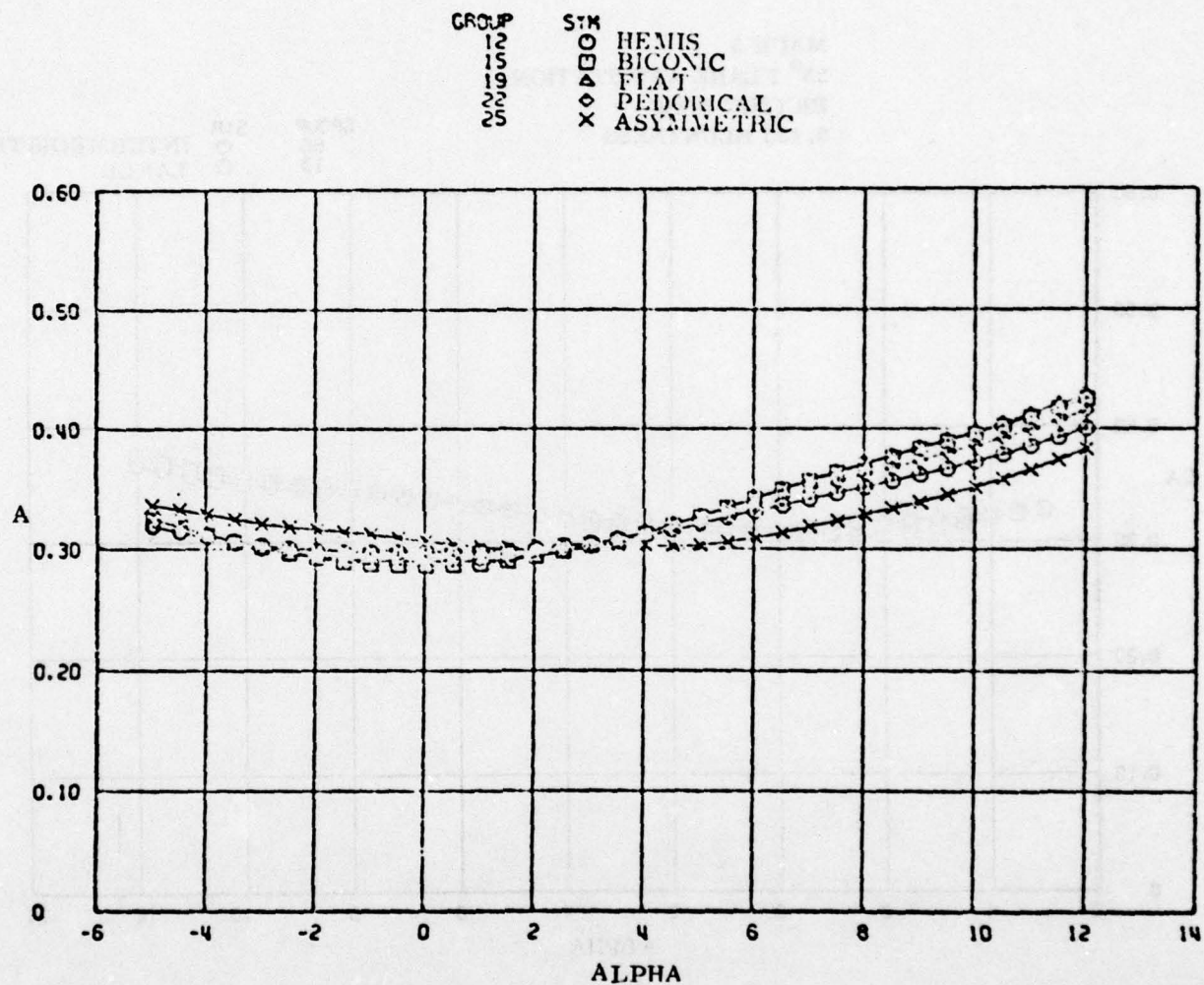


Figure 3-19. Flared body nose shape sensitivity
(25° flare, Mach 5, 0.250 bluntness).

MACH 5
 25° FLARE AFT STATION
 BICONIC NOSE
 0.135 BLUNTNESS

GROUP 86 13
 SYM O □
 INTERMEDIATE LARGE

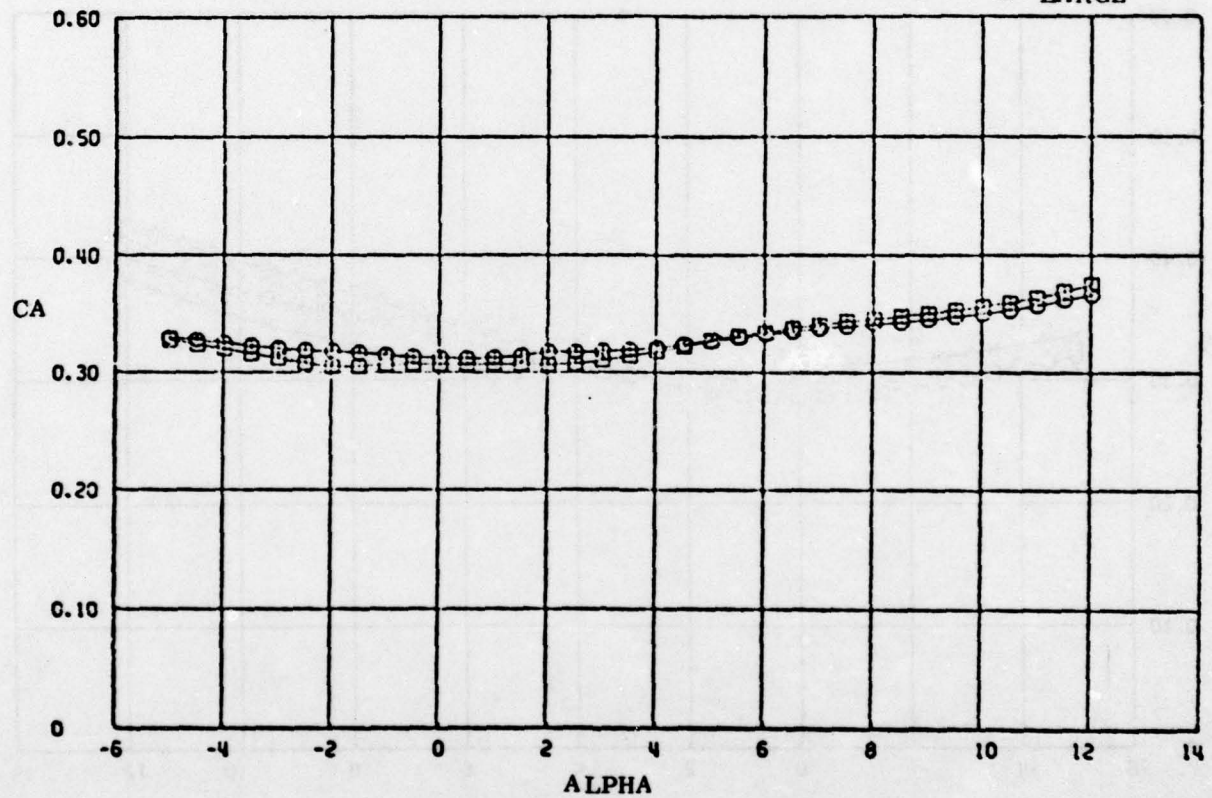


Figure 3-20. Boom size sensitivity.

MACH 5
 25° FLARE
 BICONIC NOSE
 0.135 BLUNTNESS

GROUP	SYM
68	○
43	□
86	△

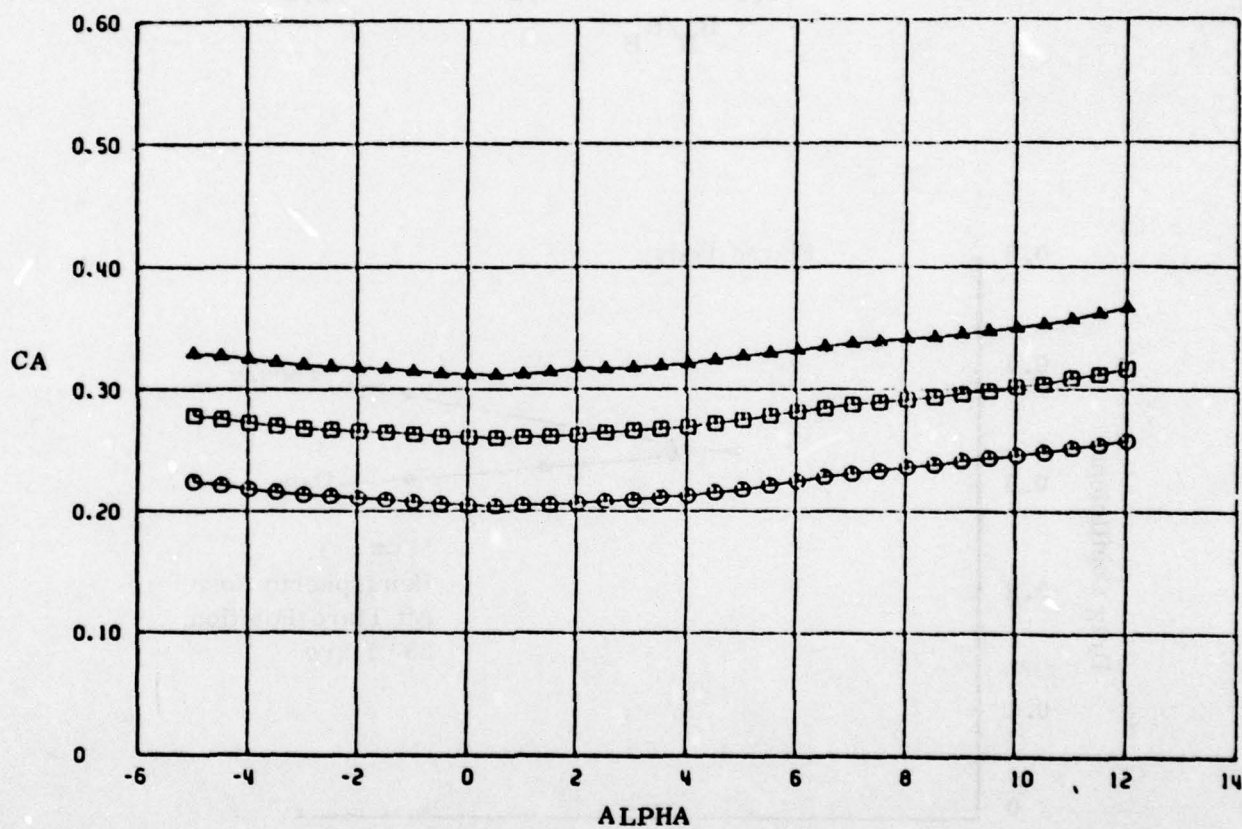


Figure 3-21. Flare position sensitivity.

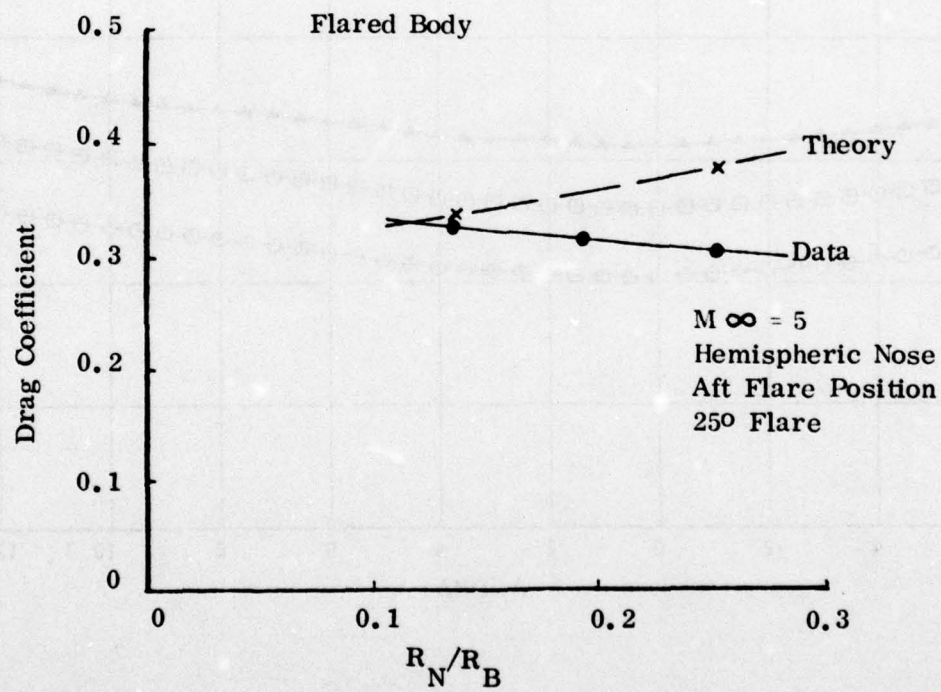
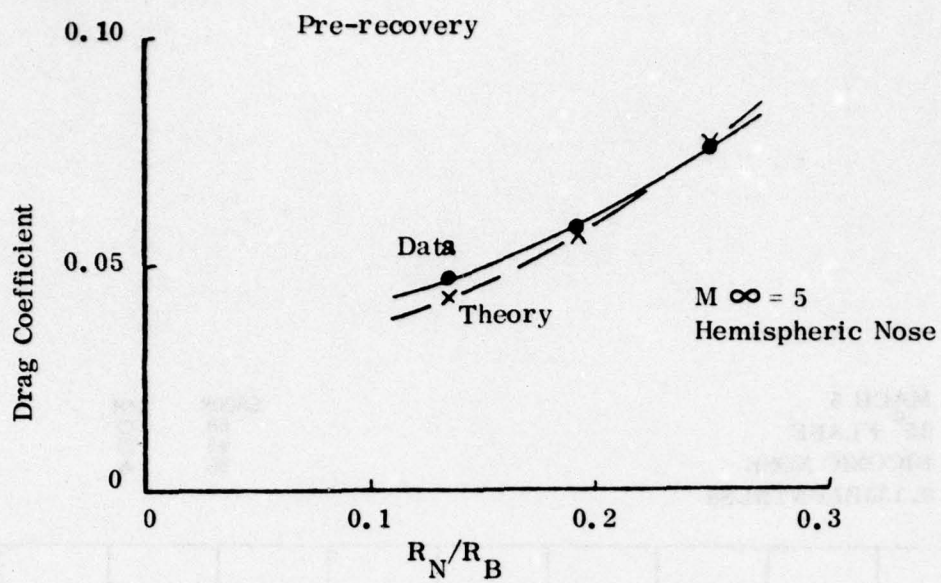


Figure 3-22. Influence of bluntness on drag.

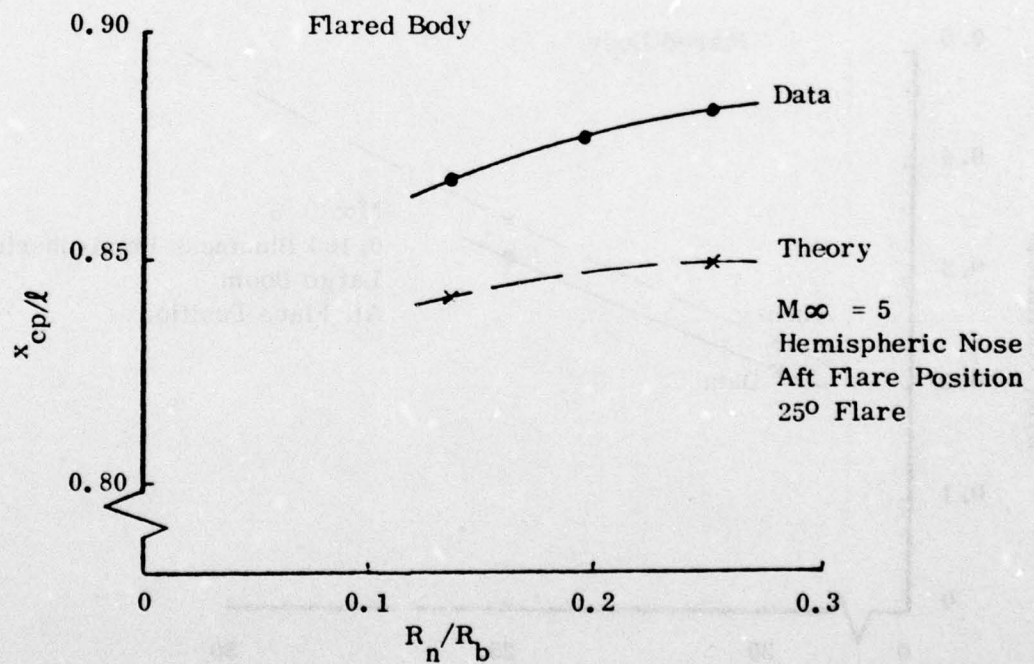
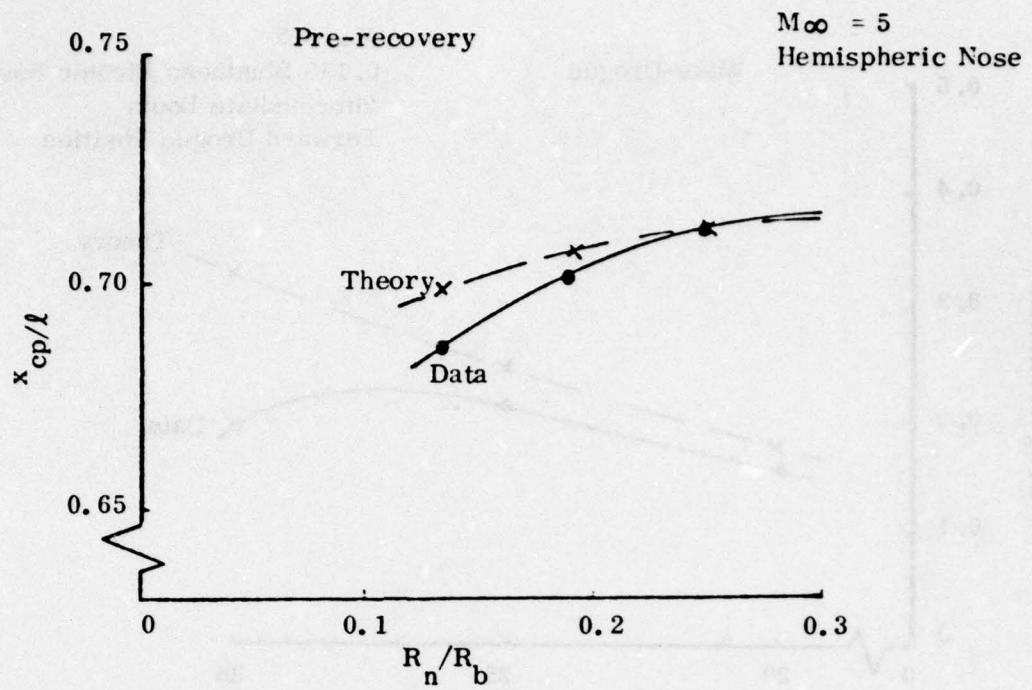


Figure 3-23. Influence of bluntness on center-of-pressure position.

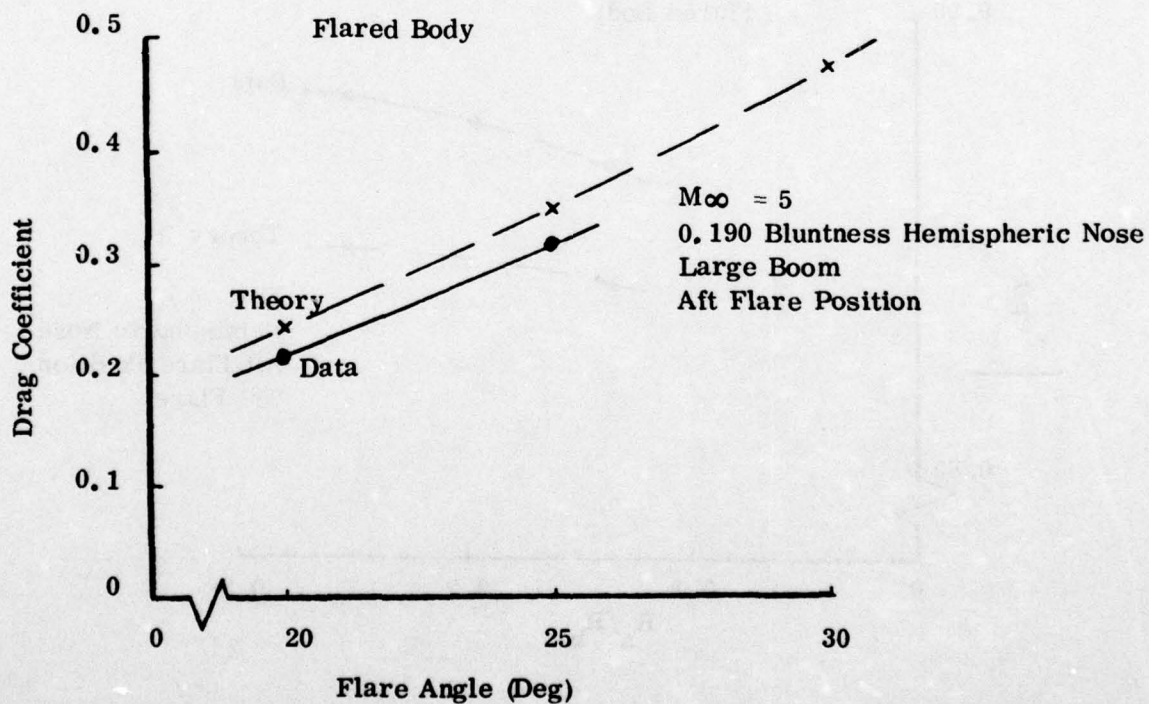
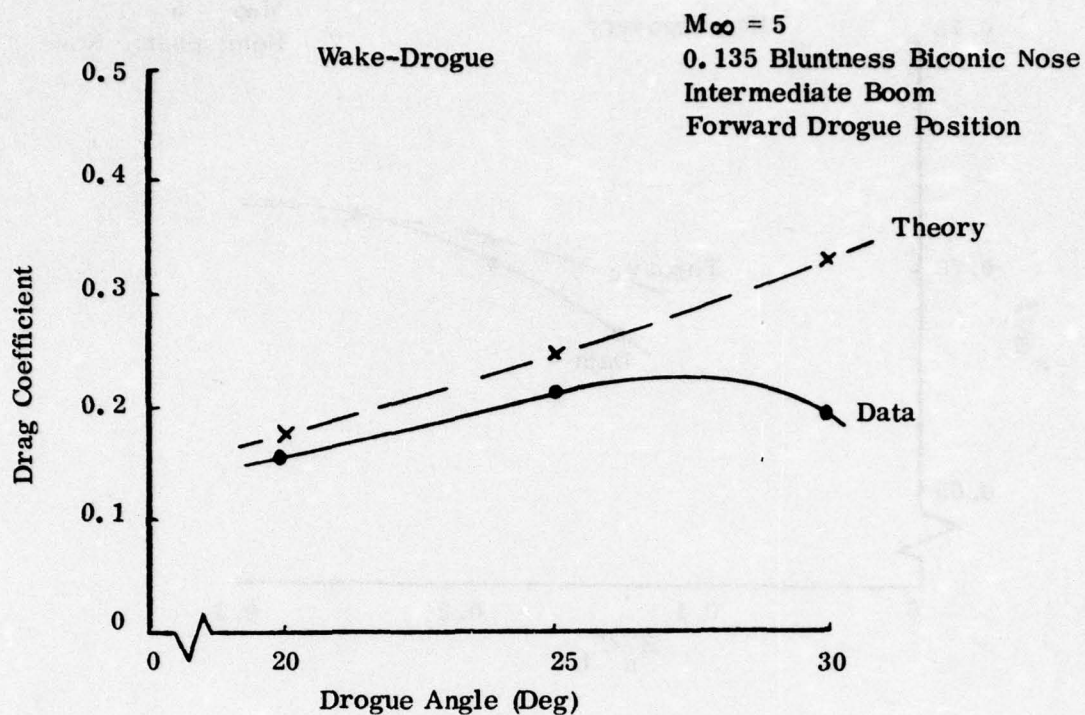


Figure 3-24. Influence of drogue/flare angle on drag.

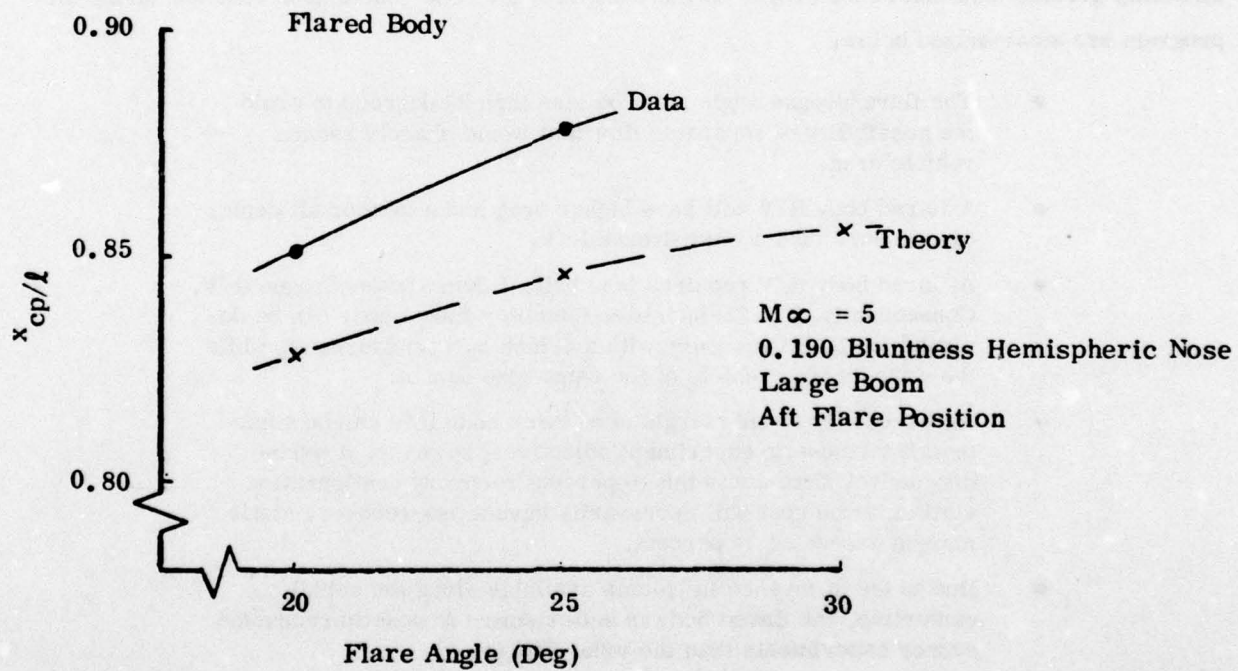
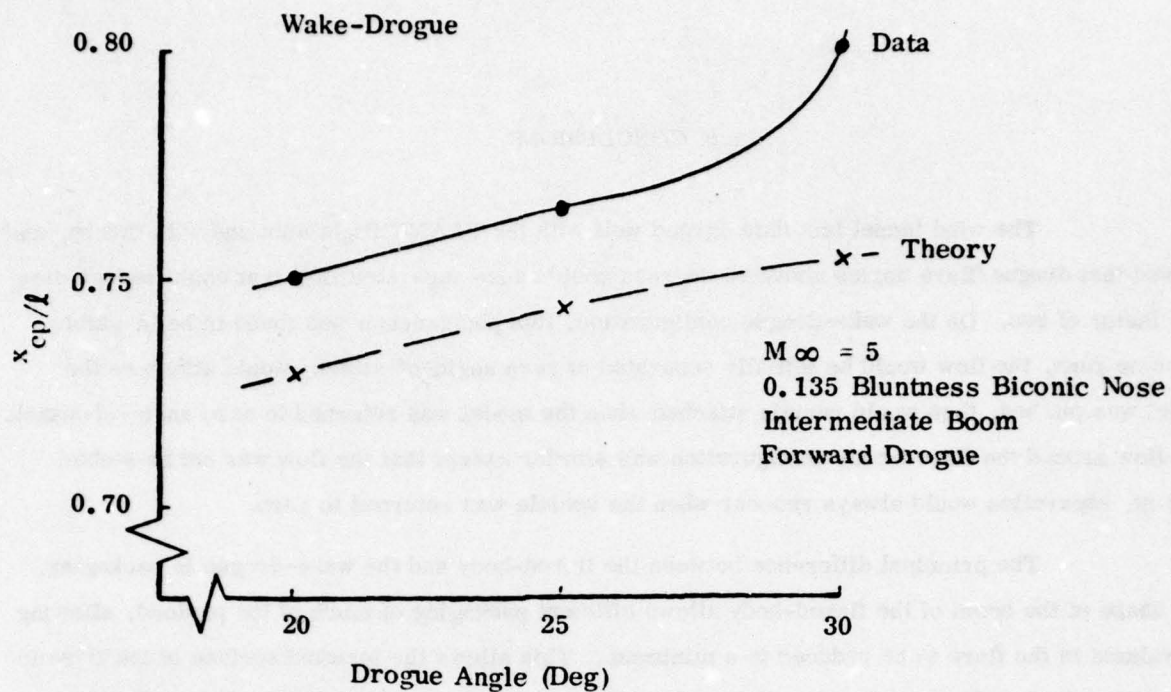


Figure 3-25. Influence of drogue/flare angle on center-of-pressure position.

4.0 CONCLUSIONS

The wind tunnel test data agreed well with the FLAME flight data and with theory, and showed that drogue/flare angles above 25 degrees could cause separated flow that could reduce drag by a factor of two. On the wake-drogue configuration, this phenomenon was found to be bi-stable. On some runs, the flow would be initially separated at zero angle-of-attack, would attach as the model was pitched, then would remain attached when the model was returned to zero angle-of-attack. The flow around the flared-body configuration was similar except that the flow was not bi-stable. That is, separation would always reoccur when the vehicle was returned to zero.

The principal difference between the flared-body and the wake-drogue is packaging. The shape of the boom of the flared-body allows efficient packaging of much of the payload, allowing the volume in the flare to be reduced to a minimum. This allows the forward surface of the flare to be positioned much farther aft than is possible on the wake-drogue in which all of the payload is packaged in the drogue. Consequently, the effective area of the flare on the flared-body can be significantly greater than that of the drogue on the wake-drogue. The conclusions reached during this program are summarized below:

- The flare/drogue angle must be less than 30 degrees to avoid the possibility of separated flow that would sharply reduce vehicle drag.
- A flared body R/V will have higher drag and a farther aft center-of-pressure than a wake drogue R/V.
- A flared body R/V requires less ballast than a wake-drogue R/V. Consequently, a 9.25-inch base diameter flared body can be designed for ICBM recovery with a 4-inch nosetip overhang, while the wake-drogue vehicle of the same size cannot.
- Pre-recovery static margin of a flared body R/V can be varied to suit the nosetip experiment objectives; however, a wake-drogue R/V that meets the 10 percent recovery configuration static margin goal will necessarily have a pre-recovery static margin exceeding 14 percent.
- Due to the difference in volume available along the vehicle centerline, the flared body is better suited to nosetip recession sensor experiments than the wake-drogue.
- The larger diameter boom of the flared body has over triple the angle-of-attack capability of the wake-drogue.
- Flared body R/V's with a 25° flare angle can recover nosetips on R/V's with ballistic coefficients up to 3500 reaching stagnation pressures of 160 atm, with recovery initiated below 15,000 foot altitude.

- For a 60 percent mass ejection, the following ballistic coefficient (β) change on recovery can be achieved.

R_N/R_B	β DRAG	β WEIGHT	β TOTAL
.135	6.5	2.5	16.3
.250	3.6	2.5	9.0

5.0 REFERENCES

1. Kochendorfer, P. C., "HEART Recovery Vehicle (HRV) Test Program," Prototype Development Associates, Inc., Final Report No. DNA 3842F, 10 November 1975.
2. Smith, D. H., "FLAME Nosetip Recovery Vehicle Flight Test Series," Prototype Development Associates, Inc., Final Report Draft, PDA TR 1027-00-01, for DNA under Contract No. DNA 001-74-C-0295, June 1978.
3. Moretti, G. and Bleich, G., "Three-Dimensional Inviscid Flow About Supersonic Blunt Cones at Angle of Attack, Vol. I," Sandia Laboratories, SC-CR-68-3728, September 1968.
4. "SAMSO/PDA Wake Drogue Study," Project No. V41A/B-M5A Data Package, Test Completion Date 9 November 1976.
5. Test Facilities Handbook (Tenth Edition), "von Karman Gas Dynamics Facility, Vol. 4," Arnold Engineering Development Center, May 1974.
6. Trimmer, L. L., Matthews, R. K., and Buchanan, T. D. "Measurement of Aerodynamic Heat Rates at the von Karman Facility," ICIASF 1973, Institute of Electrical and Electronics Engineers, Inc., New York, 1973, pp. 35-44.
7. Gardon, Robert, "An Instrument for the Direct Measurement of Intense Thermal Radiation," The Review of Scientific Instruments, Vol. 24, No. 5, May 1953, pp. 366-370.

DISTRIBUTION LIST

DEPARTMENT OF DEFENSE

Assistant to the Secretary of Defense
Atomic Energy
ATTN: Executive Assistant

Defense Advanced Rsch. Proj. Agency
ATTN: TIO

Defense Documentation Center
12 cy ATTN: DD

Defense Intelligence Agency
ATTN: DT-2
ATTN: DT-1B

Defense Nuclear Agency
ATTN: DDST
ATTN: STSP
3 cy ATTN: SPAS
4 cy ATTN: TITL

Field Command
Defense Nuclear Agency
ATTN: FCPR

Livermore Division, Field Command, DNA
ATTN: FCPRL

Commandant
NATO School (SHAPE)
ATTN: U.S. Documents Officer

Under Secretary of Defense for Rsch. & Engrg.
ATTN: Strategic & Space Systems (OS)

DEPARTMENT OF THE ARMY

BMD Advanced Technology Center
Huntsville Office
Department of the Army
ATTN: ATC-M

BMD Program Office
Department of the Army
ATTN: Technology Division

Harry Diamond Laboratories
Department of the Army
ATTN: DELHD-N-RBH
ATTN: DELHD-RC
ATTN: DELHD-N-TF, R. Oswald, Jr.
ATTN: DELHD-N-NP
ATTN: DELHD-N-P, J. Gwaltney

U.S. Army Ballistic Research Labs
ATTN: DRDAR-BL, R. Eichelberger

U.S. Army Material & Mechanics Rsch. Center
ATTN: DRXMR-HH, J. Dignam

U.S. Army Materiel Dev. & Readiness Command
ATTN: DRCDE-D, L. Flynn

DEPARTMENT OF THE ARMY (Continued)

U.S. Army Missile R&D Command
ATTN: DRDMI-XS

BMD Systems Command
Department of the Army
ATTN: BMDSC-TEB, R. Simpson

DEPARTMENT OF THE NAVY

Naval Sea Systems Command
ATTN: Code 0351

Naval Surface Weapons Center
ATTN: Code K06, W. Lyons
2 cy ATTN: Code K82, R. Feldhuhn/D. Reda

Strategic Systems Project Office
Department of the Navy
ATTN: NSP-272

DEPARTMENT OF THE AIR FORCE

Air Force Flight Dynamics Laboratory
ATTN: FXG
ATTN: FBC
ATTN: M. Buck
ATTN: J. Van Kueren

Air Force Geophysics Laboratory
ATTN: C. Touart

Air Force Materials Laboratory
ATTN: MBE, G. Schmidt
ATTN: LTM, H. Matern
ATTN: MXE, G. Ormbrek
ATTN: MBC, D. Schmitt
ATTN: MXS, Capt Heinonen

Air Force Office of Scientific Research
ATTN: P. Thurston

Air Force Rocket Propulsion Laboratory
ATTN: LKCP

Air Force Systems Command
ATTN: DLW

Air Force Weapons Laboratory
ATTN: SUL, F. Jenkins
ATTN: DYV

Arnold Engineering Development Center
Department of the Air Force
ATTN: XRRP
ATTN: R. Graham

Deputy Chief of Staff
Research, Development, & Acq.
Department of the Air Force
ATTN: AFRDQSM
ATTN: AFRDQ
ATTN: AFRDQPN

DEPARTMENT OF THE AIR FORCE (Continued)

Foreign Technology Division, AFSC

ATTN: PDBG

ATTN: A. Whitehall

Space & Missile Systems Organization/MN

Air Force Systems Command

ATTN: MNNR

ATTN: MNNH

ATTN: T. Graham

Space & Missile Systems Organization/RS

Air Force Systems Command

ATTN: RSS

ATTN: RST, J. McCormack

ATTN: RSSR, J. Pelligrani/Y. Randman

ATTN: RSSE, D. Jackson

7 cy ATTN: RSSE, W. Goldberg

Strategic Air Command/XPFS

Department of the Air Force

ATTN: XPFS

ATTN: XOBM

DEPARTMENT OF DEFENSE CONTRACTORS

Acurex Corporation

ATTN: J. Huntington

ATTN: C. Powars

ATTN: C. Nardo

Aerojet Liquid Rocket Company

ATTN: R. Jenkins

Aeronautical Rsch. Assoc. of Princeton, Inc.

ATTN: C. Donaldson

Aerospace Corporation

ATTN: W. Grabowsky

ATTN: W. Barry

ATTN: R. Mortensen

ATTN: D. Platus

ATTN: M. Gyetvay

ATTN: D. Nowlan

ATTN: R. Hallise

ATTN: P. Legendre

ATTN: W. Portenier

ATTN: H. Dyer

ATTN: B. Pershing

ATTN: A. Landauer

ATTN: A. Robinson

Aro, Inc.

ATTN: J. Adams

ATTN: G. Norfleet

Avco Research & Systems Group

ATTN: A. Pallone

ATTN: J. Stevens

ATTN: W. Broding

ATTN: V. Dicristina

ATTN: T. Saskaris

ATTN: F. Otoby

Boeing Company

ATTN: B. Lempriere

DEPARTMENT OF DEFENSE CONTRACTORS (Continued)

Calspan Corporation

ATTN: M. Holden

Effects Technology, Inc.

ATTN: R. Wengler

Ford Aerospace & Communications Corporation

ATTN: A. Demetriades

General Electric Company

Re-Entry & Environmental Systems Div.

ATTN: P. Cline

ATTN: B. Maguire

General Electric Company-TEMPO

Center for Advanced Studies

ATTN: DASIA

General Research Corporation

Santa Barbara Division

ATTN: R. Rosenthal

General Electric Company

Space Division

ATTN: J. Pettus

ATTN: K. Hall

Institute for Defense Analyses

ATTN: Classified Library

ATTN: J. Bengston

Ion Physics Corporation

ATTN: R. Evans

Kaman Sciences Corporation

ATTN: F. Shelton

ATTN: T. Meahger

Lockheed Missiles & Space Company, Inc.

ATTN: C. Lee

ATTN: D. Price

ATTN: G. Chrusciel

ATTN: P. Schneider

ATTN: R. Au

Lockheed Missiles and Space Company, Inc.

2 cy ATTN: T. Fortune

Martin Marietta Corporation

Orlando Division

ATTN: R. Cramer

ATTN: L. Kinnaird

McDonnell Douglas Corporation

ATTN: H. Hurwicz

ATTN: G. Fitzgerald

ATTN: L. Cohen

National Academy of Sciences

National Materials Advisory Board

ATTN: D. Groves

Pacific-Sierra Research Corporation

ATTN: G. Lang

Physics International Company

ATTN: J. Shea

DEPARTMENT OF DEFENSE CONTRACTORS (Continued)

Prototype Development Associates, Inc.

ATTN: J. Dunn
ATTN: D. Smith
ATTN: L. Groener

R & D Associates

ATTN: E. Field
ATTN: R. Ross
ATTN: P. Rausch

Science Applications, Inc.

ATTN: J. Warner

Science Applications, Inc.

ATTN: K. Kratsch
ATTN: L. Dunbar
ATTN: J. Courtney

Science Applications, Inc.

ATTN: C. Kyriss
ATTN: A. Martellucci

Southern Research Institute

ATTN: C. Pears

DEPARTMENT OF DEFENSE CONTRACTORS (Continued)

Spectron Development Labs, Inc.

ATTN: T. Lee

SRI International

ATTN: D. Curran
ATTN: G. Abrahamson

Systems, Science & Software, Inc.

ATTN: G. Gurtman

TRW Defense & Space Sys. Group

ATTN: D. Baer
ATTN: W. Wood
ATTN: R. Myer
ATTN: T. Williams
ATTN: I. Alber

TRW Defense & Space Sys. Group

San Bernardino Operations

ATTN: W. Polich
ATTN: V. Blankenship
ATTN: L. Berger
ATTN: E. Wong
ATTN: E. Allen